Summer 2021

Spatial variations of teleseismic P-wave attenuation and scattering beneath the southeastern United States and the Malawi and Luangwa rift zones in East Africa

Ashutosh Shrivastava

Department: Geosciences and Geological and Petroleum Engineering

SPATIAL VARIATIONS OF TELESEISMIC P-WAVE ATTENUATION AND SCATTERING BENEATH THE SOUTHEASTERN UNITED STATES AND THE MALAWI AND LUANGWA RIFT ZONES IN EAST AFRICA

by

ASHUTOSH SHRIVASTAVA

A DISSERTATION

Presented to the Graduate Faculty of the

MISSOURI UNIVERSITY OF SCIENCE AND TECHNOLOGY

In Partial Fulfillment of the Requirements for the Degree

DOCTOR OF PHILOSOPHY

in

GEOLOGY AND GEOPHYSICS

2021

Approved by:

Kelly H. Liu, Advisor
Stephen S. Gao
J. David Rogers
Neil Anderson
Mingzhen Wei

PUBLICATION DISSERTATION OPTION

This dissertation consists of the following two articles, formatted in the style used by the Missouri University of Science and Technology:

Paper I, found on pages 3–64, has been accepted in *Geochemistry, Geophysics, Geosystems*.

Paper II, found on pages 65–114, is intended for submission to *Earth and Planetary Science Letters*.

ABSTRACT

Seismic attenuation is an important physical parameter for characterizing subsurface morphology and the thermal structure of the Earth's crust and mantle. In this study, teleseismic *P*-wave amplitude spectra are used to examine the seismic attenuation beneath the southeastern United States and the Malawi and Luangwa rift zones in east African. The resulting seismic attenuation parameters (Δt^*) reveal a systematic contrast between the Appalachian Mountains and the Gulf of Mexico Coastal Plain exhibiting high and low attenuation, respectively. Spatial coherency analysis of the Δt^* observations suggests that the center of the low-attenuation layer is located within the uppermost mantle at about 70 km depth. The origin of this low-attenuation anomaly can be attributed to low-attenuation bodies in the form of remnant fossil lithospheric fragments in the deep crust or the uppermost mantle. The contribution of scattering to the observed Δt^* is relatively weaker in the Gulf of Mexico Coastal Plain, which is suggestive of a more homogenous crustal and uppermost mantle structure. The first regional-scale 3-D *P*-wave attenuation model demonstrates high-attenuation anomalies at the northern and southern tips of the Malawi Rift Zone (MRZ) and an elongated NE-SW strip of low-attenuation anomaly traversing central MRZ. The high attenuation zone beneath the Rungwe Volcanic Province is confined to the upper mantle, which can be associated with decompression melting in response to continental extension. The prominent low-attenuation anomaly beneath the Luangwa Rift Zone that traverses the central part of the MRZ suggests the presence of a relatively thick cratonic lithosphere and possibly advocates the southward subsurface extension of the Bangweulu block.

ACKNOWLEDGMENTS

It is a genuine pleasure to express my sincere gratitude to my advisor Dr. Kelly H. Liu for her continuous support and guidance throughout this research. I deeply appreciate her invaluable advice in paper writing, technical presentations, and all required resources for producing good works. I am especially grateful to my co-advisor Dr. Stephen S. Gao for providing outstanding mentorship and motivation. Constructive and insightful discussions with him were immensely helpful for my research.

I am grateful to my Ph.D. committee members Dr. J. David Rogers, Dr. Neil Anderson, and Dr. Mingzhen Wei for their thoughtful comments and encouragement in making this research a success. I am also thankful to my friends and colleagues in the geophysics group at Missouri S&T for their help and support.

Finally, I would like to thank my family for their endless love, support, and encouragement.

TABLE OF CONTENTS

LIST OF ILLUSTRATIONS

PAPER I Page

PAPER II

1. INTRODUCTION

In this study, we investigated the crustal and upper mantle attenuation structure beneath the southeastern United States (SEUS) and the Malawi and Luangwa rift zones of the East African Rift System (EARS) using the teleseismic *P*-wave amplitude spectra. The SEUS is tectonically more stable than the western U.S. but is more active than most portions of the central U.S. Alleghanian orogeny is the most recent and the final phase of mountain building in this region which was caused by the collision of Laurentia and Gondwana over 330 Ma (Iverson & Smithson, 1983; Rankin et al., 1991). This collision marked the formation of the Appalachian Mountains and the addition of the Suwannee terrane, which has significantly different tectonic attributes, lithology, and fossil accumulations than Laurentia (Mueller et al., 2014). Previous continental-scale seismic attenuation studies in North America reported a general trend of relatively low attenuation in the eastern U.S. in comparison to the tectonically active western U.S. (Der et al., 1982; Der & McElfresh, 1977; Hwang et al., 2009; Lawrence et al., 2006; Solomon & Toksöz, 1970). Most of the previous studies were conducted for the entire continental U.S. with a limited spatial resolution in the SEUS. This motivated us to utilize the recently deployed dense USArray for conducting a high-resolution *P*-wave attenuation analysis. We carried out a comprehensive assessment of seismic attenuation, which is an important physical parameter for characterizing subsurface morphology and the thermal structure of the Earth's crust and mantle.

In the second part, we estimated the seismic attenuation structure beneath the Malawi and Luangwa rift zones to investigate the mantle dynamics associated with early-

stage rifting. The Malawi Rift Zone (MRZ) is an ~800 km long N-S-oriented Cenozoic rift which initiated with an onset of volcanism in the Rungwe Volcanic Province (RVP) at its northern terminus (Ebinger et al., 1989; 1993). Located to the west of the MRZ lies the ~600 km long and ~80 km wide Permo-Triassic Luangwa Rift Zone (LRZ) of Zambia which represents the initial continuation of the EARS into the southwestern branch (Banks et al., 1995; Fritz et al., 2013). Previous seismic studies have proposed active rifting models for the EARS advocating that the upward movement of the asthenosphere is thermally eroding the lithospheric mantle and consequently thinning it (Kampunzu & Lubala, 1991; Yirgu et al., 2006). Seismic (Ritsema, 1999) and geochemical (Hilton et al., 2011) studies have proposed that the African Superswell, which is a NE tilted low-velocity anomaly originating from the lowest mantle beneath southern Africa provides dynamic support in the form of either a single plume or multiple upwellings. However, the extent of influence of the African Superswell on the volcanism beneath the RVP, and rift initiation in the MRZ remains a subject of debate. This is evident by the low-velocity anomaly beneath the RVP reported in velocity tomography studies was mainly confined in the uppermost mantle and was explained by the decompression melting (O'Donnell et al., 2016; Yu et al., 2020). We estimated 3-D *P*-wave attenuation structure beneath the MRZ and adjacent areas to provide crucial insight into weakening mechanisms and rift initiation.

PAPER

I. TELESEISMIC P-WAVE ATTENUATION BENEATH THE SOUTHEASTERN UNITED STATES

ABSTRACT

Seismic attenuation is an important parameter for characterizing subsurface morphology and thermal structure. In this study, we use *P*-wave amplitude spectra from 588 teleseismic events recorded by 477 broadband seismic stations in the southeastern United States to examine the spatial variations of seismic attenuation in the crust and upper mantle. The resulting seismic attenuation parameter (Δt^*) measurements obtained using the spectral ratio technique reveal a zone of relatively low attenuation in the Gulf of Mexico Coastal Plain and the southwestern terminus of the Piedmont province. Spatial coherency analysis of the Δt^* observations suggests that the center of the low attenuation layer is located within the uppermost mantle at about 70 km depth. This low attenuation anomaly lies along the suture zone between Laurentia and Gondwana and approximately coincides with the east-west trending Brunswick magnetic anomaly. The origin of this low attenuation anomaly can be attributed to low attenuation bodies in the form of remnant fossil lithospheric fragments in the deep crust and the uppermost mantle. The contribution of scattering to the observed Δt^* is estimated by calculating the ratio of amplitude on the transverse and vertical components in the *P*-wave window. Relative to the rest of the study area, the Gulf of Mexico Coastal Plain demonstrates weaker

scattering which is suggestive of a more homogenous crustal and uppermost mantle structure.

1. INTRODUCTION

Seismic attenuation is an important physical parameter for characterizing rocks and providing significant constraints on the viscosity, rigidity, temperature, and mineral composition of the Earth's crust and mantle (Jackson & Anderson, 1970; Knopoff, 1964). Additionally, seismic attenuation measurements can provide independent constraints on the interpretation of seismic velocity models (Deen et al., 2006; Faul & Jackson, 2005; Godey et al., 2004; Goes et al., 2000; Goes & Lee, 2002; Hwang et al., 2009; Lee, 2003; Schutt & Lesher, 2006; Shapiro & Ritzwoller, 2004; Sobolev et al., 1996). Previous seismological investigations suggest that anelasticity and velocity variations exhibit strong sensitivity to temperature anomalies in the uppermost mantle (Anderson, 1967; Faul & Jackson, 2005; Goes et al., 2000; Jackson et al., 2002; Karato, 1993; Knopoff, 1964; Sato et al., 1989; Wang et al., 2017). Such anelasticity can be estimated by measuring the attenuation of teleseismic body waves, as they provide frequencies intermediate to those of long-period surface waves and regional earthquake body waves (Solomon, 1972; Wang et al., 2017).

Anelastic or intrinsic attenuation refers to the conversion of seismic energy into heat, generally caused by grain boundary friction (Jackson & Anderson, 1970) and the movements of dislocations through the mineral grains (Gorich & Muller, 1987). Anelastic attenuation of seismic waves in a medium is expressed in terms of the seismic

quality factor (Q), which is inversely proportional to anelastic attenuation. The relation between Q and energy dissipation is

$$Q = 2\pi\frac{Eo}{\delta E}, \quad (1)$$

where E_o is the maximum value of elastic energy stored during one cycle of loading, and δE is the energy loss during the cycle (Knopoff, 1964).

In addition to anelasticity, scattering can also lead to the reduction of body-wave amplitude. Akinci et al. (1995) propose that the energy dissipation of body waves due to scattering is more prominent at shorter distances and decreases substantially as the propagation distance increases. The study also suggests that intrinsic attenuation is dominant at larger epicentral distances, without showing a strong frequency dependence. Laboratory experiments have also reported frequency-independent Q for many solids up to moderately high frequencies (Knopoff, 1964). On the basis of previous laboratory and observational studies (Dziewonski, 1979; Jackson & Anderson, 1970; Knopoff, 1964), frequency-independent Q is assumed in this and numerous previous studies (e.g., Hwang et al., 2009) to estimate the attenuation of teleseismic P-waves for frequencies up to 1 Hz.

The southeastern United States (SEUS) is tectonically more stable than the western U.S. but is more active than most portions of the central U.S. (Figure 1). Since the late Proterozoic (>1.0 Ga), multiple phases of terrane accretion, orogenies, and continental breakups have taken place in the SEUS (Cook et al., 1979; Hatcher, 2010; Thomas, 2006). The Grenville orogeny is the oldest known Mesoproterozoic mountain-building episode that marks the assembly of the supercontinent Rodinia (~1.1 Ga) (Denison et al., 1984; Thomas, 1985). The Grenville Front separates the SEUS continental margin from the Mazatzal province (Figure 1), which was formed due to the

accretion of juvenile volcanic arcs to the older stable core of North America. Following the breakup of Rodinia (~570 Ma), several episodes of continental accretion and orogenies resulted in the formation of the SEUS terrane. The Alleghanian orogeny represented by the collision of Laurentia and Gondwana at ~330 Ma resulted in the formation of the supercontinent Pangea (Iverson & Smithson, 1983; Rankin et al., 1991). This collision marked the formation of the Appalachian Mountains and the addition of the Suwannee terrane, which has significantly different tectonic attributes, lithology, and fossil accumulations than Laurentia (Mueller et al., 2014). A regionally extensive swath of lower-than-normal magnetism known as the Brunswick Magnetic Anomaly (BMA; Figure 1) lines up with the Suwannee Suture zone (Higgins & Zietz, 1983; Mueller et al., 2014; Williams & Hatcher, 1983).

The attenuation structure from previous continental-scale studies in North America suggests relatively low attenuation in the eastern and southeastern U.S. in comparison to the tectonically active western U.S. (Der et al., 1982; Der & McElfresh, 1977; Hwang et al., 2009; Lawrence et al., 2006; Solomon & Toksöz, 1970). A recent study (Cafferky & Schmandt, 2015) computes the spatial variation of seismic attenuation across the U.S. using teleseismic *P*-wave spectra from deep earthquakes for multiple frequency bands between 0.08-2 Hz. All frequency bands yield a high attenuation region near the Appalachian margin and low to medium attenuation is reported in the continental interior. Most of the previous seismic attenuation studies are conducted for the entire continental U.S. with a limited spatial resolution in the SEUS. In this study, a comprehensive assessment of seismic attenuation and the effects of scattering beneath the SEUS is conducted using data from the USArray and other portable or permanent

deployments listed in the Data Availability Statement section. The results support the existence of remnant lithospheric segments in the crust and upper mantle beneath the Gulf of Mexico (GoM) Coastal Plain.

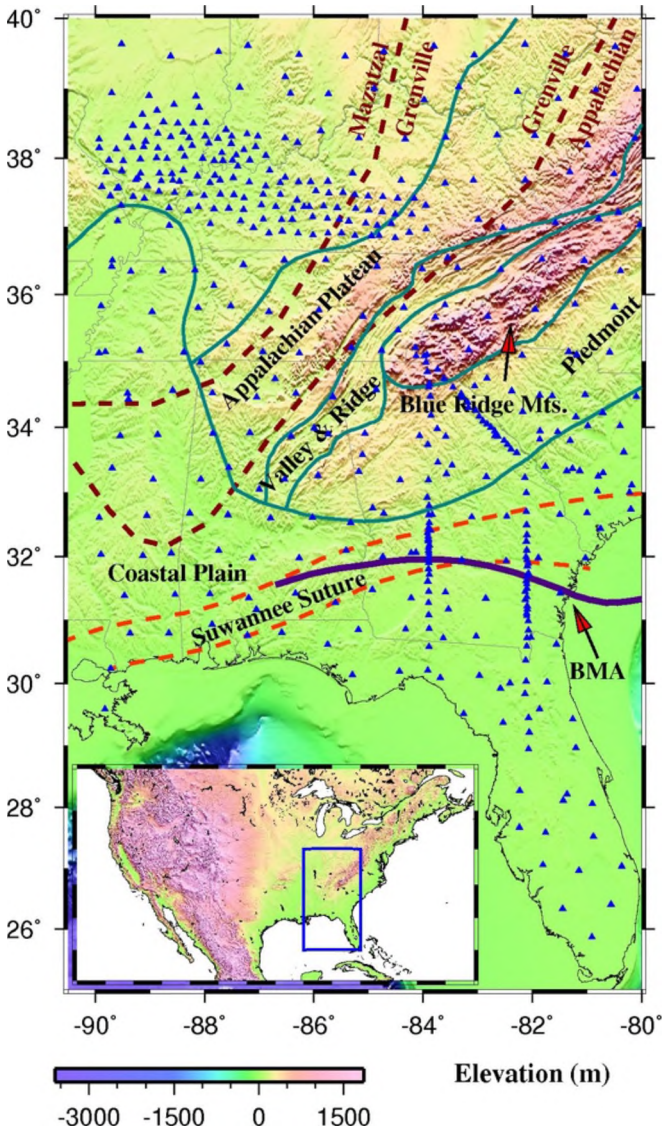

Figure 1. Topographic map of the study area showing the location of seismic stations (blue triangles), physiographic boundaries (teal solid lines), Precambrian basement terrane boundaries (maroon dashed lines), Suwannee Suture Zone (Mueller et al., 2014) (orange dashed lines), and the path of the Brunswick Magnetic Anomaly (BMA) (Mueller et al., 2014) (purple line). The inset in the figure shows the location of the study area marked by the blue rectangle.

2. DATA AND METHODS

Seismic data used in the study were recorded by 477 broadband seismic stations and were obtained (Figure 1) from the Incorporated Research Institutions for Seismology (IRIS) Data Management Centre (DMC). The stations include 220 USArray Transportable Array (TA) stations which sampled the study area with ~70 km spacing. The cutoff magnitude (M_c) for data requesting is computed using $M_c = 5.2 + (\Delta\text{-}\Delta_{min})/(180.0–\Delta_{min}) – D/ D_{max}$, where Δ is the epicentral distance (which ranges from 30° to 180°) in degree, D is the focal depth in km, Δ_{min}=30°, and D_{max}=700 km (Liu & Gao, 2010). The events were recorded by both portable and permanent seismic stations in the area of 25° to 40° North and 80° to 90° West, between March 1993 and January 2019. To enhance the quality of the measurements, only events recorded by a minimum of 10 stations were kept, and as a result, 588 teleseismic events (Figure 2) were used in the study.

Several techniques have been developed to estimate the amplitude of seismic attenuation. These techniques can be broadly classified as either time-domain methods or frequency-domain methods. Wavelet modeling (Jannsen et al., 1985), rise-time (Gladwin & Stacey, 1974), and analytical signal (Taner et al., 1979) methods are some of the major techniques used to compute seismic attenuation in the time domain, whereas methods such as spectral ratio (Teng, 1968), spectral matching (Raikes & White, 1984), coda normalization (Aki, 1980), and spectral modeling (Gao, 1997; Halderman & Davis, 1991) work in the frequency domain. Attenuation is measured in terms of the attenuation

parameter t*, which is defined as the total traveltime of the wave along the raypath divided by the quality factor (Kovach & Anderson, 1964), i.e.,

$$t^* = \int_{ray} \frac{1}{V(r)Q(r)} ds, \quad (2)$$

where $V(r)$ is the velocity of the waves, and $Q(r)$ is the quality factor.

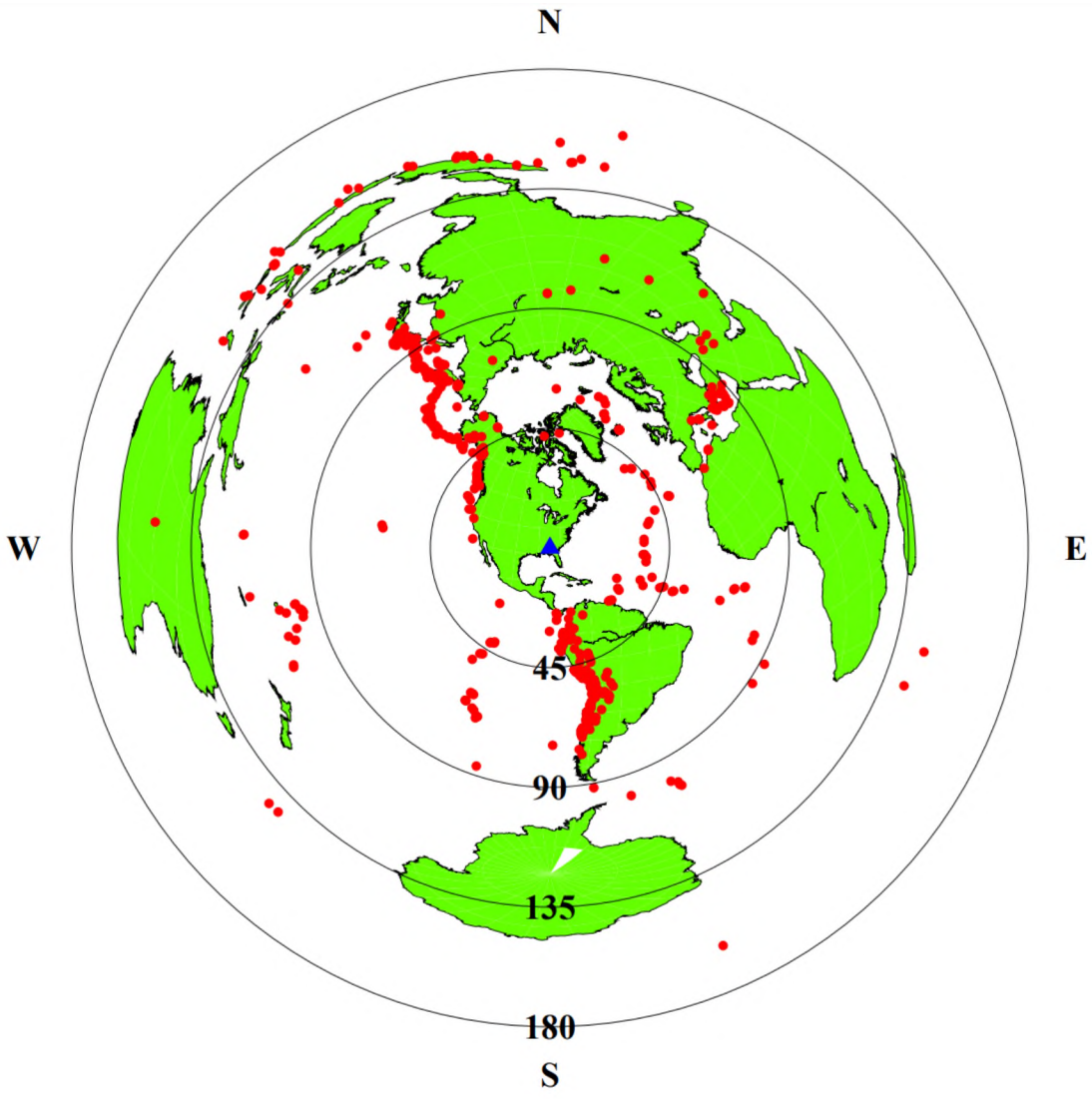

Figure 2. An azimuthal equidistant projection map centered at the study area showing the teleseismic events (red dots) used in this study. The concentric circles represent the distances (in degree) from the center of the study area (blue triangle).

In the frequency domain, the amplitude spectrum $A_{ik}(f)$ of an event 'k' recorded at station 'i' can be expressed as (Teng, 1968):

$$A_{ik}(f) = S_k(f)G_{ik}(f)R_{ik}(f)I_i(f), \quad (3)$$

where $S_k(f)$ is the source spectrum of the source wavelet, $R_{ik}(f)$ is the spectrum of the near-receiver effects, $I_i(f)$ is the spectrum of the instrument response, and $G_{ik}(f)$ is the spectrum of Green's function, which can be written as

$$G_{ik}(f) = e^{-\pi f t^*_{ik}(f)}, \quad (4)$$

The spectral ratio method used in the study is the most widely used technique to estimate seismic body-wave attenuation relative to a reference spectrum (e.g., Der & McElfresh, 1976; Hwang et al., 2009; Solomon & Toksöz, 1970; Teng, 1968). One of the benefits of using this method is that for teleseismic events, the source signal and common path effects are removed. The requested vertical component seismograms are re-sampled into a sampling frequency of 20 sps, and a section of the vertical component seismogram with a total length of 51.2 s (i.e., 1024 data samples) starting from 10 s before the theoretical arrival time of the *P* (or *PKP*) is selected for computing the spectrum. The instrument response is removed by deconvolving the seismograms with the instrument response function. A 10-s window length before the arrival of *P*-wave is used to determine the noise amplitude. The signal-to-noise ratio (SNR) between the maximum absolute value of the signal amplitude and mean absolute noise amplitude is computed for every trace, and seismograms with an SNR smaller than 10.0 are not used for the study. The *P*-wave section of the seismogram is tapered using the customary cosine-sum window, with the form:

$$w(n) = a_0 - (1 - a_0)\cos\frac{2\pi n}{N}, 0 \le n \le N, \quad (5)$$

where $w(n)$ is a zero-phase function, N is a positive integer, and the numerical value of a_0 is set as 0.54, which categorizes this tapering function as a Hamming window.

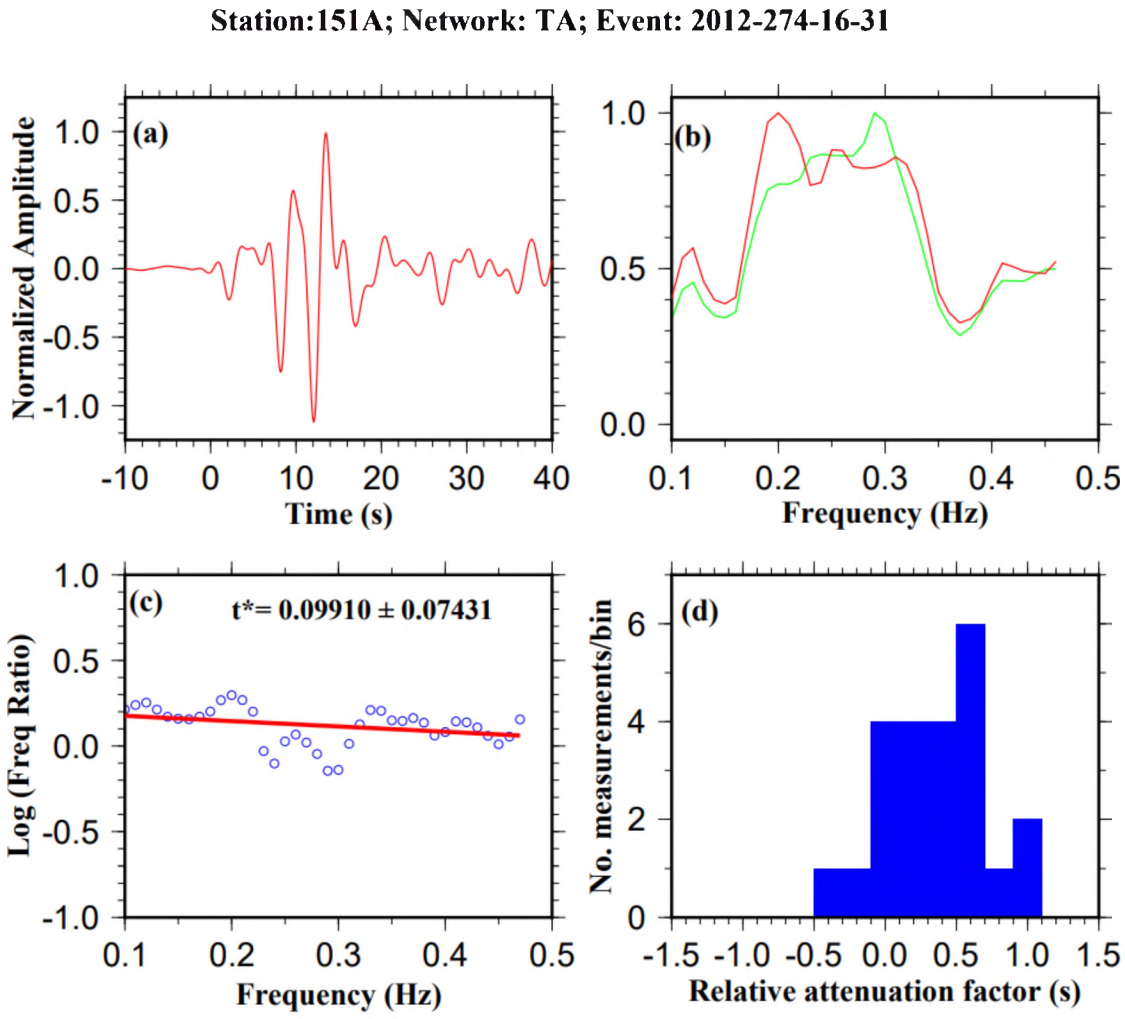

Figure 3. An example of spectral ratio analysis for TA station 151A. (a) Normalized *P* waveform for TA station 151A for event 2012-274-16-31 with an epicentral distance of 31.6°. (b) Normalized spectra for the time series shown in (a) (red), and the mean spectrum (green). (c) The spectral ratio between Station 151A and the mean spectrum plotted against frequency. The red line represents the line of best fit. (d) Histogram of Δt* measurements for all the events recorded by Station 151A.

A bandpass filter with corner frequencies of 0.1 Hz and 0.5 Hz is applied to the selected seismograms. Amplitude spectra of all the filtered high-quality seismograms are computed using the Fourier transform. To minimize the effects of heterogeneities outside the study area, for each event we use the mean spectrum computed over all the stations that recorded this event as the reference spectrum in the spectral ratio. Additionally, to exclude seismograms with high noise, the minimum correlation coefficient between each spectrum and the mean spectrum is set to 0.9. The relative attenuation factor Δt^*_{ik} between station 'i' and the reference spectrum from event 'k' is calculated by fitting the spectral ratio with a straight line using the least-squares method (Der & McElfresh, 1977; Solomon & Toksöz, 1970), that is,

$$\ln \frac{A_i(f)}{A_k(f)} = C - \pi \Delta t^*_{ik} f, \quad (6)$$

where C is the ratio between the near receiver effects of station 'i' and the reference spectrum from event 'k' ($R_{ik}(f)$ in Equation 3) and is assumed to be frequency independent. The automatically computed results are then manually checked to remove measurements with abnormal data or with a nonlinear frequency variation of the spectral ratios. Furthermore, Δt^*_{ik} measurements with an absolute value greater than 1.0 s, or a standard deviation greater than 0.2 s are excluded. Figure 3 shows an example of the spectral ratio and associated spectra and seismograms.

3. RESULTS

The resulting 14,702 individual Δt* measurements (Figure 4a) obtained using the spectral ratio method are used to compute the station-averaged Δt* measurements if the

number of measurements obtained at the station is three or greater (Figures 4b & 5a and Table S1), which vary from -0.62 s ± 0.03 s to 0.60 s ± 0.04 s in the study area and demonstrate systematic spatial variations.

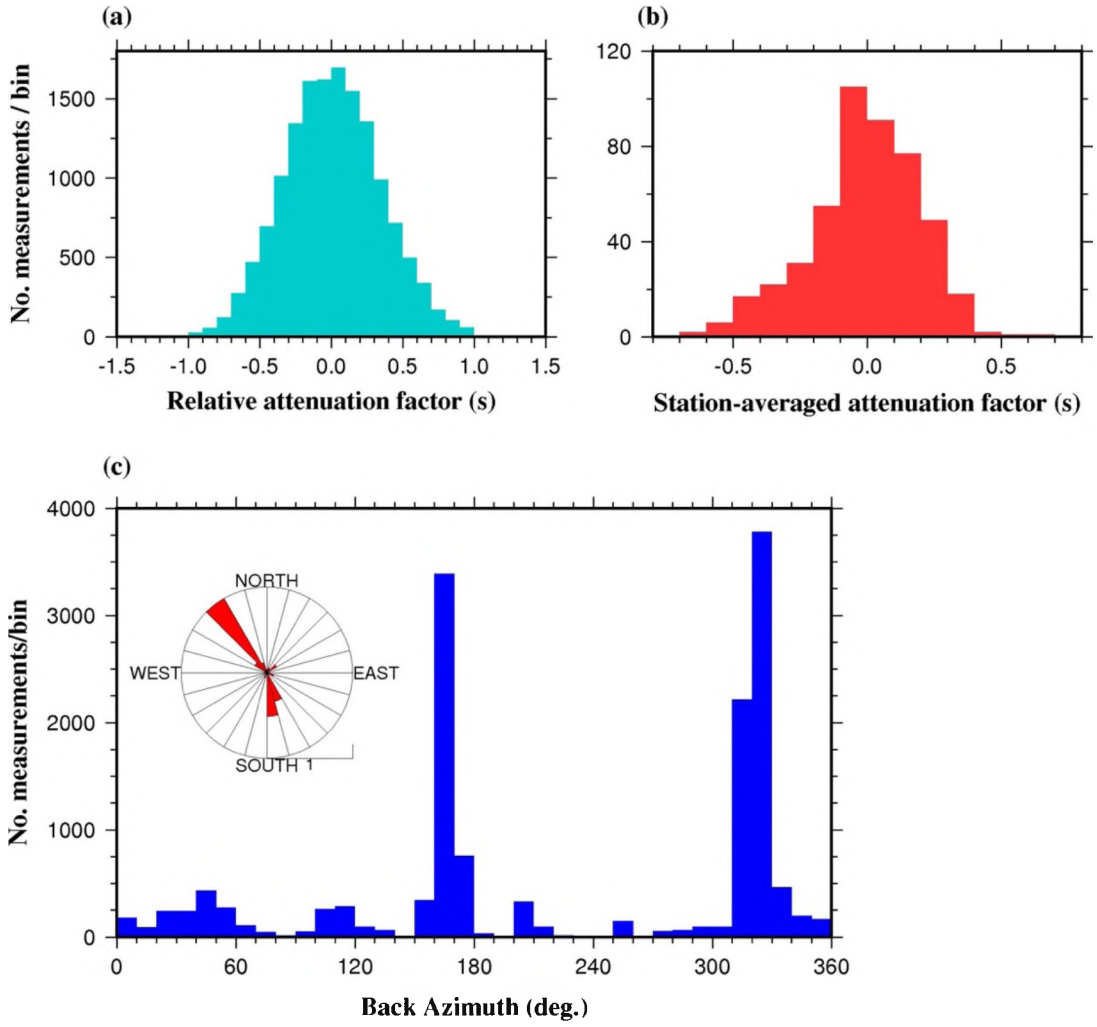

Figure 4. Distribution of (a) Δt* measurements for all events and (b) station-averaged Δt* measurements. (c) Azimuthal distribution of the individual Δt* measurements.

The station-averaged Δt* measurements (Figure 5a) are spatially interpolated by averaging the measurements in overlapping 1° by 1° blocks with a moving step of 0.1°

(Figure 5b). We experimented with different values of the size of the blocks for smoothing and found 1° to be a balanced value that most clearly demonstrates the spatial variation of station averaged Δt* measurements. As the block size for smoothing increases, both the spatial resolution and peak-to-peak range of the Δt* measurements decrease, and vice versa. To get a sense of the uncertainties in the Δt* measurements, we compute the spatial distribution of the standard deviation (SD) of the Δt* measurements (Figure 6). Areas with the largest SD are in the Florida Peninsula and along the southernmost part of the Gulf of Mexico (GoM) Coastal Plain. Some previous studies (e.g., Cafferky & Schmandt, 2015; Dong & Menke, 2017) used only events with hypocenters deeper than at least 150 km for attenuation measurements for the purpose of reducing the impact of the reduction in high-frequency components by the lithosphere on the source-side. To explore the influence of including the shallow events, we compute Δt* measurements by only using events with a focal depth ≥ 150 km. The results (Figure S1) show similar spatial variations with those obtained using all the events (Figure 5), even with a much-reduced number of measurements.

Based on the characteristics of the measurements (Figure 5) and the tectonic setting, we divide the study area into five areas: Mazatzal Province (A), Grenville Province (B), Southern Appalachian Mountain Range and Piedmont Province (C), GoM Coastal Plain (D), and Florida Peninsula (E). Area A is part of the stable central North American craton and is characterized by positive V_p anomalies in the upper-most mantle (Figure 5a) (Golos et al., 2020). Physiographically, the eastern portion of Area A belongs to the Appalachian Plateau, located adjacent to the southern end of the Appalachian

Mountains. The southeastern region of Area A displays higher attenuation relative to other regions in the area.

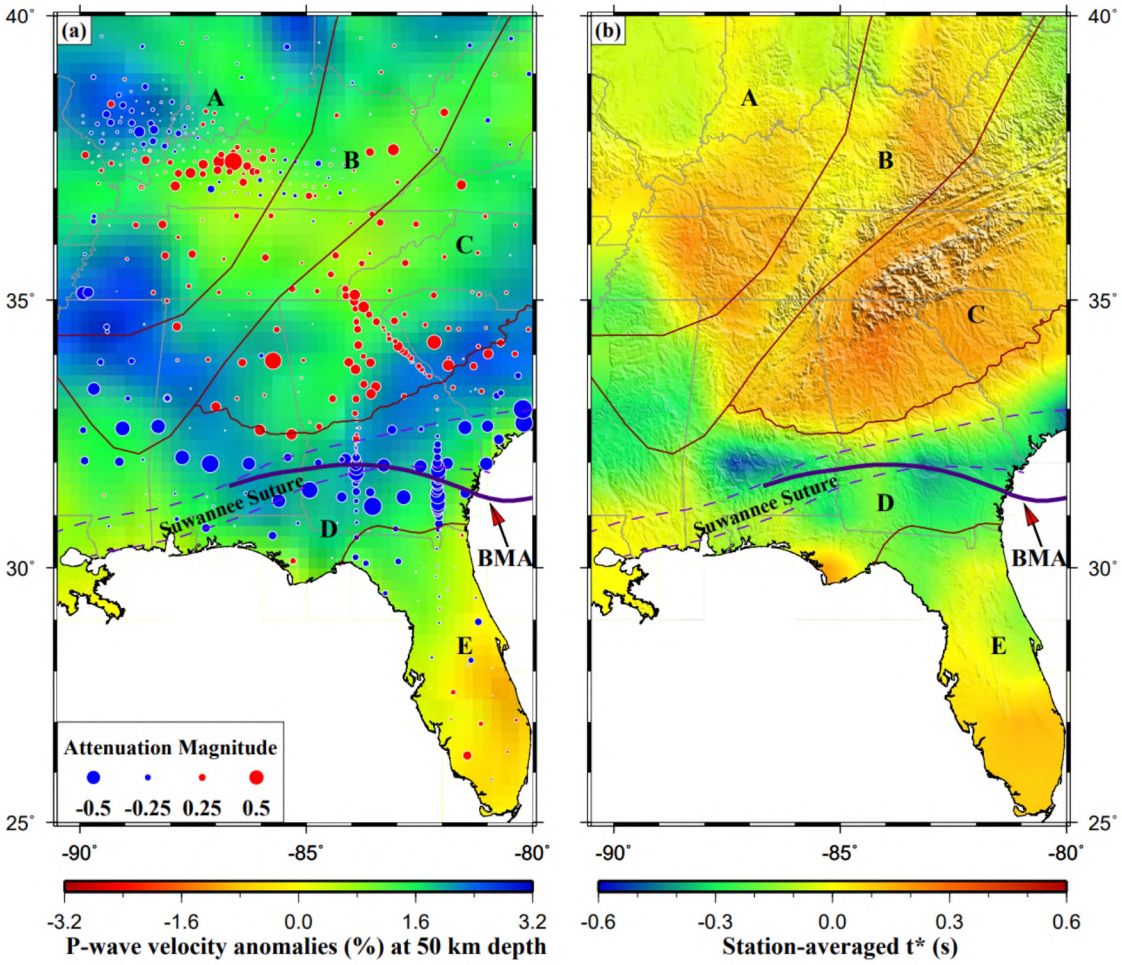

Figure 5. Station-averaged *P*-wave attenuation factors (circles) plotted on a background of *P*-wave velocity anomalies (%) at 50 km depth (Golos et al., 2020). Maroon lines represent the boundaries of five regions, divided based on the characteristics of the measurements and the tectonic setting. (b) Spatially averaged *P*-wave attenuation factors.

The western portion of Area A consists of the Interior Lowlands that includes several structural depressions that have filled with sediment mostly eroded from the

mountains (Swaby et al., 2016). Attenuation decreases gradually westward as the lithospheric thickness beneath the stable part of North America Craton increases. The northwestern region of Area A consists of the Illinois Basin comprising of a thick layer of Cambrian through Pennsylvanian sedimentary rocks (Swann, 1968) and Proterozoic granites and rhyolite in the basement which date back to around 1.55 Ga (van der Pluijm and Catacosinos, 1996; van Schmus et al., 2007). Negative Δt* measurements obtained in the Illinois Basin coincide with the strong positive V_p anomaly mapped by Golos et al. (2020) that extends up to the depth of 70 km. The southernmost tip of Area A is characterized by negative Δt* observations belonging to a zone of low attenuation pervasively observed along the northern border of the GoM Coastal Plain (Figure 5). The average Δt* value for Area A is close to zero (0.01 s ± 0.01 s).

Area B occupies the Grenville Province tectonically and is composed of the Appalachian Plateau except for the southernmost quarter which belongs to the GoM Coastal Plain. The observed Δt* values show a sharp contrast between the Appalachian Plateau and the GoM Coastal Plain, with mean values of 0.03 s ± 0.01 s for the former, and -0.30 s ± 0.03 s for the latter region. The NE portion of the area, which is found to possess high V_P anomalies in the uppermost mantle (Figure 5a), shows reduced Δt* measurements. The SW boundary of Area B traverses the area with negative Δt* values, suggesting that the observed spatial variation of the Δt* measurements is not controlled by Precambrian basement terranes, but by physiographic divisions which are mostly the result of post-Precambrian tectonic activities.

Area C is a physiographical province mostly consisting of the Blue Ridge Mountains and Valley and Ridge of the southern Appalachian Mountains in the west, and a plateau region of the Piedmont Province in the east.

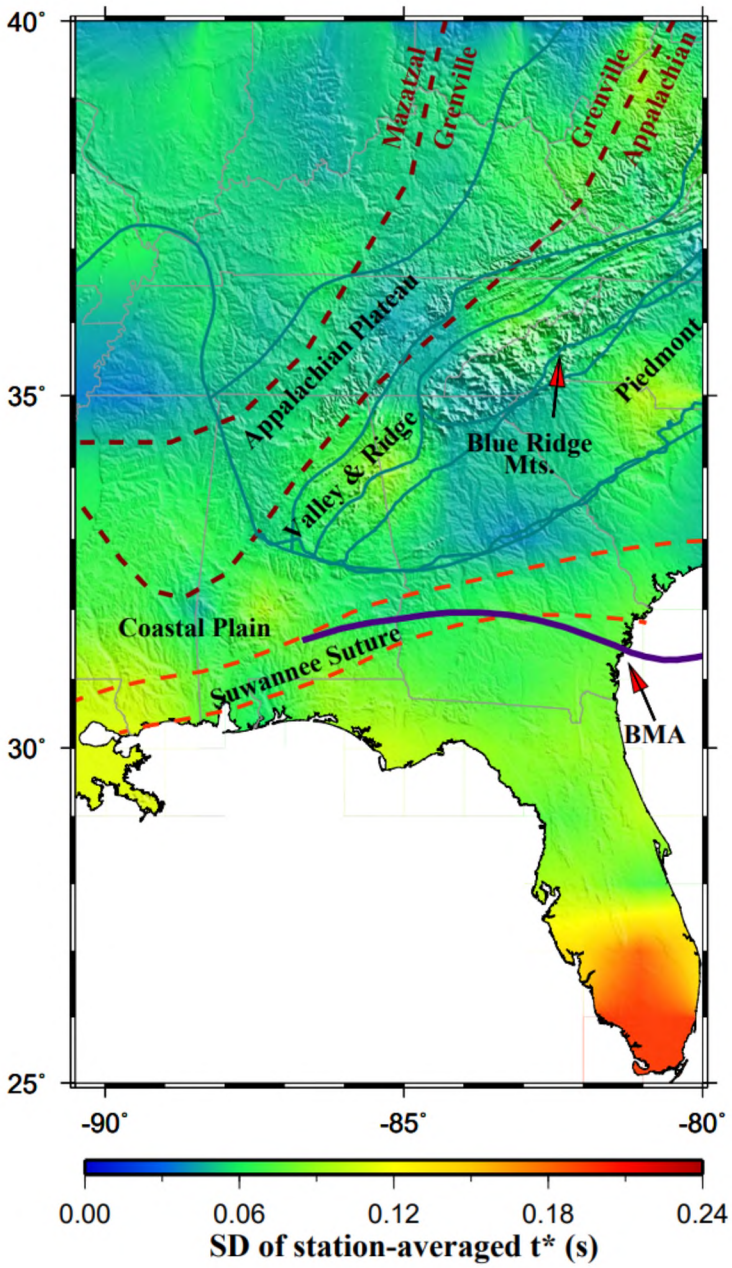

Figure 6. Distribution of the standard deviation of station averaged *P*-wave attenuation factors.

Although the western and the eastern regions of Area C are physiographically distinct from each other, both regions share similar crystalline igneous and metamorphic rocks (Swaby et al., 2016). The northernmost part of this area is comprised of the Appalachian Plateau. Similar to Areas D and E, tectonically it is part of the Paleozoic-Cenozoic Appalachian Province. The Δt^* measurements are comparable to Areas B, with an areal mean value of 0.16 s ± 0.01 s but are higher than those observed on the GoM Coastal Plain (Figure 5). No obvious change in Δt^* is observed across the boundary between this area and Area B, which is a tectonic boundary.

Area D belongs to the GoM Coastal Plain, which is composed of very young rocks, ranging in age from the Cretaceous to the present. It is characterized by a well-defined E-W zone of low Δt^* measurements, except for the NE and SW corners of the area. The zone of negative Δt^* closely follows the northern boundary of the GoM Coastal Plain and extends to the southernmost portions of Areas A and B. The mean Δt^* value for this area is -0.17 s ± 0.02 s which is the lowest among all the five areas.

Area E which includes the Florida Peninsula is characterized by Δt^* values that are intermittent between those observed in Areas A-C and D, with a mean value of -0.03 s ± 0.02 s. The Δt^* values demonstrate a southward gradual increase (Figure 5a), and the same trend is observed for the uncertainty of the measurements (Figure 6).

We estimate the optimal depth of the observed Δt^* anomalies by adapting a procedure that was developed for estimating the depth of the source of anisotropy using shear wave splitting measurements (Liu & Gao, 2011). Spatial coherency of seismic attenuation parameters is used to estimate the depth of seismic attenuation by computing a spatial variation factor ($F_{\Delta t}$). The geometric distribution of the ray-piercing points is

computed at an incremental interval of 5 km from 0 – 400 km, based on the IASP91 Earth model (Kennett & Engdahl, 1991).

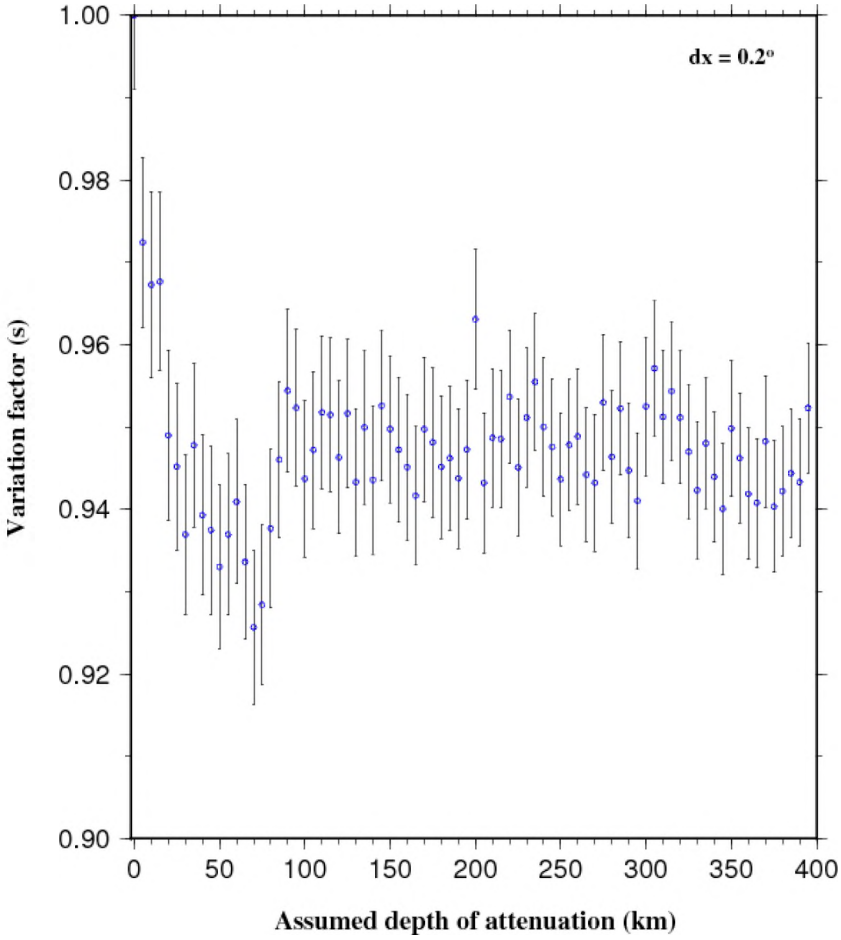

Figure 7. Depth of the source of attenuation estimated using the approach of Gao and Liu (2012) with a bin size (dx) of 0.2°.

For each depth, the study area is divided into overlapping blocks of 0.2° x 0.2° at a distance of 0.05° between the centers of the neighboring blocks. $F_{\Delta t}$ values are then calculated at each depth using

$$F_{\Delta t} = \frac{1}{N}\sum_{i=1}^{N}\sqrt{\frac{1}{M_i - 1}\sum_{j=1}^{M_i}(\Delta t_{ij} - \overline{\Delta t_i})^2}, \quad (7)$$

where N is the number of blocks, Mi is the number of measurements for the i-th block, Δt_{ij} is the attenuation parameter in the i-th block, and $\overline{\Delta t_i}$ is the average Δt* over all the measurements in block i. A detailed explanation of this approach along with the FORTRAN program is illustrated in Gao and Liu (2012). The assumption adopted in this approach is that the attenuation of body waves is caused by a single horizontal layer with spatially variable thickness. This means that the resulting optimal depth corresponding to the minimum value of $F_{\Delta t}$ indicates the center of the layer. Figure 7 shows the calculated $F_{\Delta t}$ plotted against the assumed depth of attenuation for the SEUS. The resulting $F_{\Delta t}$ shows that the optimal depth is about 70 km, i.e., in the uppermost mantle. Note that the optimal depth can be viewed as the weighted mean depth computed by the magnitude of lateral variations of the observed Δt* values. For a homogenous layer, it is the depth of the center of the layer. If Δt* variations decrease with depth, the resulting optimal depth is smaller than the center of layer and vice versa. In all cases, the actual thickness of the layer cannot be determined.

4. DISCUSSION

4.1. COMPARISONS WITH PREVIOUS SEISMIC WAVE ATTENUATION AND VELOCITY TOMOGRAPHY STUDIES

Previous larger-scale body wave (Cafferky & Schmandt, 2015; Hwang et al., 2009; Solomon & Toksöz, 1970) and surface wave (Bao et al., 2016; Baqer & Mitchell, 1999; Pasyanos, 2013) attenuation studies show a common pattern of high attenuation in

the Appalachian Mountains and low attenuation beneath the GoM Coastal Plain. Cafferky & Schmandt (2015) map the upper mantle Δt* values across the contiguous U.S. by inverting teleseismic *P*-wave amplitude spectra for multiple frequency bands ranging between 0.08-2 Hz. The Δt* values obtained for all the frequency bands are consistent with the results obtained in this study. Cafferky & Schmandt (2015) display the Δt* measurements using a median smoothing radius of 1.75° and 5° that resulted in two different spatial resolutions. The spatially interpolated results from this study (Figure 5b) are obtained by overlapping 1° by 1° blocks and are similar to their results obtained using the median smoothing radius of 1.75°. They report the lowest mean 95% confidence interval of Δt* measurements (0.09 s) for the 0.08-2 Hz band, and highest (0.21 s) for the 0.08-0.5 Hz band calculated using over 16,000 Δt* measurements across the entire contiguous U.S. In comparison, the 95% confidence interval of 14,702 Δt* measurements in our study is 0.01 s for the SEUS. Note that in our study the frequency band is 0.1-0.5 Hz, where the teleseismic *P*-wave is the strongest (Figure 3b) which could account for the differences in the small confidence interval of our measurements.

A surface wave attenuation study (Gallegos et al., 2014) uses a two-station method to estimate *Lg* attenuation in the central and eastern U.S. Their results reveal a low crustal attenuation anomaly beneath the GoM Coastal Plain, which correlates with the location of the low attenuation anomaly observed in our study. Lawrence et al. (2006) measure seismic attenuation beneath the North American continent using waveform cluster analysis and further correlate the results with the travel time. The study finds that seismic travel times and attenuation are weakly correlated ($R^2 < 0.3$). The sparsely populated seismic stations over a large study area and decreased waveform coherence

between the stations produced large-scale variations in seismic attenuation, and therefore, the attenuation structure in the SEUS is mapped with a low spatial resolution relative to those using data from the USArray. Other previous studies (Der et al., 1982; Der & McElfresh, 1977; Hwang et al., 2009; Solomon & Toksöz, 1970) calculate the crustal and upper mantle seismic attenuation beneath the U.S., and none of them reveals the low attenuation anomaly observed in our results near the southwestern terminus of Piedmont (Figure 5b). This is possibly due to the limited number of stations used in most of these studies to produce continent-scale attenuation maps, hence unable to resolve detailed features, and only major trends are reported. Our results make a more comprehensive assessment of *P*-wave attenuation using a large number of waveforms thereby obtaining a more detailed attenuation structure of the SEUS.

We next compare our results with those from previous velocity tomography studies to provide constraints on the geological implications of the attenuation measurements. The shear velocity in the upper mantle beneath the study area is as much as 15-20% higher than that in the western U.S. as reported in the studies of body wave travel-times (Golos et al., 2018; Grand & Helmberger, 1984; Melbourne & Helmberger, 1998) and surface wave dispersion (Marone & Romanowicz, 2007; van der Lee & Nolet, 1997). Golos et al. (2018) estimate the variations in shear wave speed anomalies in the crust and upper mantle using data from the USArray and permanent seismic networks in the continental U.S. Their body wave inversion results indicate low wave speeds beneath the Appalachian Mountains which correlate with the high attenuation observed in Areas B and C in our study. These low wave speed anomalies are confined in the depth range between 40 and 60 km, as inferred from the surface wave inversion results. Another study

(Shen & Ritzwoller, 2016) estimates similar low-velocity anomalies in the mantle beneath the Appalachians in western Virginia. Some of the recent studies (Biryol et al., 2016; Golos et al., 2020; Wang et al., 2019) map the 3-D *P*-wave velocity structure of the crust and upper mantle beneath the southeastern U.S. using the travel-time residuals from teleseismic *P*-wave data. Biryol et al. (2016) report high-velocity anomalies beneath the GoM Coastal Plain in the upper-most mantle (approximately 60-130 km depth range), which coincide with the location of the low attenuation anomaly observed in our study. In Figure 5a we plotted the *P*-wave velocity tomography results obtained by Golos et al. (2020) at the 50 km depth to examine the correlation of *P*-wave velocity and attenuation. Patches of relatively high-velocity anomalies are observed near the location of low-attenuation anomaly in the GoM Coastal Plain (Area D). Using seismic ambient noise recorded across the contiguous U.S., Bensen et al. (2008) produce shear wave tomographic dispersion images. At the period of 60 s, Rayleigh wave phase speed possesses sensitivity to the upper mantle and displays high-velocity anomalies along the northern border of the GoM Coastal Plain and agrees well with our attenuation results (Figure 5b). Similarly, in the period range of 40 to 60 s, Gaite et al. (2012) obtain high-velocity anomalies in the SEUS using seismic ambient noise data. Another high resolution 3-D shear velocity model of the crust and uppermost mantle beneath Mexico and the southern U.S., constrained by Rayleigh wave group velocity measurements up to 90 s period, reveals higher seismic velocities in the SEUS relative to the southwestern U.S. in the uppermost mantle (Spica et al., 2016).

4.2. SPATIAL VARIATIONS OF SCATTERING

Scattering is an important factor that can lead to the decay of the amplitude because of the heterogeneity of the Earth's crust and mantle (Shapiro & Kneib, 1993). Most of the rocks and minerals contain heterogeneities in the form of grains, mineral boundaries, pore edges, cracks, etc., and the seismic energy is scattered when it encounters these features. Different modes of scattering are often determined based on the ratio between the scale of heterogeneity of the medium, a, and the wavelength (Wu & Aki, 1985).

$$S_r = 2\pi a \text{ / wavelength.} \quad (8)$$

A small S_r ($<< 0.01$) indicates that the size of the heterogeneities is extremely small relative to the seismic wavelength, leading to insignificant scattering. Scattering from heterogeneities with $0.01 < S_r < 0.1$ is termed as Rayleigh scattering, and that from heterogeneities with S_r in the range of 0.1 and 10 is termed as Mie scattering, which produces strong attenuation and distinguishable scattering in the seismic signal.

Theoretically, there should be zero energy on the transverse component of *P*-waves in an isotropic medium that is free of heterogeneities capable of producing scattering. Therefore, most of the energy in the *P*-wave window on the transverse component is the scattered energy due to 3-D heterogeneity. To examine the lateral variation of the strength of scattering, we calculated the ratio of the mean absolute amplitude between the transverse component and that of the vertical component for all the events that we used to estimate the Δt^*. We selected a signal window that is 5 s before and 10 s after, and a noise window that is 5-15 s before, the theoretical *P*-wave arrival time for both the vertical and transverse components. A bandpass filter with

corner frequencies of 0.1 Hz and 0.5 Hz is used, which is identical to the one used in Δt* calculation. The ratio of the noise normalized absolute mean amplitude between the transverse and vertical components is calculated for each of the event-station pairs using

$$Rtz = \frac{Ts \,/\, Tn}{Zs \,/\, Zn}, \tag{9}$$

where Z_s and T_s are the mean absolute vertical and transverse amplitudes in the signal window, and, Z_n and T_n are the mean absolute vertical and transverse amplitudes in the noise window, respectively.

The station-averaged *Rtz* measurements for the entire study area (Figure 8a) range from 0.086 to 0.424, with a mean value of 0.187 ± 0.040 s. The GoM Coastal Plain, which is an area characterized by low attenuation anomalies (Figure 5b), is dominated by low *Rtz* values. Patches of relatively high *Rtz* values are observed in the Appalachian Plateau, and the southwestern part of the Floridan Peninsula. To examine the intensity of scattering across the SEUS, we calculated the cross-correlation coefficient (XCC) between individual Δt* and *Rtz* measurements. A strong positive correlation between Δt* and *Rtz* values would reveal potential scattering artifacts, and zero or negative correlation would indicate that the Δt* values likely reflect intrinsic attenuation (Cafferky & Schmandt, 2015). High positive XCCs are observed near the Appalachian Mountains and northwest part of the Appalachian Plateau (Figure 8b), which is consistent with the scattering estimates obtained by Cafferky & Schmandt (2015) from T/Z spectral analysis of teleseismic *P*-waves in the frequency between 0.08 Hz and 0.4 Hz. Using receiver function, Schulte-Pelkum & Mahan (2014) report high scattering in the Appalachian Mountains. A recent study that uses the USArray data to estimate the crustal attenuation of high frequency (1-20 Hz) shear waves reports high scattering in parts of Interior Plains

and Appalachian Highlands (Eulenfeld & Wegler, 2017). They also report low scattering in the parts of the GoM Coastal Plain including the Lower Mississippi Region. The relatively low *Rtz* values and mostly negative XCCs observed along the GoM Coastal Plain in our study suggest a relatively more homogenous crustal and upper mantle structure in this area.

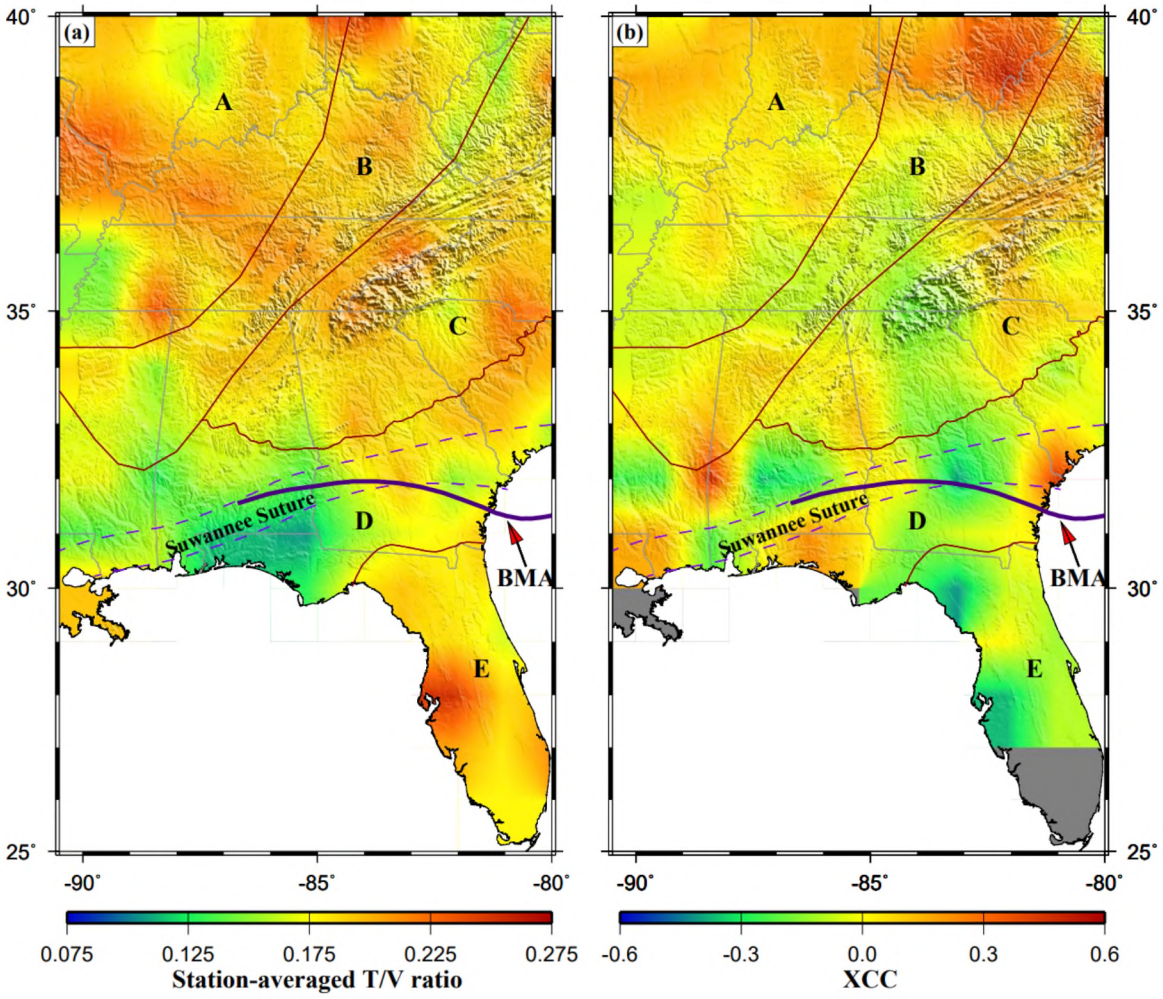

Figure 8. (a) Station-averaged transverse/vertical amplitude ratios. (b) Cross-correlation coefficient between individual t* measurements and transverse/vertical amplitude ratios at each station.

4.3. GEOGRAPHICAL VARIATIONS AND GEOLOGICAL IMPLICATIONS OF Δt*

The geographic variation of Δt* across the SEUS provides insights into the structure and dynamics of the upper mantle. The estimated Δt* measurements correspond with the *P*-wave velocity anomalies in the uppermost mantle (Figure 5a). The strongest correspondences include high Δt* in the Appalachians, where upper mantle velocities are low, and low Δt* in the GoM Coastal Plain where an E-W strip of high upper mantle velocities are reported in numerous velocity tomography studies (Bensen et al., 2008; Biryol et al., 2016; Gaite et al., 2012; Golos et al., 2018; Spica et al., 2016). Previous seismic studies have revealed mantle upwelling beneath several sections of the Appalachians along the eastern North American margin (Savage et al., 2017; Schmandt & Lin, 2014), and some of which are attributed to edge-driven convection (Menke et al., 2016). A recent study (Byrnes et al., 2019) estimates the upper mantle seismic attenuation beneath the Appalachian Mountains using the tight station spacing of 10 – 25 km. They interpret the high-attenuating upper mantle as the result of the removal of mantle lithosphere from a 100 km wide region beneath the central Appalachian Mountains.

The low attenuation anomaly observed beneath the GoM Coastal Plain lies within the proposed Suwannee suture zone (Thomas, 2011), and roughly coincides with the east-west trending BMA (Figure 5b) (Higgins & Zietz, 1983; Mueller et al., 2014; Williams & Hatcher, 1983). This magnetic anomaly located within the study area runs from Alabama across southern Georgia up to North Carolina's northern banks in the Atlantic Ocean. The source of the BMA is ambiguous because of its apparent connection with both the Permo-Carboniferous Alleghanian orogeny (330–270 Ma) and the volcanic rocks that caused the emplacement of the Central Atlantic Magmatic Province (~200 Ma). Lower crustal

seismic reflectors overlapping the location of magnetic low in southern Georgia (McBride & Nelson, 1988) and more recent magnetic models (Parker, 2014) suggest that the continental segment of the BMA can be explained by the collision of Laurentia and Gondwana. Seismic data have revealed the remnants of Pangea's breakup in the shallow crust near the BMA, providing evidence for the collision zone in the deep crust (Parker, 2014). Therefore, the low attenuation anomaly along the path of BMA can be explained by the presence of remnant lithospheric fragments in the deep crust or the uppermost mantle.

S-to-P receiver function studies using the USArray data (e.g., Hopper & Fischer, 2018; Liu & Gao, 2018) suggest that in the SEUS, the lithosphere has an average thickness of ~70 km, which is comparable to the estimated optimal depth of the weighted center of the anomalous attenuation layer (Figure 7). In addition, seismic tomography studies suggest a high velocity band approximately overlaps with the low attenuation zone along the GoM Coastal Plain in the depth range of ~20 to ~200 km relative to the Appalachians (Golos et al., 2020). Using the Qp values in the PREM model (Dziewonski & Anderson, 1981) for the remnant lithosphere (Q_L=1400) and the surrounding asthenosphere (Q_A=195), and Vp values of 8.1 km/s for the lithosphere (V_L) and 8.0 km/s for the asthenosphere (V_A), respectively, the required vertical length of the remnant lithospheric slab (R_L) in order to produce the observed -0.17 s ± 0.02 Δt^* value is as large as 305 ± 35 km which is inconsistent with results from seismic tomography studies. One way to produce a more reasonable R_L is to use a smaller Q_A value. For instance, when a Q_A value of 120 is used, R_L would reduce to ~180 ± 20 km which is more in accordance with tomography results (e.g., Golos et al., 2020). Additional studies are needed to isolate

the intrinsic attenuation from the observed total Δt^* and to more accurately determine the absolute Qp value for the proposed lithospheric segments and that of the ambient asthenosphere, in order to confirm the existence of the lithospheric segments and their spatial distribution.

5. CONCLUSIONS

We have utilized 14,702 teleseismic *P*-wave amplitude spectra recorded by 477 broadband seismic stations to map the spatial distribution of Δt^* in the SEUS. This large dataset of events recorded by the dense array of stations including 220 USArray TA stations provides a better constraint on the crustal and upper mantle *P*-wave attenuation structure than previous larger-scale attenuation studies. The resulting Δt^* measurements show a systematic contrast between the Appalachian Mountain range and the GoM Coastal Plain exhibiting high and low attenuation, respectively. An east-west strip of low attenuation anomaly is identified beneath most of the GoM Coastal Plain. The weighted center of this anomaly is located at about 70 km depth as estimated using the spatial coherency approach. This anomaly lies along the Suwannee suture zone that separated Laurentia and Gondwana during the Alleghanian orogeny. It also coincides with the path of the Brunswick Magnetic anomaly, providing evidence of low attenuation and fast velocity bodies in the upper-most mantle that are likely remnant lithospheric segments extending from the crust to the middle upper mantle. The ratio between the transverse and vertical amplitudes of the *P*-wave is calculated to estimate the lateral variation of scattering. Areas of relatively high transverse/vertical ratios are observed in the

Appalachian Plateau and the Floridan Peninsula, whereas low ratios observed in the GoM Coastal Plain indicate that this area is relatively less capable of producing scattering.

ACKNOWLEDGMENTS

The study was partially supported by the U.S. National Science Foundation under Grant No. 1919789. We thank two anonymous reviewers and Editor Maureen Long for providing thoughtful and constructive feedbacks that significantly improved the manuscript.

DATA AVAILABILITY STATEMENT

Station and event information, the measured Δt^* and its standard deviation (SD), as well as a plot similar to Figure 3 for each of the 14,702 measurements obtained in this study, can be found at https://web.mst.edu/~as6g7/1g_SEUS_tst/.

All the seismic waveform data used in this study were freely available from the Incorporated Research Institutions for Seismology Data Management Center (https://ds.iris.edu/ds/nodes/dmc/data/types/waveform-data/; last accessed: January 2019) under the main network codes of 6E (https://doi.org/10.7914/SN/6E_2013), IM (International Miscellaneous Stations), IU (https://doi.org/10.7914/SN/IU), N4 (https://doi.org/10.7914/SN/N4), NM (Cooperative New Madrid Seismic Network), PN (PEPP-Indiana), SP (https://doi.org/10.7914/SN/SP), TA (https://doi.org/10.7914/SN/TA), US (https://doi.org/10.7914/SN/US), XO

(https://doi.org/10.7914/SN/XO_2011), XR (https://doi.org/10.7914/SN/XR_2001), and Z9 (https://doi.org/10.7914/SN/Z9_2010).

APPENDIX

Table S1. Station averaged Δt^* measurements.

S. No.	Station Name	Latitude	Longitude	Δt^*	Std. dev. Δt^*	No. of Events
1	058Axx_TA	27.0569	-81.8049	0.073	0.138	8
2	059Axx_TA	26.9671	-81.144	0.1528	0.184	7
3	059Zxx_TA	26.3373	-81.4432	0.2917	0.2135	5
4	060Axx_TA	27.0361	-80.3618	0.114	0.1303	8
5	060Zxx_TA	26.4062	-80.556	0.087	0.106	5
6	061Zxx_TA	25.8657	-80.907	-0.0657	0.2697	3
7	145Axx_TA	32.6035	-89.9287	-0.2217	0.0643	23
8	146Axx_TA	32.6368	-89.0573	-0.4901	0.0701	10
9	147Axx_TA	32.6738	-88.2708	-0.4678	0.1321	6
10	148Axx_TA	32.6469	-87.571	-0.015	0.0809	18
11	149Axx_TA	32.5983	-86.7916	-0.0197	0.0607	22
12	150Axx_TA	32.6067	-86.022	0.3662	0.0598	23
13	151Axx_TA	32.5269	-85.3267	0.3656	0.0688	21
14	152Axx_TA	32.6686	-84.7188	0.2153	0.0545	31
15	153Axx_TA	32.6499	-83.8316	0.084	0.0432	37
16	154Axx_TA	32.6131	-83.1066	-0.3027	0.0364	31

Table S1. Station averaged Δt^* measurements. (cont.)

S. No.	Station Name	Latitude	Longitude	Δt^*	Std. dev. Δt^*	No. of Events
17	155Axx_TA	32.6219	-82.4665	-0.1647	0.0468	29
18	156Axx_TA	32.6542	-81.495	-0.4656	0.0779	18
19	157Axx_TA	32.678	-80.9972	-0.3997	0.0729	15
20	158Axx_TA	32.7364	-80.1935	-0.5878	0.0813	9
21	245Axx_TA	32.0322	-89.8958	-0.274	0.079	17
22	246Axx_TA	32.0143	-89.1286	-0.3074	0.0641	21
23	247Axx_TA	32.053	-88.6102	-0.0975	0.0466	18
24	248Axx_TA	32.094	-87.7393	-0.4827	0.0818	10
25	249Axx_TA	31.9752	-87.1225	-0.579	0.104	6
26	250Axx_TA	31.9778	-86.2677	-0.4328	0.0619	22
27	251Axx_TA	32.0929	-85.409	-0.2679	0.0538	20
28	252Axx_TA	31.9962	-84.7357	-0.2415	0.0549	21
29	253Axx_TA	32.0612	-84.1294	-0.3814	0.0474	17
30	254Axx_TA	31.9457	-83.2905	-0.4376	0.0726	18
31	255Axx_TA	31.9263	-82.4758	-0.4291	0.0756	17
32	256Axx_TA	31.9799	-81.8878	-0.3975	0.0638	17
33	257Axx_TA	31.9746	-81.0261	-0.4415	0.0653	13
34	346Axx_TA	31.3876	-89.4649	0.0678	0.1374	9
35	347Axx_TA	31.4017	-88.5412	0.0121	0.0934	10
36	348Axx_TA	31.4129	-87.9023	-0.0856	0.0407	27

Table S1. Station averaged Δt^* measurements. (cont.)

S. No.	Station Name	Latitude	Longitude	Δt^*	Std. dev. Δt^*	No. of Events
37	349Axx_TA	31.3504	-87.1924	-0.0321	0.0744	12
38	350Axx_TA	31.4207	-86.3353	-0.0936	0.076	18
39	351Axx_TA	31.2753	-85.6036	-0.4343	0.0967	12
40	352Axx_TA	31.4793	-84.9274	-0.5438	0.0557	18
41	353Axx_TA	31.3474	-84.2172	-0.3404	0.0644	15
42	355Axx_TA	31.3438	-82.8518	-0.4866	0.0825	12
43	356Axx_TA	31.3247	-82.1275	-0.3119	0.0824	10
44	357Axx_TA	31.4239	-81.4855	-0.3461	0.0756	14
45	446Axx_TA	30.7912	-89.3645	-0.0864	0.0659	19
46	447Axx_TA	30.7952	-88.6542	-0.0561	0.0993	11
47	448Axx_TA	30.9309	-87.8608	-0.1445	0.0616	22
48	449Axx_TA	30.7596	-87.2151	-0.2791	0.0666	17
49	450Axx_TA	30.8038	-86.5863	-0.0261	0.1015	12
50	451Axx_TA	30.616	-85.7467	-0.2752	0.0817	9
51	452Axx_TA	30.8492	-85.183	-0.1162	0.0834	14
52	453Axx_TA	30.8541	-84.3197	0.0288	0.0648	18
53	454Axx_TA	30.7145	-83.6302	0.0601	0.0787	16
54	455Axx_TA	30.7422	-83.026	-0.1937	0.0755	14
55	456Axx_TA	30.7248	-82.0223	-0.0102	0.064	18
56	457Axx_TA	30.6199	-81.5563	0.1148	0.0874	17

Table S1. Station averaged Δt^* measurements. (cont.)

S. No.	Station Name	Latitude	Longitude	Δt^*	Std. dev. Δt^*	No. of Events
57	546Axx_TA	30.233	-89.7191	0.0139	0.061	8
58	552Axx_TA	30.1327	-85.2938	0.1958	0.1034	7
59	553Axx_TA	30.189	-84.4317	-0.0336	0.1055	14
60	554Axx_TA	30.0841	-83.6836	-0.1948	0.1094	11
61	555Axx_TA	30.1212	-82.9666	-0.2171	0.0821	14
62	556Axx_TA	30.0015	-82.4057	-0.0131	0.0642	17
63	557Axx_TA	30.016	-81.7291	-0.011	0.1045	13
64	646Axx_TA	29.5832	-89.8245	-0.013	0.1629	3
65	655Axx_TA	29.5107	-83.2552	-0.1652	0.087	12
66	656Axx_TA	29.3689	-82.5348	-0.0114	0.0638	15
67	657Axx_TA	29.5852	-81.8665	0.0604	0.095	10
68	658Axx_TA	29.422	-81.2578	-0.0686	0.0831	16
69	757Axx_TA	28.9413	-82.0685	-0.0785	0.0741	13
70	758Axx_TA	28.9621	-81.1996	-0.2399	0.1135	11
71	857Axx_TA	28.267	-82.2291	-0.0929	0.0769	14
72	858Axx_TA	28.2126	-81.3616	-0.1881	0.0721	6
73	859Axx_TA	28.0592	-80.8984	0.0205	0.0956	10
74	957Axx_TA	27.6702	-82.2357	0.0169	0.0768	10
75	958Axx_TA	27.5855	-81.7543	0.1662	0.1317	9
76	959Axx_TA	27.524	-80.8791	0.012	0.0887	10

Table S1. Station averaged Δt^* measurements. (cont.)

S. No.	Station Name	Latitude	Longitude	Δt^*	Std. dev. Δt^*	No. of Events
77	ACFLRx_SP	34.0165	-80.9829	0.3186	0.0602	16
78	AGBLFx_SP	33.395	-81.758	0.1479	0.0504	22
79	BBLVxx_SP	33.9234	-81.5347	0.0387	0.0512	23
80	BLACKx_SP	33.364	-81.2635	-0.05	0.0402	26
81	BLAxxx_US	37.2113	-80.4205	0.0414	0.0266	124
82	BLOxxx_NM	39.1719	-86.5222	-0.0813	0.0177	222
83	BRALxx_US	31.1687	-87.0506	-0.0756	0.0286	100
84	BRNCHx_SP	33.2465	-80.7904	-0.2297	0.0436	11
85	BTRCKx_SP	32.432	-80.7476	-0.3371	0.0913	3
86	CLINTx_SP	34.4811	-81.8628	0.1642	0.0594	13
87	CLOVEx_SP	35.0969	-81.1842	0.1274	0.2151	5
88	D02xxx_Z9	33.6041	-82.2828	0.1543	0.0405	44
89	D03xxx_Z9	33.6594	-82.3884	0.0861	0.0416	39
90	D04xxx_Z9	33.7301	-82.4518	0.1677	0.0461	32
91	D05xxx_Z9	33.7915	-82.5159	0.1853	0.0445	48
92	D06xxx_Z9	33.859	-82.6304	0.0563	0.07	25
93	D07xxx_Z9	33.9376	-82.6864	0.1785	0.0556	34
94	D08xxx_Z9	33.9938	-82.7566	0.1636	0.0503	26
95	D09xxx_Z9	34.0448	-82.8278	0.2385	0.0551	38
96	D10xxx_Z9	34.0917	-82.9032	0.2317	0.066	22

Table S1. Station averaged Δt^* measurements. (cont.)

S. No.	Station Name	Latitude	Longitude	Δt^*	Std. dev. Δt^*	No. of Events
97	D11xxx_Z9	34.1565	-82.9731	0.3228	0.0388	46
98	D12xxx_Z9	34.2462	-83.0333	0.1716	0.0571	38
99	D13xxx_Z9	34.2943	-83.1662	0.1746	0.0446	45
100	D14xxx_Z9	34.3765	-83.1811	0.1239	0.0362	54
101	D15xxx_Z9	34.4498	-83.2799	0.1023	0.0361	52
102	D17xxx_Z9	34.6044	-83.4507	0.248	0.0283	54
103	D18xxx_Z9	34.7342	-83.6121	0.2319	0.0556	33
104	D19xxx_Z9	34.8721	-83.7338	0.3796	0.0524	37
105	D20xxx_Z9	35.074	-83.9803	0.2509	0.0522	39
106	D21xxx_Z9	35.1997	-84.1369	0.2332	0.0396	37
107	D22xxx_Z9	35.4629	-84.4588	0.2096	0.0491	33
108	DFORKx_SP	34.1531	-81.2003	0.133	0.0911	9
109	DWDANx_SP	34.7388	-82.8308	0.152	0.0372	23
110	DWPFxx_IU	28.1103	-81.4327	-0.0491	0.0338	80
111	E01xxx_Z9	29.2116	-82.0545	0.0675	0.0859	13
112	E02xxx_Z9	29.443	-82.0674	-0.0827	0.0755	19
113	E03xxx_Z9	29.8296	-82.1318	-0.0622	0.0687	17
114	E04xxx_Z9	30.0271	-82.1095	-0.0559	0.1105	13
115	E05xxx_Z9	30.3617	-82.1176	-0.0842	0.0747	13
116	E06xxx_Z9	30.5853	-82.0999	-0.0888	0.0773	13

Table S1. Station averaged Δt^* measurements. (cont.)

S. No.	Station Name	Latitude	Longitude	Δt^*	Std. dev. Δt^*	No. of Events
117	E07xxx_Z9	30.718	-82.0979	-0.1272	0.0618	13
118	E08xxx_Z9	30.8388	-82.0717	-0.2775	0.0708	16
119	E09xxx_Z9	30.9839	-82.0742	-0.2695	0.0757	17
120	E10xxx_Z9	31.0673	-82.1013	-0.3268	0.0753	18
121	E11xxx_Z9	31.1074	-82.1019	-0.3686	0.1784	4
122	E12xxx_Z9	31.1733	-82.088	-0.4763	0.0942	5
123	E13xxx_Z9	31.223	-82.0919	-0.476	0.0672	13
124	E15xxx_Z9	31.3632	-82.0969	-0.5041	0.0388	15
125	E16xxx_Z9	31.4505	-82.1299	-0.3544	0.0563	16
126	E17xxx_Z9	31.5016	-82.0986	-0.3692	0.0427	9
127	E18xxx_Z9	31.5665	-82.0996	-0.3381	0.0506	17
128	E19xxx_Z9	31.6177	-82.1113	-0.3944	0.0641	15
129	E20xxx_Z9	31.6967	-82.0796	-0.3871	0.0509	18
130	E21xxx_Z9	31.738	-82.071	-0.4302	0.0708	12
131	E22xxx_Z9	31.8477	-82.0899	-0.5031	0.0603	5
132	E23xxx_Z9	31.8887	-82.0737	-0.1703	0.068	6
133	E24xxx_Z9	31.9445	-82.097	-0.401	0.0521	27
134	E25xxx_Z9	31.9918	-82.1135	-0.304	0.067	22
135	E26xxx_Z9	32.0979	-82.0991	-0.2384	0.0711	14
136	E27xxx_Z9	32.2362	-82.1091	-0.2603	0.0949	6

Table S1. Station averaged Δt^* measurements. (cont.)

S. No.	Station Name	Latitude	Longitude	Δt^*	Std. dev. Δt^*	No. of Events
137	E28xxx_Z9	32.3359	-82.0967	-0.23	0.073	16
138	E29xxx_Z9	32.4908	-82.1032	-0.1252	0.0619	25
139	E30xxx_Z9	32.6958	-82.1091	-0.0194	0.0449	35
140	E31xxx_Z9	32.9866	-82.107	0.0639	0.0529	38
141	EDGExx_SP	33.8073	-81.863	0.3785	0.0722	12
142	FA01xx_XR	29.9167	-82.5827	-0.04	0.1028	8
143	FA02xx_XR	31.1732	-83.5344	-0.609	0.0628	8
144	FA03xx_XR	32.0549	-84.2152	-0.1813	0.1953	4
145	FA04xx_XR	32.751	-84.9206	0.0611	0.0613	18
146	FA05xx_XR	33.5728	-85.1095	0.0633	0.0768	15
147	FA06xx_XR	33.9848	-85.9924	-0.1432	0.076	8
148	FA07xx_XR	34.7312	-86.7104	-0.0106	0.0679	17
149	FA08xx_XR	37.3156	-89.5293	0.1349	0.0865	13
150	FFILxx_NM	38.3813	-88.3896	-0.0977	0.0313	110
151	GOGAxx_US	33.4112	-83.4666	0.3312	0.0204	179
152	GREENx_SP	34.23	-82.1743	0.4718	0.0681	10
153	KF28xx_XO	37.7532	-87.8091	-0.0591	0.058	25
154	KF30xx_XO	37.8847	-87.3937	-0.0992	0.0451	32
155	KF34xx_XO	37.823	-86.8078	-0.0506	0.0447	27
156	KG27xx_XO	37.6473	-87.9012	-0.1059	0.0563	38

Table S1. Station averaged Δt^* measurements. (cont.)

S. No.	Station Name	Latitude	Longitude	Δt^*	Std. dev. Δt^*	No. of Events
157	KG29xx_XO	37.7179	-87.4726	-0.0306	0.0668	27
158	KG31xx_XO	37.653	-87.1805	0.0532	0.0457	40
159	KG35xx_XO	37.6431	-86.6141	0.1691	0.0311	38
160	KG37xx_XO	37.6568	-86.2797	0.1046	0.0488	39
161	KG41xx_XO	37.6661	-85.7428	0.1914	0.0892	21
162	KH26xx_XO	37.4567	-88.0082	0.182	0.0536	35
163	KH28xx_XO	37.4789	-87.7108	-0.0346	0.0542	23
164	KH30xx_XO	37.4706	-87.4643	0.0678	0.0613	25
165	KH32xx_XO	37.4233	-87.2761	0.3185	0.0381	29
166	KH34xx_XO	37.474	-86.9269	0.4056	0.0522	23
167	KH36xx_XO	37.4722	-86.6131	0.6038	0.0442	12
168	KH38xx_XO	37.3921	-86.3046	0.2817	0.0588	26
169	KH42xx_XO	37.4933	-85.7235	0.1136	0.0651	25
170	KH44xx_XO	37.502	-85.4645	-0.12	0.0435	22
171	KH46xx_XO	37.4669	-85.2482	-0.1294	0.0692	26
172	KH48xx_XO	37.4455	-85.0052	-0.0627	0.0493	29
173	KH49xx_XO	37.437	-84.7353	-0.193	0.0605	26
174	KH50xx_XO	37.417	-84.4633	0.0806	0.0566	34
175	KH54xx_XO	37.4149	-84.16	-0.0697	0.0536	37
176	KH56xx_XO	37.3148	-83.9502	0.0942	0.0653	20

Table S1. Station averaged Δt^* measurements. (cont.)

S. No.	Station Name	Latitude	Longitude	Δt^*	Std. dev. Δt^*	No. of Events
177	KI25xx_XO	37.2912	-88.1118	0.069	0.0522	35
178	KI27xx_XO	37.2642	-87.8269	0.2568	0.063	23
179	KI29xx_XO	37.2731	-87.5576	0.357	0.0729	18
180	KI31xx_XO	37.2529	-87.2858	0.2105	0.0535	30
181	KI33xx_XO	37.3191	-86.9601	0.2834	0.0424	30
182	KI35xx_XO	37.2954	-86.6963	0.2139	0.0688	22
183	KI37xx_XO	37.2561	-86.389	0.1073	0.0679	21
184	KI39Ax_XO	37.2964	-86.1756	0.257	0.1154	15
185	KI39xx_XO	37.2944	-86.0838	0.1883	0.103	14
186	KI41xx_XO	37.2992	-85.817	-0.0276	0.0543	33
187	KI43xx_XO	37.2805	-85.5691	-0.1126	0.0439	27
188	KI45xx_XO	37.2665	-85.2339	-0.0169	0.0488	28
189	KI47xx_XO	37.2462	-84.9904	-0.0254	0.048	32
190	KI49xx_XO	37.2207	-84.7498	0.0039	0.0318	45
191	KI51xx_XO	37.1857	-84.5075	-0.083	0.0527	30
192	KI53xx_XO	37.1845	-84.2061	0.0032	0.0514	20
193	KJ30xx_XO	37.0871	-87.3385	0.0215	0.047	38
194	KJ34xx_XO	37.1098	-86.9234	-0.1031	0.0435	47
195	KJ36xx_XO	37.1025	-86.587	-0.036	0.0543	37
196	KJ40xx_XO	37.1449	-86.0187	-0.1527	0.0549	34

Table S1. Station averaged Δt^* measurements. (cont.)

S. No.	Station Name	Latitude	Longitude	Δt^*	Std. dev. Δt^*	No. of Events
197	KJ42xx_XO	37.1185	-85.7507	-0.0158	0.0566	27
198	KJ46xx_XO	37.0821	-85.3614	-0.0186	0.0474	33
199	KJ48xx_XO	37.0498	-85.0474	0.0594	0.0717	29
200	KJ50xx_XO	37.0462	-84.5808	0.0977	0.0478	35
201	KJ52xx_XO	36.9186	-84.25	-0.127	0.04	41
202	KK34xx_XO	36.9081	-86.8208	-0.0542	0.0568	30
203	KK36xx_XO	36.9355	-86.5777	-0.0626	0.0455	36
204	KK38xx_XO	36.903	-86.2871	-0.0634	0.0614	24
205	KK40xx_XO	36.8802	-86.0141	-0.1243	0.0492	33
206	KK42xx_XO	36.9034	-85.7403	-0.0302	0.0478	30
207	KK44xx_XO	36.9076	-85.4932	-0.1219	0.0405	29
208	KK46xx_XO	36.8709	-85.2468	-0.1296	0.0499	25
209	KK48xx_XO	36.8672	-84.9442	0.2265	0.0583	22
210	KK50xx_XO	36.8694	-84.8024	0.1254	0.0485	37
211	KK52xx_XO	36.8372	-84.5091	-0.0486	0.0762	17
212	KMSCxx_TA	35.142	-81.3333	0.0765	0.0296	125
213	LA17xx_XO	38.6334	-89.1377	-0.1413	0.07	16
214	LA19xx_XO	38.6944	-88.8699	-0.0661	0.0638	23
215	LA21xx_XO	38.7749	-88.5598	-0.1964	0.0814	18
216	LB16xx_XO	38.475	-89.3121	0.2289	0.0857	17

Table S1. Station averaged Δt^* measurements. (cont.)

S. No.	Station Name	Latitude	Longitude	Δt^*	Std. dev. Δt^*	No. of Events
217	LB18xx_XO	38.4544	-89.0516	-0.2049	0.0424	20
218	LB20xx_XO	38.5256	-88.752	-0.0247	0.0526	20
219	LB22xx_XO	38.5073	-88.488	0.0369	0.0835	21
220	LB24xx_XO	38.5057	-88.2059	-0.0721	0.0833	10
221	LB26xx_XO	38.5122	-87.9705	-0.1348	0.0523	22
222	LC15xx_XO	38.2974	-89.4124	-0.2343	0.0548	29
223	LC19xx_XO	38.3611	-88.8554	-0.1507	0.0525	26
224	LC21xx_XO	38.3129	-88.6176	0.0365	0.08	19
225	LC25xx_XO	38.3224	-87.9882	-0.0153	0.0642	21
226	LD12xx_XO	38.1506	-89.9279	-0.0516	0.0655	21
227	LD14xx_XO	38.1305	-89.6138	-0.1141	0.0402	29
228	LD16xx_XO	38.1552	-89.3221	-0.2097	0.0448	20
229	LD18xx_XO	38.1654	-89.1138	-0.0852	0.0909	15
230	LD20xx_XO	38.1485	-88.8538	-0.204	0.0466	25
231	LD22xx_XO	38.1394	-88.4326	-0.1957	0.0544	22
232	LD24xx_XO	38.184	-88.2267	0.0142	0.0789	11
233	LE13xx_XO	37.974	-89.7496	-0.0981	0.0528	25
234	LE15xx_XO	37.9616	-89.4867	-0.0512	0.0401	27
235	LE17xx_XO	37.9874	-89.1763	-0.0791	0.0449	27
236	LE19xx_XO	38.0065	-88.8787	-0.0758	0.0437	31

Table S1. Station averaged Δt^* measurements. (cont.)

S. No.	Station Name	Latitude	Longitude	Δt^*	Std. dev. Δt^*	No. of Events
237	LE21xx_XO	37.9939	-88.6868	-0.3581	0.0481	22
238	LE23xx_XO	38.0293	-88.3642	-0.2915	0.063	20
239	LE25xx_XO	38.0006	-88.034	-0.1189	0.0514	25
240	LF16xx_XO	37.8216	-89.5137	-0.1486	0.0426	24
241	LF18xx_XO	37.7818	-89.1733	-0.0651	0.0507	24
242	LF20xx_XO	37.7822	-88.8262	0.018	0.0573	20
243	LF22xx_XO	37.7764	-88.5971	-0.1671	0.0727	18
244	LF24xx_XO	37.8302	-88.3871	-0.2204	0.0555	23
245	LF26xx_XO	37.745	-88.13	-0.1883	0.0474	44
246	LG19xx_XO	37.5957	-89.0459	-0.0222	0.0391	40
247	LG21xx_XO	37.6691	-88.7941	0.0935	0.042	40
248	LG25Ax_XO	37.6625	-88.4588	-0.0181	0.0418	31
249	LG25xx_XO	37.6639	-88.4557	0.0931	0.1031	6
250	LGELGx_SP	34.2175	-80.7092	0.2457	0.1028	10
251	LH16xx_XO	37.4427	-89.3084	0.1649	0.0637	20
252	LH18xx_XO	37.4132	-89.104	0.0561	0.0564	24
253	LH20xx_XO	37.5179	-88.8349	-0.064	0.0488	27
254	LH22xx_XO	37.4976	-88.5491	0.2919	0.0446	18
255	LH24xx_XO	37.4818	-88.2727	0.0407	0.0589	30
256	LI21xx_XO	37.2764	-88.6512	-0.0241	0.061	24

Table S1. Station averaged Δt^* measurements. (cont.)

S. No.	Station Name	Latitude	Longitude	Δt^*	Std. dev. Δt^*	No. of Events
257	LOKYxx_XO	37.2366	-88.2946	0.0323	0.0637	28
258	LRALxx_US	33.0399	-86.9978	0.3203	0.0288	127
259	MF14xx_XO	37.8018	-89.8023	0.0304	0.0478	21
260	MG13xx_XO	37.5888	-89.882	0.2399	0.0707	30
261	MG15Ax_XO	37.5766	-89.5748	-0.0331	0.0798	16
262	MG15xx_XO	37.5623	-89.5996	0.0179	0.0807	15
263	MH14xx_XO	37.4537	-89.7244	0.0547	0.068	15
264	MPHxxx_NM	35.123	-89.932	-0.4393	0.0217	159
265	MYNCxx_US	35.0739	-84.1279	0.2354	0.0473	5
266	NB28xx_XO	38.4148	-87.6073	0.0851	0.0477	25
267	NC27xx_XO	38.2883	-87.7544	-0.0171	0.0594	22
268	NC29xx_XO	38.3182	-87.503	0.0087	0.0445	22
269	NC31xx_XO	38.3512	-87.2219	0.1548	0.0617	22
270	NC33xx_XO	38.318	-87.0238	0.1185	0.061	29
271	ND26xx_XO	38.2196	-87.9203	-0.0586	0.0581	17
272	ND28xx_XO	38.0787	-87.6839	-0.1176	0.0486	19
273	ND30xx_XO	38.1215	-87.2793	0.1476	0.0521	35
274	ND32xx_XO	38.1662	-87.0638	0.1125	0.0542	34
275	NE27xx_XO	37.966	-87.8226	-0.2043	0.0489	36
276	NE29xx_XO	38.0455	-87.419	-0.0267	0.0603	29

Table S1. Station averaged Δt^* measurements. (cont.)

S. No.	Station Name	Latitude	Longitude	Δt^*	Std. dev. Δt^*	No. of Events
277	NE31xx_XO	37.9743	-87.1727	0.017	0.0519	29
278	NE33xx_XO	38.0408	-86.878	0.0829	0.0437	35
279	NHSCxx_US	33.1067	-80.1778	-0.2311	0.0316	109
280	OLARxx_SP	33.3264	-81.1311	0.1662	0.0627	10
281	OLILxx_NM	38.7338	-88.0991	-0.0543	0.0177	219
282	OXFxxx_US	34.5118	-89.4092	-0.1726	0.0236	184
283	P43Axx_TA	39.6409	-89.5213	-0.0676	0.0407	41
284	P44Axx_TA	39.4676	-88.6209	-0.1304	0.0521	30
285	P45Axx_TA	39.5277	-87.7439	0.0891	0.0634	27
286	P46Axx_TA	39.6178	-87.2067	-0.0795	0.0495	29
287	P47Axx_TA	39.4869	-86.2699	0.0181	0.0432	23
288	P48Axx_TA	39.4605	-85.4258	-0.192	0.0574	30
289	P49Axx_TA	39.5342	-84.7164	-0.0324	0.033	79
290	P50Axx_TA	39.6086	-83.7988	-0.0539	0.043	33
291	P51Axx_TA	39.4818	-83.0601	0.0979	0.0548	32
292	P52Axx_TA	39.6337	-82.1325	0.0285	0.0384	59
293	P53Axx_TA	39.4868	-81.3896	-0.154	0.0524	27
294	P54Axx_TA	39.602	-80.4796	-0.1427	0.0448	24
295	PLALxx_NM	34.9824	-88.0755	0.1369	0.0198	205
296	PPHHSx_PN	37.972	-87.486	0.0479	0.0809	7

Table S1. Station averaged Δt^* measurements. (cont.)

S. No.	Station Name	Latitude	Longitude	Δt^*	Std. dev. Δt^*	No. of Events
297	PVMOxx_NM	36.4137	-89.6997	-0.1764	0.0211	203
298	Q43Axx_TA	38.941	-89.6991	-0.138	0.0383	33
299	Q44Axx_TA	38.9032	-89.017	0.1	0.0539	22
300	Q45Axx_TA	38.8948	-88.1565	-0.0011	0.0642	30
301	Q46Axx_TA	39.0231	-87.3575	-0.0145	0.0466	24
302	Q47Axx_TA	38.9362	-86.4261	-0.1159	0.0725	19
303	Q48Axx_TA	38.9295	-85.7311	-0.0488	0.0498	27
304	Q49Axx_TA	39.005	-84.8956	-0.0048	0.0533	22
305	Q50Axx_TA	38.8436	-83.979	-0.099	0.0573	29
306	Q51Axx_TA	39.026	-83.3456	0.1241	0.0622	32
307	Q52Axx_TA	38.9622	-82.2669	0.0388	0.0483	32
308	Q53Axx_TA	38.8586	-81.5251	-0.049	0.054	24
309	Q54Axx_TA	38.9836	-80.8338	0.0791	0.1632	14
310	Q55Axx_TA	38.9952	-80.0812	-0.1662	0.0681	9
311	R43Axx_TA	38.276	-89.9308	-0.0622	0.0525	27
312	R44Axx_TA	38.2475	-89.0809	0.041	0.0416	34
313	R45Axx_TA	38.2926	-88.2812	-0.0136	0.0571	27
314	R46Axx_TA	38.2124	-87.5114	0.0023	0.0503	33
315	R47Axx_TA	38.2957	-86.527	-0.0385	0.0491	23
316	R48Axx_TA	38.4001	-85.8714	0.0463	0.0631	24

Table S1. Station averaged Δt^* measurements. (cont.)

S. No.	Station Name	Latitude	Longitude	Δt^*	Std. dev. Δt^*	No. of Events
317	R49Axx_TA	38.2916	-85.1714	0.0722	0.0361	30
318	R50Axx_TA	38.2816	-84.3274	0.1536	0.0531	29
319	R51Axx_TA	38.3001	-83.5834	0.0369	0.0543	36
320	R52Axx_TA	38.3366	-82.6443	0.0846	0.082	23
321	R53Axx_TA	38.3307	-81.9522	0.2746	0.0854	23
322	R54Axx_TA	38.1909	-80.9904	-0.1707	0.0345	20
323	R55Axx_TA	38.2825	-80.1195	0.002	0.0549	19
324	RUFINx_SP	33.0122	-80.8065	0.0027	0.06	6
325	S44Axx_TA	37.6936	-89.2551	0.0399	0.0337	59
326	S45Axx_TA	37.6774	-88.5804	0.0051	0.0495	42
327	S46Axx_TA	37.6849	-87.7153	-0.0429	0.0367	34
328	S47Axx_TA	37.5946	-86.8779	0.2147	0.0512	20
329	S48Axx_TA	37.6574	-86.0569	0.0624	0.0601	21
330	S49Axx_TA	37.7849	-85.2875	0.0193	0.0447	43
331	S50Axx_TA	37.679	-84.4003	-0.0633	0.0451	40
332	S51Axx_TA	37.6392	-83.5935	0.2798	0.0452	23
333	S52Axx_TA	37.6791	-83.0784	0.388	0.0813	23
334	S53Axx_TA	37.6815	-82.1264	-0.0957	0.0676	22
335	S54Axx_TA	37.7997	-81.3114	0.0172	0.0718	16
336	S55Axx_TA	37.7724	-80.5013	-0.0999	0.0933	19

Table S1. Station averaged Δt^* measurements. (cont.)

S. No.	Station Name	Latitude	Longitude	Δt^*	Std. dev. Δt^*	No. of Events
337	SCOTTx_SP	33.6152	-80.3228	-0.2027	0.0253	5
338	SIUCxx_NM	37.7148	-89.2174	-0.028	0.0178	302
339	SOKYxx_XO	37.5256	-85.9619	0.2483	0.0495	32
340	SUMMRx_SP	32.9944	-80.219	-0.6271	0.0372	4
341	T44Axx_TA	37.086	-89.5896	0.0886	0.0474	35
342	T45Axx_TA	37.0196	-88.6447	0.1808	0.0381	31
343	T45Bxx_N4	37.0159	-88.6459	-0.0495	0.032	94
344	T46Axx_TA	37.0417	-87.8941	0.3292	0.0497	17
345	T47Axx_TA	36.9881	-87.1055	-0.2442	0.0405	52
346	T48Axx_TA	37.1094	-86.3943	0.2649	0.0719	23
347	T49Axx_TA	37.105	-85.5334	0.0586	0.0362	51
348	T50Axx_TA	37.0204	-84.8384	0.067	0.0278	47
349	T51Axx_TA	36.9655	-83.9454	-0.0512	0.0454	39
350	T52Axx_TA	37.1076	-82.9852	0.1323	0.084	25
351	T53Axx_TA	36.9823	-82.535	0.0707	0.0568	32
352	T54Axx_TA	37.0608	-81.5762	0.3278	0.0626	25
353	T55Axx_TA	37.117	-80.7843	-0.0497	0.0669	29
354	T56Axx_TA	37.0288	-80.0311	-0.0036	0.0551	25
355	TIGAxx_TA	31.4389	-83.5898	-0.2982	0.0306	82
356	TKLxxx_IM	35.658	-83.774	0.1996	0.0256	133

Table S1. Station averaged Δt^* measurements. (cont.)

S. No.	Station Name	Latitude	Longitude	Δt^*	Std. dev. Δt^*	No. of Events
357	TZTNxx_US	36.5439	-83.549	0.1886	0.0228	146
358	U44Axx_TA	36.5047	-89.6863	-0.146	0.0518	30
359	U44Bxx_TA	36.3391	-89.3507	0.0369	0.0567	18
360	U45Axx_TA	36.3481	-88.7635	0.1961	0.0524	25
361	U46Axx_TA	36.359	-88.1773	0.2836	0.0485	29
362	U47Axx_TA	36.4413	-87.2892	0.0694	0.0459	37
363	U48Axx_TA	36.5107	-86.5402	0.1891	0.0548	29
364	U49Axx_TA	36.5129	-85.7796	0.1774	0.0496	36
365	U50Axx_TA	36.4156	-84.8431	-0.0851	0.0379	39
366	U51Axx_TA	36.3786	-84.0165	0.0997	0.0564	25
367	U52Axx_TA	36.3929	-83.3671	0.237	0.076	20
368	U53Axx_TA	36.3644	-82.5765	0.2041	0.0548	25
369	U54Axx_TA	36.5209	-81.8204	0.045	0.0569	31
370	U55Axx_TA	36.5023	-81.0472	0.1462	0.0589	29
371	U56Axx_TA	36.3472	-80.3829	0.1032	0.0633	23
372	USINxx_NM	37.965	-87.666	-0.0573	0.0158	252
373	V44Axx_TA	35.8282	-89.8954	-0.0917	0.0455	31
374	V45Axx_TA	35.7403	-88.9591	0.0949	0.0585	31
375	V46Axx_TA	35.8007	-88.1177	0.247	0.0717	18
376	V47Axx_TA	35.8278	-87.5205	0.262	0.0761	22

Table S1. Station averaged Δt^* measurements. (cont.)

S. No.	Station Name	Latitude	Longitude	Δt^*	Std. dev. Δt^*	No. of Events
377	V48Axx_TA	35.74	-86.8219	0.1105	0.0676	31
378	V49Axx_TA	35.7663	-85.903	0.2423	0.0412	27
379	V50Axx_TA	35.6713	-85.1	0.0984	0.048	33
380	V51Axx_TA	35.8033	-84.3511	0.2303	0.0549	22
381	V52Axx_TA	35.8417	-83.5959	0.1187	0.0732	24
382	V53Axx_TA	35.6694	-82.8124	0.2282	0.0835	16
383	V54Axx_TA	35.7771	-81.9478	0.1469	0.0602	26
384	V55Axx_TA	35.8518	-81.2149	0.1399	0.0515	27
385	V56Axx_TA	35.8097	-80.4963	-0.0181	0.048	30
386	W01xxx_Z9	30.2017	-83.9109	-0.2019	0.0641	22
387	W02xxx_Z9	30.5774	-83.8902	-0.1806	0.0858	21
388	W03xxx_Z9	30.8635	-83.8864	-0.1153	0.0675	20
389	W04xxx_Z9	31.0831	-83.8952	-0.1218	0.0848	17
390	W05xxx_Z9	31.2724	-83.8978	-0.1533	0.0565	21
391	W06xxx_Z9	31.4486	-83.895	-0.2513	0.0615	20
392	W07xxx_Z9	31.611	-83.911	-0.2099	0.062	22
393	W08xxx_Z9	31.7165	-83.886	-0.3487	0.0587	19
394	W09xxx_Z9	31.8051	-83.8981	-0.5254	0.042	22
395	W10xxx_Z9	31.9025	-83.8937	-0.4936	0.0402	19
396	W11xxx_Z9	31.9587	-83.9083	-0.3838	0.0443	22

Table S1. Station averaged Δt^* measurements. (cont.)

S. No.	Station Name	Latitude	Longitude	Δt^*	Std. dev. Δt^*	No. of Events
397	W12xxx_Z9	32.0095	-83.8885	-0.3154	0.0911	8
398	W13xxx_Z9	32.055	-83.8933	-0.2228	0.0684	22
399	W14xxx_Z9	32.0938	-83.8987	-0.2673	0.0461	16
400	W15Axx_Z9	32.138	-83.8985	-0.0157	0.0359	26
401	W16xxx_Z9	32.1794	-83.8841	0.0717	0.0621	19
402	W17xxx_Z9	32.2427	-83.9045	-0.0836	0.0589	13
403	W18xxx_Z9	32.2725	-83.9017	-0.0854	0.0412	30
404	W19xxx_Z9	32.3132	-83.9064	0.0621	0.0415	27
405	W20xxx_Z9	32.3665	-83.9198	0.0453	0.0787	22
406	W21xxx_Z9	32.404	-83.8587	0.1256	0.0389	40
407	W22xxx_Z9	32.4492	-83.8973	0.2236	0.0537	30
408	W23xxx_Z9	32.5234	-83.886	0.1164	0.0442	35
409	W24xxx_Z9	32.6437	-83.8967	0.0255	0.049	32
410	W26xxx_Z9	32.7886	-83.8917	0.094	0.0602	17
411	W27xxx_Z9	32.9174	-83.9234	0.1862	0.04	60
412	W28xxx_Z9	33.1856	-83.8999	0.2462	0.0497	44
413	W29xxx_Z9	33.4568	-83.7288	0.2535	0.0371	50
414	W30xxx_Z9	33.7318	-83.9128	0.3386	0.0498	35
415	W315xx_Z9	34.1779	-83.8531	0.2838	0.0514	38
416	W31xxx_Z9	33.9722	-83.7385	0.1823	0.038	43

Table S1. Station averaged Δt^* measurements. (cont.)

S. No.	Station Name	Latitude	Longitude	Δt^*	Std. dev. Δt^*	No. of Events
417	W32xxx_Z9	34.4657	-83.8658	0.2429	0.0452	36
418	W33xxx_Z9	34.6547	-83.886	0.1246	0.04	54
419	W34xxx_Z9	34.8376	-83.9204	0.1926	0.0423	28
420	W35xxx_Z9	34.9762	-83.9438	0.2994	0.0454	41
421	W44Axx_TA	35.1395	-89.8161	-0.3364	0.0517	22
422	W45Axx_TA	35.1568	-89.186	0.0077	0.0472	36
423	W46Axx_TA	35.1333	-88.3783	0.1373	0.0565	29
424	W47Axx_TA	35.2511	-87.5946	0.1575	0.0457	25
425	W48Axx_TA	35.1386	-86.9333	0.1467	0.0492	28
426	W49Axx_TA	35.1194	-86.2645	0.0958	0.0463	32
427	W50Axx_TA	35.2002	-85.3119	0.2184	0.0597	29
428	W51Axx_TA	35.1606	-84.7599	0.1702	0.043	25
429	W52Axx_TA	35.0935	-83.9277	0.3649	0.0482	26
430	W53Axx_TA	35.1696	-83.163	0.1357	0.0369	28
431	W54Axx_TA	35.0857	-82.1859	0.2098	0.0469	34
432	W56Axx_TA	35.135	-80.5828	0.1055	0.0482	33
433	WB45xx_6E	37.7231	-86.5226	0.1743	0.0433	33
434	WCIxxx_IU	38.2289	-86.2939	-0.0488	0.0239	152
435	WOAKxx_SP	34.6215	-83.0522	0.2489	0.0612	18
436	WVTxxx_IU	36.1297	-87.83	0.1268	0.0224	247

Table S1. Station averaged Δt^* measurements. (cont.)

S. No.	Station Name	Latitude	Longitude	Δt^*	Std. dev. Δt^*	No. of Events
437	X45Axx_TA	34.4241	-89.3931	-0.1132	0.0462	28
438	X46Axx_TA	34.5564	-88.5844	0.0416	0.0622	23
439	X47Axx_TA	34.5178	-87.8571	0.2868	0.061	24
440	X48Axx_TA	34.4517	-87.0452	0.0102	0.0486	43
441	X49Axx_TA	34.5126	-86.326	-0.0041	0.049	32
442	X50Axx_TA	34.4596	-85.6486	0.1178	0.2263	4
443	X50Bxx_TA	34.4611	-85.6499	0.2089	0.0348	29
444	X51Axx_TA	34.5658	-84.8574	0.0067	0.0465	37
445	X52Axx_TA	34.6032	-83.8938	0.2085	0.0436	32
446	X53Axx_TA	34.5031	-83.3013	0.1214	0.0436	40
447	X54Axx_TA	34.5474	-82.3743	0.1523	0.0563	36
448	X55Axx_TA	34.4701	-81.6336	0.1142	0.0582	26
449	X56Axx_TA	34.4923	-81.0319	0.0903	0.0461	35
450	X57Axx_TA	34.4643	-80.094	0.1495	0.0667	33
451	Y45Axx_TA	33.8656	-89.5431	-0.1996	0.0702	24
452	Y46Axx_TA	33.8828	-88.8577	-0.1849	0.0558	33
453	Y47Axx_TA	33.9025	-87.8494	0.0842	0.0409	34
454	Y48Axx_TA	33.9131	-87.1696	0.1499	0.0705	25
455	Y49Axx_TA	33.8577	-86.4119	0.2706	0.0636	22
456	Y50Axx_TA	33.8911	-85.7347	0.5636	0.0767	11

Table S1. Station averaged Δt^* measurements. (cont.)

S. No.	Station Name	Latitude	Longitude	Δt^*	Std. dev. Δt^*	No. of Events
457	Y51Axx_TA	33.8993	-85.064	0.134	0.0442	30
458	Y52Axx_TA	33.864	-84.0626	0.3022	0.046	41
459	Y53Axx_TA	33.8554	-83.5836	0.3048	0.043	33
460	Y54Axx_TA	33.8621	-82.688	-0.0562	0.0567	34
461	Y55Axx_TA	33.9375	-81.8581	0.1077	0.0452	33
462	Y56Axx_TA	33.7922	-81.3047	0.2262	0.05	33
463	Y57Axx_TA	34.017	-80.3915	0.1847	0.061	30
464	Z45Axx_TA	33.3705	-89.6913	-0.4112	0.0718	10
465	Z46Axx_TA	33.1933	-88.9414	-0.1738	0.0586	22
466	Z47Axx_TA	33.199	-88.0696	-0.2479	0.0445	30
467	Z47Bxx_N4	33.1989	-88.0696	-0.1965	0.0305	82
468	Z48Axx_TA	33.3764	-87.5556	-0.039	0.0502	24
469	Z49Axx_TA	33.1942	-86.5311	0.121	0.076	19
470	Z50Axx_TA	33.254	-85.9226	0.1067	0.0471	41
471	Z51Axx_TA	33.3167	-85.1747	0.0212	0.0483	28
472	Z52Axx_TA	33.1893	-84.4176	0.248	0.0488	29
473	Z53Axx_TA	33.2801	-83.5713	0.336	0.0499	30
474	Z54Axx_TA	33.2362	-82.8417	0.1596	0.0452	36
475	Z55Axx_TA	33.2211	-82.1359	0.0934	0.0455	35
476	Z56Axx_TA	33.3253	-81.3687	-0.0173	0.0439	36

Table S1. Station averaged Δt^* measurements. (cont.)

S. No.	Station Name	Latitude	Longitude	Δt^*	Std. dev. Δt^*	No. of Events
477	Z57Axx_TA	33.297	-80.7039	-0.192	0.0518	24

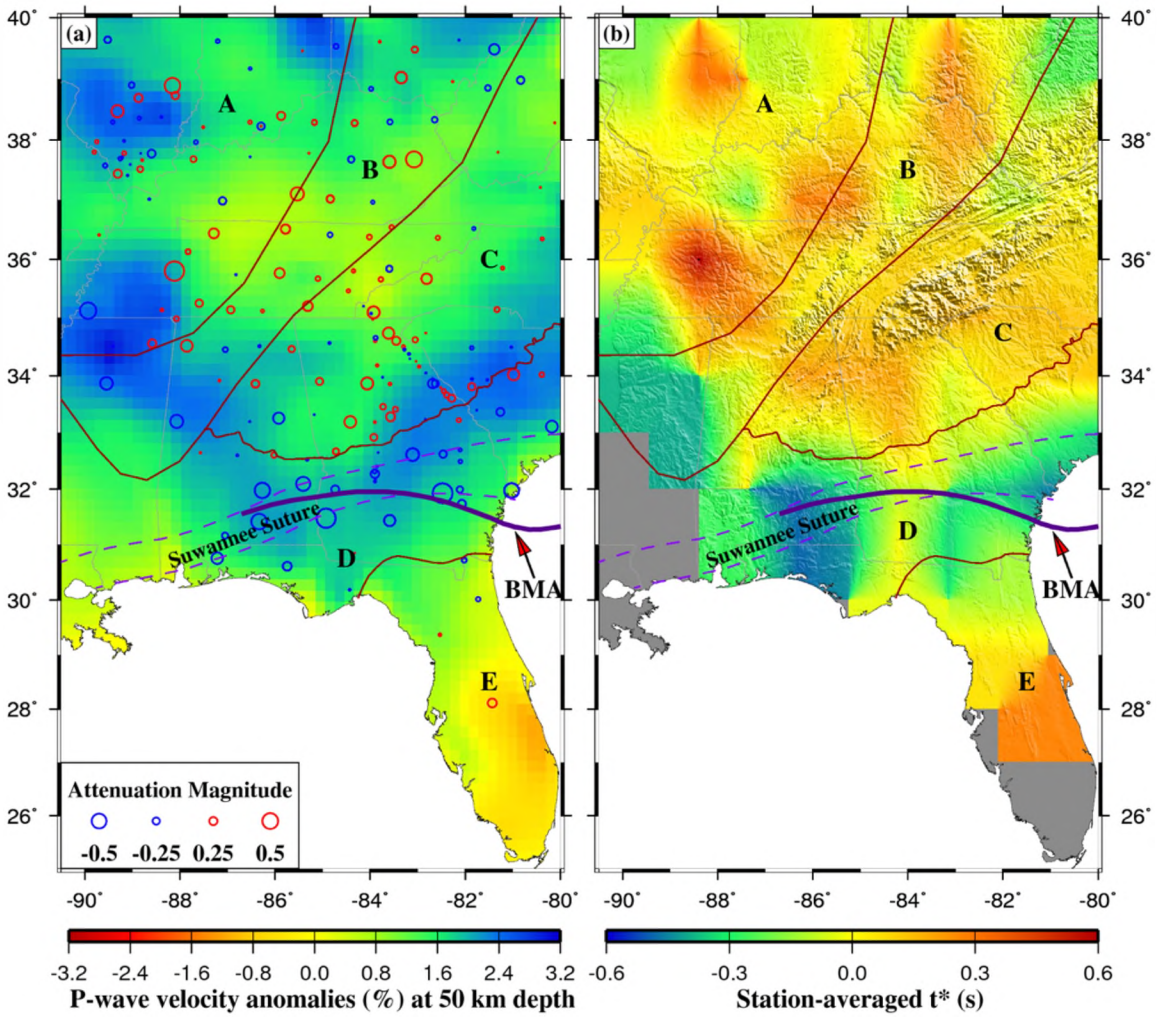

Figure S1: (a) Station-averaged *P*-wave attenuation factors (circles) obtained using only the events with focal depths ≥ 150 km plotted on a background of *P*-wave velocity anomalies at 50 km depth (Golos et al., 2020). Maroon lines represent the boundaries of five regions, divided based on the characteristics of the measurements and the tectonic setting. (b) Spatially averaged *P*-wave attenuation factors in overlapping 1.0° by 1.0° blocks with a moving step of 0.1°.

REFERENCES

Aki, K. (1980). Attenuation of shear-waves in the lithosphere for frequencies from 0.05 to 25 Hz. Physics of the Earth and Planetary Interiors, 21(1), 50–60. https://doi.org/10.1016/0031-9201(80)90019-9

Akinci, A., del Pezzo, E., & Ibáñez, J. M. (1995). Separation of scattering and intrinsic attenuation in southern Spain and western Anatolia (Turkey). Geophysical Journal International, 121(2), 337–353. https://doi.org/10.1111/j.1365-246X.1995.tb05715.x

Anderson, D. L. (1967). The anelasticity of the mantle. Geophysical Journal International, 14(1–4), 135–163. https://doi.org/10.1111/j.1365-246X.1967.tb06232.x

Anderson, D. L., & Minster, J. B. (1979). The frequency dependence of Q in the earth and implications for mantle rheology and chandler wobble, Geophysical Journal of the Royal Astronomical Society, 58, 431-440. https://doi.org/10.1111/j.1365-246X.1979.tb01033.x

Bao, X., Dalton, C. A., Jin, G., Gaherty, J. B., & Shen, Y. (2016). Imaging Rayleigh wave attenuation with USArray. Geophysical Journal International, 206(1), 241–259. https://doi.org/10.1093/gji/ggw151

Baqer, S., & Mitchell, B. J. (1999). Regional Variation of Lg Coda Q in the Continental United States and its Relation to Crustal Structure and Evolution. In B. J. Mitchell & B. Romanowicz (Eds.), Q of the Earth: Global, Regional, and Laboratory Studies (pp. 613–638). Birkhäuser. https://doi.org/10.1007/978-3-0348-8711-3_17

Bensen, G. D., Ritzwoller, M. H., & Shapiro, N. M. (2008). Broadband ambient noise surface wave tomography across the United States. Journal of Geophysical Research: Solid Earth, 113, B05306. https://doi.org/10.1029/2007JB005248.

Biryol, C. B., Wagner, L. S., Fischer, K. M., & Hawman, R. B. (2016). Relationship between observed upper mantle structures and recent tectonic activity across the Southeastern United States. Journal of Geophysical Research: Solid Earth, 121(5), 3393–3414. https://doi.org/10.1002/2015JB012698

Byrnes, J. S., Bezada, M., Long, M. D., & Benoit, M. H. (2019). Thin lithosphere beneath the central Appalachian Mountains: constraints from seismic attenuation beneath the MAGIC array. Earth and Planetary Science Letters, 519, 297–307. https://doi.org/10.1016/j.epsl.2019.04.045

Cafferky, S., & Schmandt, B. (2015). Teleseismic P wave spectra from USArray and implications for upper mantle attenuation and scattering. Geochemistry, Geophysics, Geosystems, 16(10), 3343–3361. https://doi.org/10.1002/2015GC005993

Cook, F. A., Albaugh, D. S., Brown, L. D., Kaufman, S., Oliver, J. E., & Hatcher, R. D. (1979). Thin-skinned tectonics in the crystalline southern Appalachians; COCORP seismic-reflection profiling of the Blue Ridge and Piedmont. Geology, 7(12), 563–567. https://doi.org/10.1130/0091-7613(1979)7<563:TTITCS>2.0.CO;2

Deen, T. J., Griffin, W. L., Begg, G., O'Reilly, S. Y., Natapov, L. M., & Hronsky, J. (2006). Thermal and compositional structure of the subcontinental lithospheric mantle: Derivation from shear wave seismic tomography. Geochemistry, Geophysics, Geosystems, 7(7). https://doi.org/10.1029/2005GC001120

Denison, R. E., Lidiak, E. G., Bickford, M. E., & Kisvarsanyi, E. B. (1984). Geology and geochronology of Precambrian rocks in the Central Interior region of the United States. In Professional Paper (USGS Numbered Series No. 1241– C).

Der, Z. A., & McElfresh, T. W. (1976). Short-period P-wave attenuation along various paths in North America as determined from P-wave spectra of the SALMON nuclear explosion. Bulletin of the Seismological Society of America, 66(5), 1609–1622.

Der, Z. A., & McElfresh, T. W. (1977). The relationship between anelastic attenuation and regional amplitude anomalies of short-period P waves in North America. Bulletin of the Seismological Society of America, 67(5), 1303–1317.

Der, Z. A., McElfresh, T. W., & O'Donnell, A. (1982). An investigation of the regional variations and frequency dependence of anelastic attenuation in the mantle under the United States in the 0.5–4 Hz band. Geophysical Journal International, 69(1), 67–99. https://doi.org/10.1111/j.1365-246X.1982.tb04936.x

Dong, M. T., & Menke, W. H. (2017). Seismic high attenuation region observed beneath southern New England from teleseismic body wave spectra: Evidence for high asthenospheric temperature without melt. Geophysical Research Letters, 44, 10,958-10,969. https://doi.org/10.1002/2017GL074953

Dziewonski, A. M. (1979). Elastic and anelastic structure of the Earth. Reviews of Geophysics, 17(2), 303–312. https://doi.org/10.1029/RG017i002p00303

Dziewonski, A. M., & Anderson, D. L. (1981). Preliminary reference Earth model. Physics of the Earth and Planetary Interiors, 25(4), 297–356. https://doi.org/10.1016/0031-9201(81)90046-7

Eulenfeld, T., & Wegler, U. (2017). Crustal intrinsic and scattering attenuation of high-frequency shear waves in the contiguous United States. Journal of Geophysical Research: Solid Earth, 122, 4676–4690. https://doi.org/10.1002/2017JB014038

Faul, U. H., & Jackson, I. (2005). The seismological signature of temperature and grain size variations in the upper mantle. Earth and Planetary Science Letters, 234(1), 119–134. https://doi.org/10.1016/j.epsl.2005.02.008

Gaite, B., Iglesias, A., Villasenor, A., Herraiz, M., & Pacheco, J. F. (2012). Crustal structure of Mexico and surrounding regions from seismic ambient noise tomography. Geophysical Journal International, 188(3), 1,413-1,424. https://doi.org/10.1111/j.1365-246X.2011.05339.x

Gallegos, A., Ranasinghe, N., Ni, J., & Sandvol, E. (2014). Lg attenuation in the central and eastern United States as revealed by the EarthScope Transportable Array. Earth and Planetary Science Letters, 402, 187–196. https://doi.org/10.1016/j.epsl.2014.01.049

Gao, S. S. (1997). A Bayesian nonlinear inversion of seismic body-wave attenuation factors. Bulletin of the Seismological Society of America, 87(4), 961–970.

Gao, S. S., & Liu, K. H. (2012). AnisDep: A FORTRAN program for the estimation of the depth of anisotropy using spatial coherency of shear-wave splitting parameters. Computers & Geosciences, 49, 330–333. https://doi.org/10.1016/j.cageo.2012.01.020

Gao, S. S., Liu, K. H., & Abdelsalam, M. G. (2010). Seismic anisotropy beneath the Afar Depression and adjacent areas; Implications for mantle flow. Journal of Geophysical Research: Solid Earth, 115, B12330. https://doi.org/10.1029/2009JB007141

Gladwin, M. T., & Stacey, F. D. (1974). Anelastic degradation of acoustic pulses in rock. Physics of the Earth and Planetary Interiors, 8(4), 332–336. https://doi.org/10.1016/0031-9201(74)90041-7

Godey, S., Deschamps, F., Trampert, J., & Snieder, R. (2004). Thermal and compositional anomalies beneath the North American continent. Journal of Geophysical Research: Solid Earth, 109(B1). https://doi.org/10.1029/2002JB002263

Goes, S., Govers, R., & Vacher, P. (2000). Shallow mantle temperatures under Europe from P and S wave tomography. Journal of Geophysical Research: Solid Earth, 105(B5), 11153–11169. https://doi.org/10.1029/1999JB900300

Goes, S., & van der Lee, S. (2002). Thermal structure of the North American uppermost mantle inferred from seismic tomography. Journal of Geophysical Research: Solid Earth, 107(B3), ETG-2-1-ETG 2-13. https://doi.org/10.1029/2000JB000049

Golos, E. M., Fang, H., Yao, H., Zhang, H., Burdick, S., Vernon, F., Schaeffer, A., Lebedev, S., & van der Hilst, R. D. (2018). Shear wave tomography beneath the United States using a joint inversion of surface and body waves. Journal of Geophysical Research: Solid Earth, 123(6), 5169–5189. https://doi.org/10.1029/2017JB014894

Golos, E., Fang, H., & van der Hilst, R. D. (2020). Variations in seismic wave speed and Vp/Vs ratio in the North American lithosphere. Journal of Geophysical Research: Solid Earth, 125, e2020JB020574. https://doi.org/ 10.1029/2020JB020574

Gorich, U., & Muller, G. (1987). Apparent and intrinsic Q: The one-dimensional case. Journal of Geophysics, 61(1), 46–54

Grand, S. P., & Helmberger, D. V. (1984). Upper mantle shear structure of North America. Geophysical Journal International, 76(2), 399–438. https://doi.org/10.1111/j.1365-246X.1984.tb05053.x

Halderman, T. P., & Davis, P. M. (1991). Qp beneath the Rio Grande and East African rift zones. Journal of Geophysical Research, 96(B6). https://doi.org/10.1029/91jb00146

Hatcher, R. D. (2010). The Appalachian orogen: A brief summary. In From Rodinia to Pangea: The Lithotectonic Record of the Appalachian Region. Geological Society of America. https://doi.org/10.1130/2010.1206(01)

Higgins, M. W., & Zietz, I. (1983). Geologic interpretation of geophysical maps of the pre-Cretaceous "basement" beneath the Coastal Plain of the Southeastern United States. In Geological Society of America Memoirs (Vol. 158, pp. 125–130). Geological Society of America.

Hopper, E., & Fischer, K. M. (2018). The changing face of the lithosphere–asthenosphere boundary: Imaging continental scale patterns in upper mantle structure across the contiguous U.S. with Sp converted waves. Geochemistry, Geophysics, Geosystems, 19(8), 2593–2614. https://doi.org/10.1029/2018GC007476

Hwang, Y. K., Ritsema, J., & Goes, S. (2009). Spatial variations of P wave attenuation in the mantle beneath North America. Journal of Geophysical Research: Solid Earth, 114(B6). https://doi.org/10.1029/2008JB006091

Iverson, W. P., & Smithson, S. B. (1983). Reprocessing and reinterpretation of COCORP southern Appalachian profiles. Earth and Planetary Science Letters, 62(1), 75–90. https://doi.org/10.1016/0012-821X(83)90072-9

Jackson, D. D., & Anderson, D. L. (1970). Physical mechanisms of seismic-wave attenuation. Reviews of Geophysics, 8(1), 1–63. https://doi.org/10.1029/RG008i001p00001

Jackson, I., Gerald, J. D. F., Faul, U. H., & Tan, B. H. (2002). Grain-size-sensitive seismic wave attenuation in polycrystalline olivine. Journal of Geophysical Research: Solid Earth, 107(B12), ECV-5-1-ECV 5-16. https://doi.org/10.1029/2001JB001225

Jannsen, D., Voss, J., & Theilen, F. (1985). Comparison of methods to determine Q in shallow marine sediments from vertical reflection seismograms. Geophysical Prospecting, 33(4), 479–497. https://doi.org/10.1111/j.1365-2478.1985.tb00762.x

Karato, S. (1993). Importance of anelasticity in the interpretation of seismic tomography. Geophysical Research Letters, 20(15), 1623–1626. https://doi.org/10.1029/93GL01767

Kennett, B. L. N., & Engdahl, E. R. (1991). Traveltimes for global earthquake location and phase identification. Geophysical Journal International, 105(2), 429–465. https://doi.org/10.1111/j.1365-246X.1991.tb06724.x

Knopoff, L. (1964). Q. Reviews of Geophysics, 2(4), 625–660. https://doi.org/10.1029/RG002i004p00625

Kovach, R. L., & Anderson, D. L. (1964). Attenuation of shear waves in the upper and lower mantle. Bulletin of the Seismological Society of America, 54(6A), 1855–1864.

Lawrence, J. F., Shearer, P. M., & Masters, G. (2006). Mapping attenuation beneath North America using waveform cross-correlation and cluster analysis. Geophysical Research Letters, 33(7), L07315. https://doi.org/10.1029/2006GL025813

Lee, C.-T. A. (2003). Compositional variation of density and seismic velocities in natural peridotites at STP conditions: Implications for seismic imaging of compositional heterogeneities in the upper mantle. Journal of Geophysical Research: Solid Earth, 108(B9). https://doi.org/10.1029/2003JB002413

Liu, K. H., & Gao, S. S. (2011). Estimation of the depth of anisotropy using spatial coherency of shear-wave splitting parameters. Bulletin of the Seismological Society of America, 101(5), 2153–2161. https://doi.org/10.1785/0120100258

Liu, K. H. & Gao, S. S. (2010). Spatial variations of crustal characteristics beneath the Hoggar swell, Algeria, revealed by systematic analyses of receiver functions from a single seismic station. Geochemistry, Geophysics, Geosystems, 11, Q08011. https://doi.org/10.1029/2010GC003091

Liu, L., & Gao, S. S. (2018). Lithospheric layering beneath the contiguous United States constrained by S-to-P receiver functions. Earth and Planetary Science Letters, 495, 79–86. https://doi.org/10.1016/j.epsl.2018.05.012

Marone, F., & Romanowicz, B. (2007). Non-linear crustal corrections in high-resolution regional waveform seismic tomography. Geophysical Journal International, 170(1), 460–467. https://doi.org/10.1111/j.1365-246X.2007.03399.x

McBride, J., & Nelson, K. (1988). Integration of COCORP deep reflection and magnetic anomaly analysis in the southeastern United States: Implications for origin of the Brunswick and East Coast magnetic anomalies. Geological Society of America Bulletin, 100, 436–445. https://doi.org/10.1130/0016-7606(1988)100<0436:IOCDRA>2.3.CO;2

Melbourne, T., & Helmberger, D. (1998). Fine structure of the 410-km discontinuity. Journal of Geophysical Research: Solid Earth, 103(B5), 10091–10102. https://doi.org/10.1029/98JB00164

Menke, W., Skryzalin, P., Levin, V., Harper, T., Darbyshire, F., & Dong, T. (2016). The Northern Appalachian Anomaly; a modern asthenospheric upwelling. Geophysical Research Letters, 43, 10,173-10,179. https://doi.org/10.1002/2016GL070918

Mueller, P. A., Heatherington, A. L., Foster, D. A., Thomas, W. A., & Wooden, J. L. (2014). The Suwannee suture: Significance for Gondwana-Laurentia terrane transfer and formation of Pangaea. Gondwana Research, 26(1), 365–373. https://doi.org/10.1016/j.gr.2013.06.018

Parker, Jr., E. H. (2014). Crustal magnetism, tectonic inheritance, and continental rifting in the southeastern United States. GSA Today, 24(4), 4–9. https://doi.org/10.1130/GSAT-G192A.1

Pasyanos, M E. (2013). A lithospheric attenuation model of North America. Bulletin of the Seismological Society of America, 103(6), 3321–3333. https://doi.org/10.1785/0120130122

Raikes, S. A., & White, R. E. (1984). Measurements of Earth attenuation from downhole and surface seismic recordings. Geophysical Prospecting, 32(5), 892–919. https://doi.org/10.1111/j.1365-2478.1984.tb00745.x

Rankin, D. W., Dillon, W. P., Black, D. F. B., Boyer, S. E., Daniels, D. L., Goldsmith, R., Grow, J. A., Horton, J. W., Hutchinson, D. R., Klitgord, K. D., McDowell, R. C., Milton, D. J., Owens, J. P., Phillips, J. D., Bayer, K. C., Butler, J. R., Elliott, D. W., & Milici, R. C. (1991). E-4 Central Kentucky to the Carolina Trough. Geological Society of America. https://doi.org/10.1130/DNAG-COT-E-4

Sato, H., Sacks, I. S., & Murase, T. (1989). The use of laboratory velocity data for estimating temperature and partial melt fraction in the low-velocity zone: Comparison with heat flow and electrical conductivity studies. Journal of Geophysical Research: Solid Earth, 94(B5), 5689–5704. https://doi.org/10.1029/JB094iB05p05689

Savage, B., Covellone, B. M., & Shen, Y. (2017). Wave speed structure of the eastern North American margin. Earth and Planetary Science Letters, 459, 394–405. https://doi.org/10.1016/j.epsl.2016.11.028

Schmandt, B., & Lin, F. -C. (2014). P and S wave tomography of the mantle beneath the United States. Geophysical Research Letters, 41, 2014GL061231. https://doi.org/10.1002/2014GL061231

Schulte-Pelkum, V., & Mahan, K. H. (2014). A method for mapping crustal deformation and anisotropy with receiver functions and first results from USArray. Earth and Planetary Science Letters, 402, 221–233. https://doi.org/10.1016/j.epsl.2014.01.050

Schutt, D. L., & Lesher, C. E. (2006). Effects of melt depletion on the density and seismic velocity of garnet and spinel lherzolite. Journal of Geophysical Research: Solid Earth, 111(B5). https://doi.org/10.1029/2003JB002950

Shapiro, N. M., & Ritzwoller, M. H. (2004). Inferring surface heat flux distributions guided by a global seismic model: particular application to Antarctica. Earth and Planetary Science Letters, 223(1), 213–224. https://doi.org/10.1016/j.epsl.2004.04.011

Shapiro, S. A., & Kneib, G. (1993). Seismic attenuation by scattering: Theory and numerical results, Geophysical Journal International, 114. https://doi.org/10.1111/j.1365-246X.1993.tb03925.x

Shen, W., & Ritzwoller, M. H. (2016). Crustal and uppermost mantle structure beneath the United States. Journal of Geophysical Research: Solid Earth, 121(6), 4306–4342. https://doi.org/10.1002/2016JB012887

Sobolev, S., Zeyen, H., Stoll, G., Werling, F., Altherr, R., & Fuchs, K. (1996). Upper mantle temperatures from teleseismic tomography of French Massif Central including effects of composition, mineral reactions, anharmonicity, anelasticity and partial melt. Earth and Planetary Science Letters, 139(1), 147–163. https://doi.org/10.1016/0012-821X(95)00238-8

Solomon, S. C. (1972). Seismic-wave attenuation and partial melting in the upper mantle of North America. Journal of Geophysical Research, 77(8), 1483–1502. https://doi.org/10.1029/JB077i008p01483

Solomon, S. C., & Toksöz, M. N. (1970). Lateral variation of attenuation of P and S waves beneath the United States. Bulletin of the Seismological Society of America, 60(3), 819–838.

Spica, Z., Perton, M., Calo, M., Legrand, D., Cordoba-Montiel, F., & Iglesias, A. (2016). 3-D shear wave velocity model of Mexico and South US: Bridging seismic networks with ambient noise cross-correlations (C1) and correlation of coda of correlations (C3). Geophysical Journal International, 206(3), 1,795-1,813. https://doi.org/10.1093/gji/ggw240

Swaby, A. N., Lucas, M. D., & Ross, R. M. (2016). The teacher-friendly guide to the earth science of the southeastern US, 2nd edition. Paleontological Research Institution, Ithaca, New York, 460 pp.

Swann, D. H. (1968). A summary geologic history of the Illinois Basin, in Geology and Petroleum Production of the Illinois Basin, Illinois Geologic Society, p.3-21.

Taner, M. T., Koehler, F., & Sheriff, R. E. (1979). Complex seismic trace analysis. Geophysics, 44(6), 1041-1063. https://doi.org/10.1190/1.1440994

Teng, T.-L. (1968). Attenuation of body waves and the Q structure of the mantle. Journal of Geophysical Research (1896-1977), 73(6), 2195–2208. https://doi.org/10.1029/JB073i006p02195

Thomas, M. D. (1985). Gravity studies of the Grenville Province: Significance for Precambrian plate collision and the origin of anorthosite. In The Utility of Regional Gravity and Magnetic Anomaly Maps (pp. 109–123). Society of Exploration Geophysicists. https://doi.org/10.1190/1.0931830346.ch10

Thomas, W. A. (2006). Tectonic inheritance at a continental margin. https://doi.org/10.1130/1052-5173(2006)016[4:tiaacm]2.0.co;2

Thomas, W. A. (2011). The Iapetan rifted margin of southern Laurentia. Geosphere, 7(1), 97–120. https://doi.org/10.1130/GES00574.1

van der Lee, S., & Nolet, G. (1997). Upper mantle S velocity structure of North America. Journal of Geophysical Research: Solid Earth, 102(B10), 22815–22838. https://doi.org/10.1029/97JB01168

van der Pluijm, B. A., & Catacosinos, P. A. (1996). Basement and basins of eastern North America. Geological Society of America, Special Paper 308, p. 14. https://doi.org/10.1130/SPE308

van Schmus, W. R., Schneider, D. A., Holm, D. K., Dodson, S., & Nelson, B. K. (2007). New insights into the southern margin of the Archean-Proterozoic boundary in the north-central United States based on U-Pb, Sm-Nd, Ar-Ar geochronology. Precambrian Research, 157, 80-105. https://doi.org/10.1016/j.precamres.2007.02.011

Wang, H., Zhao, D., Huang, Z., & Wang, L. (2019). Tomography, seismotectonics, and mantle dynamics of Central and Eastern United States. Journal of Geophysical Research: Solid Earth, 124(8), 8890–8907. https://doi.org/10.1029/2019JB017478

Wang, Z., Zhao, D., Liu, X., & Li, X. (2017). Seismic attenuation tomography of the source zone of the 2016 Kumamoto earthquake (M 7.3). Journal of Geophysical Research: Solid Earth, 122(4), 2988–3007. https://doi.org/10.1002/2016JB013704

Williams, H., & Hatcher, R. D. (1983). Appalachian suspect terranes. In Geological Society of America Memoirs (Vol. 158, pp. 33–53). Geological Society of America. https://pubs.geoscienceworld.org/books/book/168/chapter/3791953/

Wu, R., & Aki, K. (1985). Scattering characteristics of elastic waves by an elastic heterogeneity. Geophysics, 50(4). https://doi.org/10.1190/1.1441934

II. UPPER MANTLE ATTENUATION STRUCTURE BENEATH THE MALAWI AND LUANGWA RIFT ZONES IN EAST AFRICA

ABSTRACT

The Malawi Rift Zone (MRZ) is an ~800 km long N-S oriented Cenozoic rift which initiated with an onset of volcanism in the Rungwe Volcanic Province (RVP) at its northern terminus. We use *P*-wave amplitude spectra from 203 teleseismic events recorded at 113 SAFARI (Seismic Arrays for African Rift Initiation) and other seismic stations in the vicinity of the MRZ to examine spatial variations of seismic attenuation in the crust and upper mantle beneath the Malawi and Luangwa rift zones of the East African Rift System (EARS). *P*-wave spectral ratios are measured in the frequency range of 0.1 to 0.5 Hz using the spectral ratio method to obtain seismic attenuation parameters (Δt^*). The resulting Δt^* measurements reveal a zone of high attenuation in the north of MRZ and significantly low attenuation along the Irumide belt of Zambia. The contribution of scattering to the observed Δt^* is small, as evidenced by a small ratio (less than 0.22 on average) of amplitude on the transverse and vertical components in the *P*-wave window. The Δt^* measurements are further inverted to image the 3-D crustal and upper mantle attenuation structure to draw inferences on the thermal state of the upper mantle and on the physical properties of the rifting system in the area. Our attenuation tomography results reveal a high attenuation zone beneath the RVP in the shallow upper mantle, which can be associated with the decompression melting in response to continental extension. A prominent low-attenuation anomaly beneath the Luangwa Rift

that traverses the central part of the MRZ possibly advocates the southward subsurface extension of the Bangweulu block.

1. INTRODUCTION

Continental rifting is the manifestation of lithospheric stretching, and understanding the extent of rupture of the continental lithosphere in its early stages of rifting is exceptionally challenging (e.g., Buck, 2016; Yirgu et al., 2006). Extending over ~5000 kilometers, the East African Rift System (EARS) marks an ideal location to study the continental rifting mechanism as it exhibits an entire spectrum of rift development, starting from early-stage rifting in its southernmost segments to seafloor spreading in Afar at its northern terminus (Bridges et al., 2012; Chorowicz, 2005) (Figure 1). The EARS consists of two contrasting rifting branches in terms of the intensity of igneous activity: the magma-rich eastern branch, and the magma-poor western branch (Koptev et al., 2015; 2018 and references therein). Unlike the more mature segments of the EARS such as the Main Ethiopian and Kenyan rifts, the early-stage rifting segments provide crucial insight into weakening mechanisms and rift initiation as they are devoid of post rifting sedimentation, magmatism, and subsequent deformation (Cunningham et al., 2009; Mazur et al., 2015; Peřestý et al., 2017).

Located along the southernmost segment of the western branch of the EARS, the Malawi Rift Zone (MRZ) is an ~800 km long N-S oriented Cenozoic rift which initiated with an onset of volcanism in the Rungwe Volcanic Province (RVP) at its northern terminus (Ebinger et al., 1989; 1993) (Figure 1).

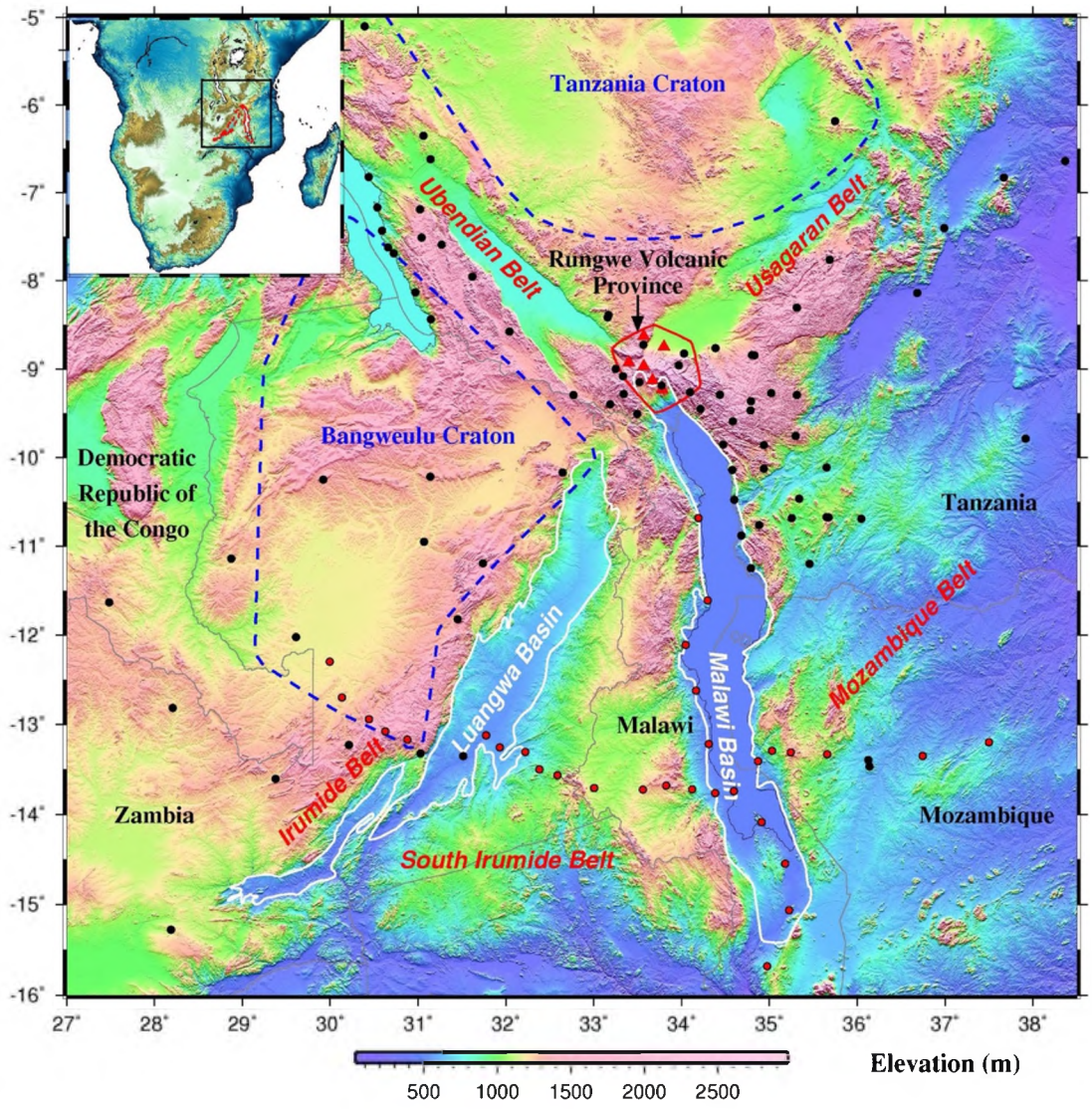

Figure 1. Topographic map of the study area showing locations of seismic stations from SAFARI (red circles) and other seismic arrays (black circles). The red triangles are Holocene volcanoes in the RVP. The Archaean Bangweulu and Tanzania cratons are outlined by blue dashed lines (after Fritz et al., 2013). The inset map of southern and central Africa shows the location of the study area marked by the black rectangle.

The major portion of the weakly extended MRZ is occupied by the ~ 40-60 km wide Lake Malawi (Nyasa), and consists of several half-grabens bounded by border faults (Ebinger, et al., 1989; Specht & Rosendahl, 1989). Extending from the RVP to the

seismically inactive Urema Graben (Mozambique), the MRZ is surrounded by the Tanzania Craton in the north, Bangweulu Craton in the west, and Mozambique Belt in the east (Figure 1). The Paleoproterozoic Ubendian Belt with a crustal thickness of 36-39 km (Last et al., 1997), and the Usagaran Belt having a crustal thickness between 32 and 40 km (Tugume et al., 2012) lie in the southwest and southeast of the Tanzania Craton, respectively (Cahen et al., 1984). Southwest of the Ubendian Belt, between the Kibaran Belt in the north and Irumide Belt to the southeast, is the Bangweulu block which consists of volcanic basement rocks. These basement rocks are overlain by the sedimentary Mporokoso Group, and the central part of the Bangweulu block is overlaid by a recent sedimentary cover that restricts the direct dating of the central basement (Adams et al., 2018). In the south and southeast of the Bangweulu block are the Irumide and South Irumide Belts, respectively. The Irumide Belt is a lithospheric block of uncertain origins that exists between the Bangweulu block and southern Malawi Rift. Although most sources indicate that the Irumide Belt is Proterozoic in age, some studies suggest that it may once have been a stable craton (Abdelsalam et al., 2002; Johnson et al., 2006; Liégeois et al., 2013; Sarafian et al., 2018), and others indicate that it may still contain the central nucleus of unaltered cratonic lithosphere called the Niassa Craton (de Waele et al., 2009; Giacomo, 1984; Sarafian et al., 2018). To the west of the MRZ lies the ~600 km long and ~80 km wide Permo-Triassic Luangwa Rift Zone (LRZ) of Zambia located between the Proterozoic Irumide Belt and Pan-African South Irumide Belt and represents the initial continuation of the EARS into the southwestern branch (Banks et al., 1995; Fritz et al., 2013). In the LRZ, active rifting was initiated in the Early Permian and lasted till the Triassic, and may have recently been reactivated by the same

extensional regional stress that formed the Cenozoic EARS (Banks et al., 1995). This rift valley consists mainly of Permo-Triassic clastic sediments of the Karoo Supergroup that are found up to a depth of 8 km (Banks et al., 1995).

To better understand the evolution and extensional processes of an early-stage rift, numerous seismic studies have been conducted in this area in recent years in the vicinity of the MRZ (Accardo et al., 2017, 2018; Adams et al., 2018; Borrego et al., 2018; Gao et al., 2013; Grijalva et al., 2018; Reed et al., 2016, 2017; Shillington et al., 2016; Sun et al., 2021; Tepp et al., 2018; Wang et al., 2019; Yu et al., 2020). Active rifting models for the EARS (Kampunzu & Lubala, 1991; Yirgu et al., 2006) advocate that upward movement of the asthenosphere is thermally eroding the lithospheric mantle and consequently thinning it. The African Superswell, a NE tilted low-velocity anomaly originating from the lowest mantle beneath southern Africa, extends through the 660-km seismic discontinuity and provides dynamic support in the form of either a single plume or multiple upwellings (Hilton et al., 2011). This upwelling of the convective mantle has caused the increase in topographic elevation, and subsequently, the formation of the Ethiopia and Kenya plateaus (Ebinger et al., 1989; Nyblade et al., 2000; Nyblade & Robinson, 1994; Ritsema, 1999). However, the extent of influence of the African Superswell on the volcanism beneath the RVP, and rift initiation in the MRZ remains a subject of debate. The low-velocity anomalies beneath the RVP, as reported in previous global and regional seismic tomographic studies (Adams et al., 2012; Hansen et al., 2012; Mulibo & Nyblade, 2013; Ritsema, 1999; Zhao, 2001) are explained as upwelling of the asthenospheric mantle caused by the African Superswell (Ritsema, 1999). An isotope geochemistry study (Hilton et al., 2011) reported the helium isotope ratios ($^{3}He/^{4}He$) of

the lavas and tephras of the RVP by analyzing a total of 31 samples. The study found higher-than-normal $^{3}He/^{4}He$ ratios at RVP, which indicate the presence of a high time-integrated $^{3}He/(U+Th)$ ratio in the mantle source region. The lowermost mantle is interpreted as an obvious candidate for such a source, as it is a more primitive, or less degassed portion of the mantle that has remained isolated from the convecting upper mantle (Courtillot et al., 2003; Graham, 2002). The high $^{3}He/^{4}He$ ratios at the RVP, which almost approach the values of $^{3}He/^{4}He$ ratios measured along the Main Ethiopian Rift (Marty et al., 1996; Scarsi & Craig, 1996), provide a shred of evidence for the mantle upwelling that originated from the African Superswell (Hilton et al., 2011).

On the other side of the debate, the low-velocity anomaly beneath the RVP reported in previous regional-scale surface and body wave velocity tomography studies (Accardo et al., 2017; Adams et al., 2012; 2018; Grijalva et al., 2018; Mulibo & Nyblade, 2013; O'Donnell et al., 2013) is mainly confined in the uppermost mantle and is explained by the presence of melt probably induced by decompression associated with continental extension (O'Donnell et al., 2016). A recent study of *P*-wave velocity anisotropic tomography (Yu et al., 2020) conducted using a large number of teleseismic *P*-wave arrival-time data obtained a 3-D distribution of *P*-wave velocity (V_P) in the upper mantle. They reported normal or slightly low-velocity anomalies beneath both Luangwa and Malawi rift zones and a prominent circular low-velocity anomaly beneath the RVP which is confined in the top 200 km of the upper mantle. The extent of seismic anisotropy and the distribution of the mantle flow system are commonly quantified by teleseismic shear-wave splitting (SWS) analysis. The polarization orientation of the fast wave indicates the orientation of the seismic anisotropy which is caused by the lattice-

preferred orientations of anisotropic minerals such as olivine in the upper mantle (Silver, 1996). Previous SWS studies (Bagley & Nyblade, 2013; Tepp et al., 2018; Walker et al., 2004) reported generally NE-SW trending fast orientations of the SWS measurements beneath eastern Africa. An SWS study (Reed et al., 2017) conducted in the Malawi and Luangwa rift zones using data from the Seismic Arrays for African Rift Initiation (SAFARI) experiment (Gao et al., 2013), revealed a mostly asthenospheric origin of the observed azimuthal anisotropy and attributed it to absolute plate motion of the African Plate in the no-net rotation frame. While it is known that the SWS measurements provide an excellent lateral resolution, their vertical resolution is low (Savage, 1999; Silver & Chan, 1991) and they cannot be used effectively for characterizing the vertical distribution of seismic azimuthal anisotropy. The normal mantle transition zone (MTZ) thickness observed in recent receiver function studies (Reed et al., 2016) conducted using SAFARI data indicates the absence of thermal anomalies in the MTZ, which is inconsistent with the hypothesis of large-scale thermal upwelling from the lower mantle that reaches the MTZ.

In this study, we focus on the seismic attenuation structure of the Malawi and Luangwa rift zones to investigate the mantle dynamics associated with early-stage rifting. Seismic attenuation provides significant constraints on the interpretation of the seismic velocity models (Deen et al., 2006; Faul & Jackson, 2005; Godey et al., 2004; Goes et al., 2000; Goes & Lee, 2002; Hwang et al., 2009; Lee, 2003; Schutt & Lesher, 2006; Shapiro & Ritzwoller, 2004; Sobolev et al., 1996), viscosity, rigidity, temperature, and mineral composition of the Earth's crust and mantle (Jackson & Anderson, 1970; Knopoff, 1964). Seismic attenuation exhibits very strong sensitivity to temperature anomalies and the

existence of fluids in the uppermost mantle (Anderson, 1967; Faul & Jackson, 2005; Goes et al., 2000; Jackson et al., 2002; Karato, 1993; 2004; Knopoff, 1964; Sato et al., 1989; Wang et al., 2017), which makes it one of the best indicators of partial melting. Teleseismic body waves provide frequencies intermediate to those of long-period surface waves and regional earthquake body waves, and therefore, are frequently used to study crustal and upper mantle attenuation structures beneath the recording stations (Solomon, 1972; Wang et al., 2017). The conversion of seismic energy to heat, generally caused by grain boundary friction, is called anelastic or intrinsic attenuation (Jackson & Anderson, 1970). The anelastic attenuation of seismic waves in a medium is expressed in terms of the seismic quality factor (Q), which is inversely proportional to anelastic attenuation. The relation between Q and energy dissipation is

$$Q^{-1} = \Delta E / 2\pi E_{max}, \quad (1)$$

where E_{max} is the maximum value of elastic energy stored during one cycle of loading, and ΔE is the energy loss during the cycle (Knopoff, 1964).

Active tectonic areas typically exhibit lower values of seismic quality factor ($Q <$ 200) as compared to stable tectonic regions ($Q >$ 600), while Q varies between 200 and 600 in areas with moderate tectonic activity (Mak et al., 2004). Attenuation studies have been conducted in other major continental rift zones including the Baikal Rift Zone (BRZ) which is located in North Eurasia and is the second-largest Cenozoic continental rift system after the EARS. The BRZ consists of a linear system of uplifts and basins predominantly bordered by normal faults (Logatchev & Florensov, 1978). It is one of the most seismically active rifts in the world, where 13 earthquakes having a magnitude of $Ms \geq 6.0$ have been reported since 1950 by the Baikal Regional Seismological Center of

Geophysical Survey of Siberian Branch of the Russian Academy of Sciences. Dobrynina et al. (2016) investigated the lateral variation of seismic wave attenuation in the BRZ by analyzing coda waves of local earthquakes using a single backscattering model. They reported a strong correlation of the seismic wave attenuation with geological and geophysical characteristics of the BRZ including both seismicity and heat flow. Faulting and active deformation play a crucial role in increasing thermal and fluid flow activity which increases the seismic wave attenuation in the main fault zones of the BRZ by about 25-60% (Dobrynina et al., 2016). Located between the Colorado Plateau in the west and the North American Craton in the east, the Rio Grande rift is another major continental rift that has been investigated using seismic wave attenuation analysis. Halderman and Davis (1991) used teleseismic short-period *P*-waves to measure the Q_P beneath the Rio Grande and EARS by calculating attenuation at each station using a spectral comparison technique. The low Q values, together with the low velocities obtained beneath both the BRZ (Gao et al., 2003) and the Rio Grande rift (Slack et al., 1996) suggest the presence of partial melt in the upwarped asthenosphere. Wang and Zhao (2019) obtained an updated model of 3-D *P*- and *S*- wave attenuation tomography of the Japan subduction zone. In contrast to the continental rifts, the subducting Pacific and Philippines Sea slabs exhibit clear low attenuation with Q values abruptly reaching up to 1800 or higher due to low temperatures (Wang & Zhao, 2019). They also reported high attenuation in the mantle wedge beneath the volcanic front and back-arc areas advocating high sensitivity of seismic attenuation to temperature variations and fluid content (Jackson et al., 2002; 2004; Faul et al., 2004). In this study we investigate the 3-D body-wave attenuation

structure beneath the MRZ and adjacent areas using recently recorded broadband seismic data (Figure 1).

2. DATA AND METHODS

Seismic data used in this study were recorded at a total of 113 three-component broadband seismic stations (Figure 1) among which 35 stations belong to the SAFARI experiment conducted between mid-2012 and mid-2014 (Gao et al., 2013). The stations belonging to the SAFARI experiment (network code XK) were installed along an ~900 km E-W and an ~600 km N-S array located in Malawi, Mozambique, and Zambia. The other 78 stations belong to other seismic experiments, including AF (Africa Array), IU (Global Seismic Network), YH (Africa Array SE Tanzania Basin Experiment), YQ (Study of Extension and maGmatism in Malawi aNd Tanzania (SEGMeNT)), ZP (Africa Array- Uganda/Tanzania), and ZV (Southern Lake Tanganyika experiment). All the data are archived and publicly accessible from the Incorporated Research Institutions for Seismology (IRIS) Data Management Center (DMC). The events recorded at the seismic stations in the area of 27°E – 38.5°E, and 16°S – 5°S, during February 2009 to September 2015 were selected. In order to balance the quantity and quality of the requested data from the IRIS DMC, the cutoff magnitude (M_c) was computed using $M_c = 5.2 + (\Delta\text{-}\Delta_{min})/(180.0–\Delta_{min}) – D/ D_{max}$, where Δ is the epicentral distance in degree, D is the focal depth in km, Δ_{min}=30°, and D_{max}=700 km (Liu & Gao, 2010). We kept the events that were recorded at 10 or more stations. As a result, 203 teleseismic events (Figure 2) were used in this study. The data processing steps include the following:

1) A section of the vertical component seismogram with a total length of 51.2 s (i.e., 1024 data samples) starting from 10 s before the theoretical arrival time of the *P*-wave is selected.
2) A bandpass filter is applied in the frequency range of 0.1 – 0.5 Hz.
3) The instrument response is removed by deconvolving the seismograms with the instrumental response function.
4) A window of seismogram of 10-s duration before the arrival of *P*-wave is used to determine the noise amplitude. The signal-to-noise ratio (SNR) between the maximum absolute value of the signal amplitude and mean absolute noise amplitude is computed for every trace, and seismograms with an SNR smaller than 10.0 are not used for the study.
5) The *P*-wave section of the seismogram is tapered using the customary cosine-sum window, having the form:

$$w(n) = a_0 - (1 - a_0)\cos\frac{2\pi n}{N}, 0 \leq n \leq N, \quad (2)$$

where $w(n)$ is a zero-phase function, N is a positive integer, and the numerical value of a_0 is set as 0.54, which categorizes this tapering function as a Hamming window.

The processed seismic data are used to estimate the seismic body-wave attenuation using a procedure based on the spectral ratio method (e.g., Der & McElfresh, 1976; Hwang et al., 2009; Solomon & Toksöz, 1970; Teng, 1968). It has been recognized that the intrinsic attenuation becomes more dominant at larger epicentral distances, without showing a strong frequency dependence, whereas the energy dissipation of body waves due to scattering is more prominent at shorter distances and decreases substantially as the propagation distance increases (Akinci et al., 1995). Laboratory experiments have

reported frequency-independent Q for many solids up to moderately high frequencies (Knopoff, 1964). Consequently, several studies have discussed the mechanism for intrinsic attenuation that leads to frequency-independent Q (e.g., Dziewonski, 1979; Jackson & Anderson, 1970; Knopoff, 1964), which is assumed in the present study.

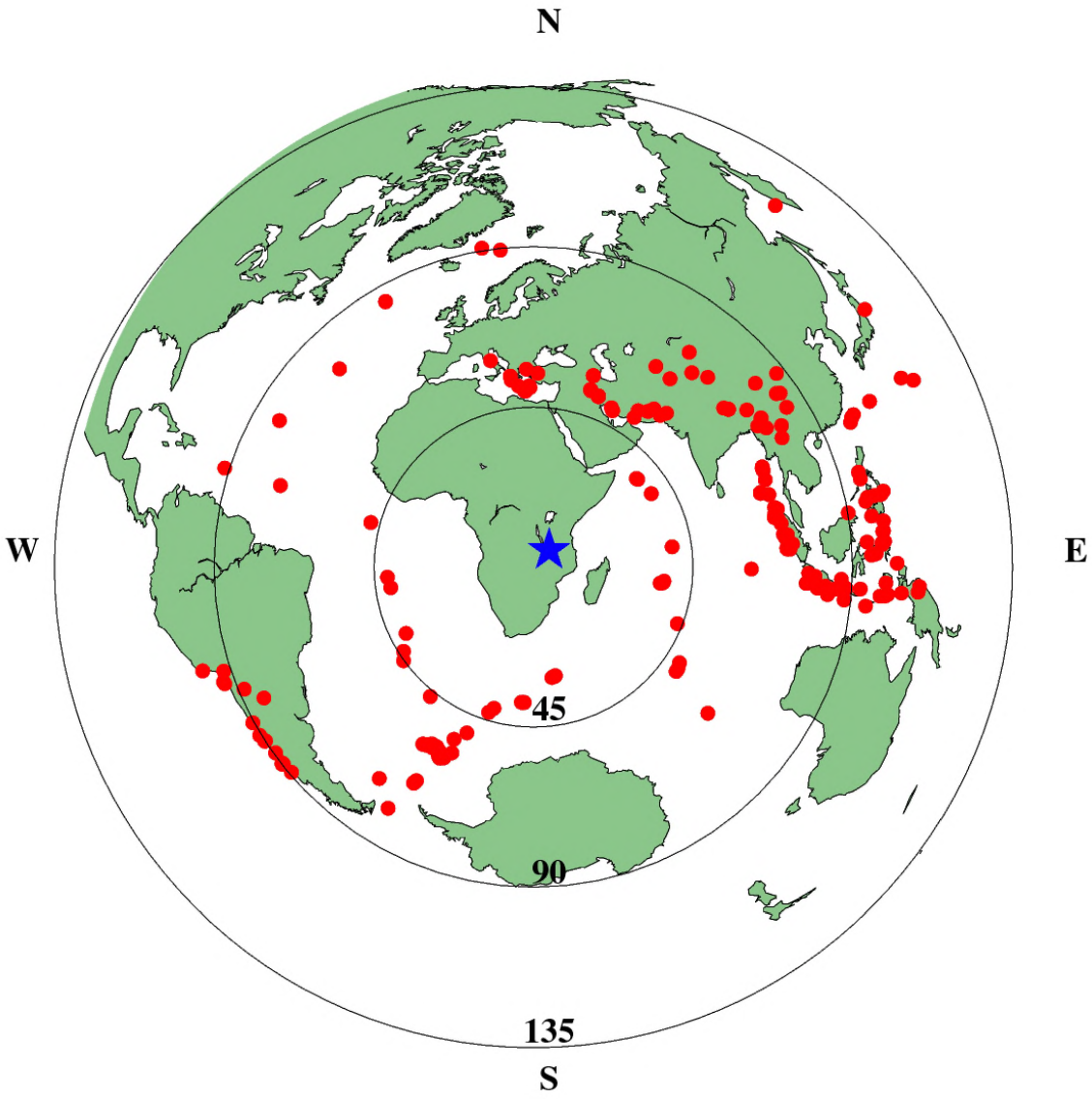

Figure 2. An azimuthal equidistant projection map centered at the study area showing the teleseismic events (red dots) used in this study.

Attenuation is widely considered as the dominant cause of amplitude variations of teleseismic *P*-waves and is measured in terms of the attenuation parameter t*, which is defined as the total traveltime of the wave along the raypath divided by the quality factor (Kovach & Anderson, 1964)

$$\mathbf{t}^{*} = \int_{r} \frac{dt}{Q(r)}, \tag{3}$$

where $Q(r)$ is the quality factor. In the frequency domain, the amplitude spectrum $A_{ik}(f)$ of an event 'k' recorded at station 'i' can be expressed as (Teng, 1968):

$$A_{ik}(f) = S_k(f) G_{ik}(f) R_{ik}(f) I_i(f), \tag{4}$$

where $S_k(f)$ is the source spectrum of the source wavelet $S_k(t)$, $R_{ik}(f)$ is the spectrum of the near-receiver effects, $I_i(f)$, is the spectrum of the instrument response, and $G_{ik}(f)$ is the spectrum of Green's function $G(t)$, which can be written as

$$G_{ik}(f) = e^{-\pi f t^{*}_{ik}(f)}, \tag{5}$$

Fourier transform is used to compute the amplitude spectra of all the filtered high-quality seismograms. For each event, we compute the mean spectrum at every station that recorded this event. We used this mean spectrum as the reference spectrum in the spectral ratio to minimize the effects of heterogeneities outside the study area. Additionally, to exclude seismograms with high noise, the minimum correlation coefficient between each spectrum and the mean spectrum is set to 0.9. The relative attenuation factor Δt^{*}_{ik} between station 'i' and reference spectrum from event 'k' is calculated by fitting the spectral ratio with a straight line using the least-squares method (e.g., Der & McElfresh, 1977; Solomon & Toksöz, 1970); that is,

$$\ln \frac{A_i(f)}{A_k(f)} = \mathrm{C} - \pi \, \Delta t^{*}_{ik} \, f \tag{6}$$

where C is the ratio between the near receiver effects of station 'i' and reference spectrum from event 'k' ($R_{ik}(f)$ in Equation 4), and is assumed to be frequency independent.

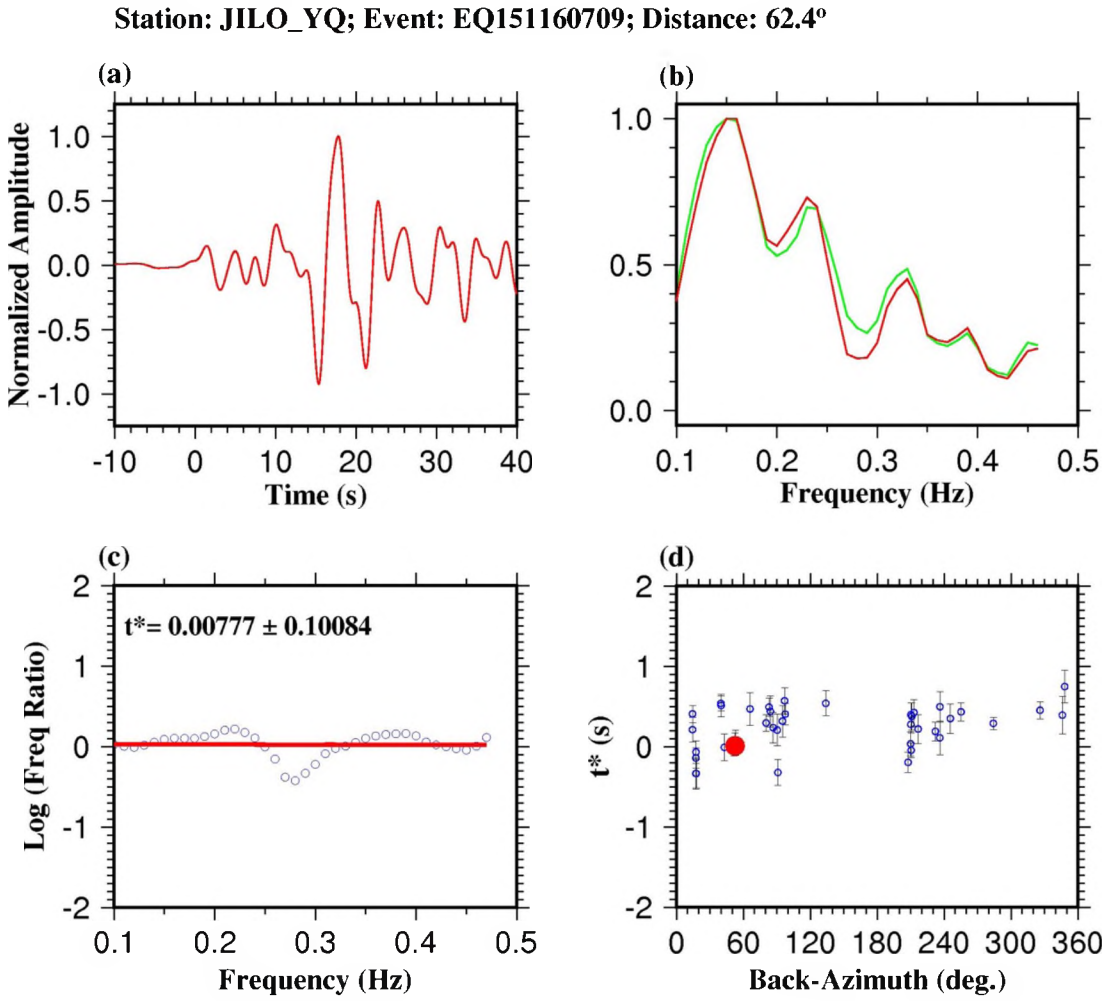

Figure 3. An example of spectral ratio analysis for Station JILO. (a) Normalized *P* waveforms for Station JILO (red) of Network YQ for event 2015-116-07-09 with an epicentral distance of 62.4°. (b) Normalized spectra for the time series shown in (a) (red), and the mean spectrum (green). (c) The spectral ratio between Station JILO and the mean spectrum plotted against frequency. The red line represents the line of best fit. (d) Δt^* measurements for all the events recorded at Station JILO plotted against the back-azimuth of the events. The red dot represents the measurement using data shown in (a).

We manually checked the automatically computed results and the measurements with abnormal data or with a nonlinear frequency variation of the spectral ratios are removed. Furthermore, Δt^*_{ik} measurements with an absolute value greater than 1.0 s, or a standard deviation greater than 0.2 s are excluded. To investigate possible azimuthal variations of the relative Δt^* values, for each of the stations, we plot the resulting Δt^* against the back-azimuth of the event (see Figure 3 for an example).

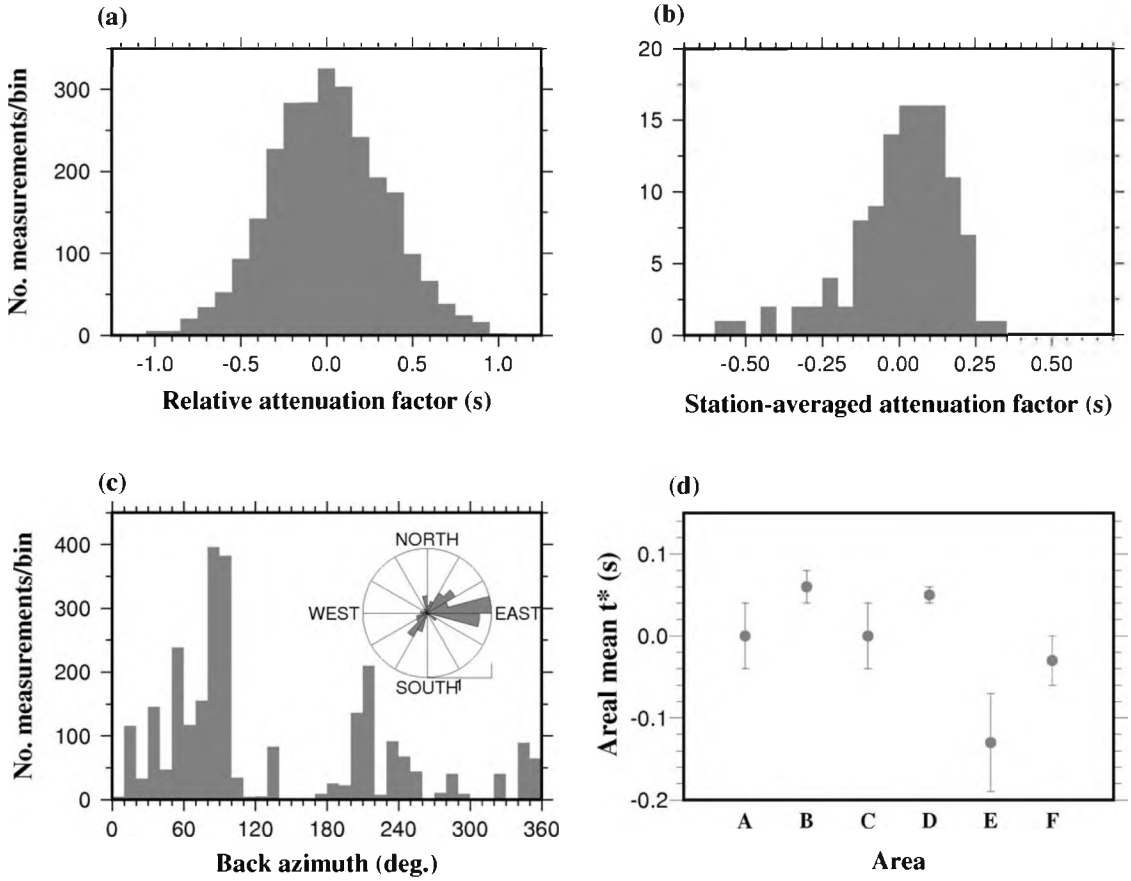

Figure 4. Distribution of (a) Δt^* measurements for all events and (b) station-averaged Δt^* measurements. (c) Azimuthal distribution of the individual measurements. (d) Mean Δt^* values for six areas shown in Figure 5 (b).

3. RESULTS

The resulting 2,626 individual Δt^* measurements (Figure 4a) obtained using the spectral ratio method are used to compute the station-averaged Δt^* measurements (Figures 4b & 5a and Table S1) which vary from -0.55 ± 0.05 s to 0.32 ± 0.11 s in the study area, and demonstrate systematic spatial variations. To analyze the lateral variation of attenuation, station-averaged Δt^* measurements (Figure 5a) are spatially interpolated by averaging the measurements in overlapping 1° radius bins with a moving step of 0.1° (Figure 5b). Based on the tectonic setting and the characteristics of the measurements (Figure 5), we divide the study area into six regions: Ubendian Belt (A), Usagaran Belt (B), Mozambique Belt (C), Malawi Basin (D), South Irumide Belt (E), and Bangweulu Craton and Irumide Belt (F).

3.1. AREA A

Area A is an NW-SE elongated zone of the Palaeoproterozoic Ubendian Belt located along the southwest margin of the Tanzania Craton. It consists mostly of granulite and amphibolite facies gneisses and metasedimentary rocks that formed during two orogenic events between 2.03 and 1.86 Ga, resulting in granitoid intrusions and denudation of granulities and eclogites (Cahen et al., 1984; Lenoir et al., 1994; Schlüter & Hampton, 1997). In this area, the Δt^* measurements recorded at 15 stations from networks ZP and ZV have an areal mean of 0.00 ± 0.04 s, and show a sharp contrast between the NW and SE regions of the area, exhibiting medium-to-high attenuation with

a mean value of 0.13 ± 0.03 s for the former, and low attenuation with a mean value of -0.05 ± 0.04 s for the latter region.

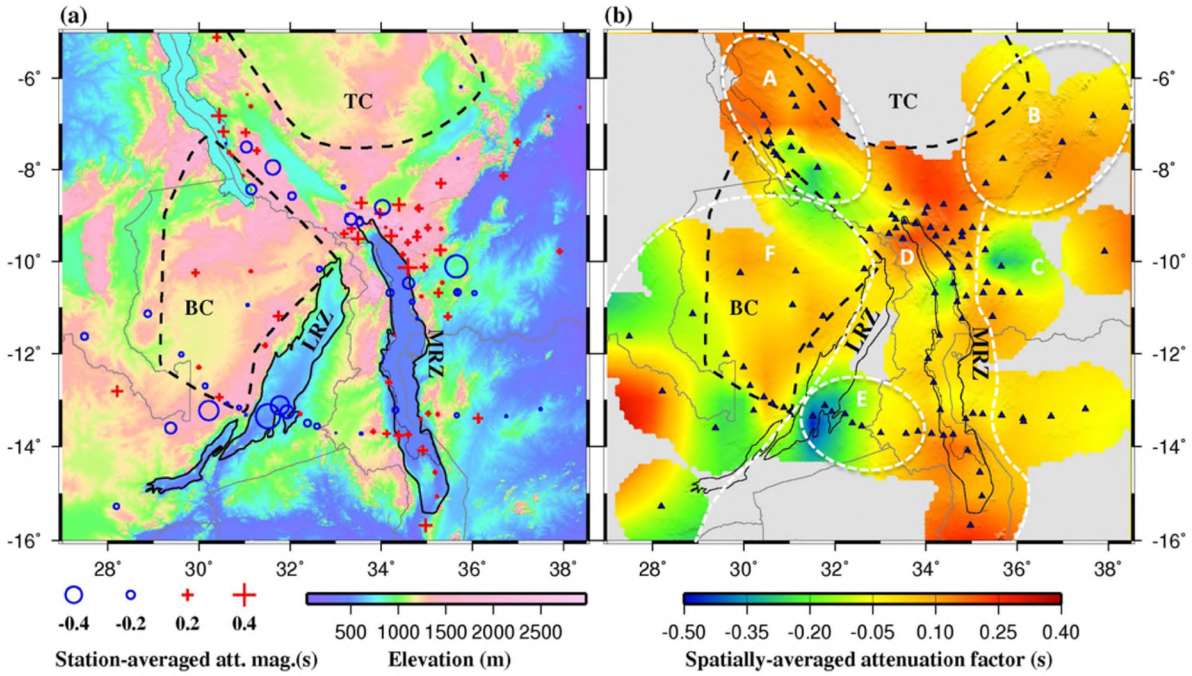

Figure 5. (a) Station-averaged *P*-wave attenuation factors (red pluses and blue circles) plotted at the stations. (b) Lateral variation of spatially-averaged *P*-wave attenuation factors.

3.2. AREA B

Area B is part of the Palaeoproterozoic Usagaran Belt, which is one of many Proterozoic mobile belts surrounding the Tanzania Craton. Located along the southeast margin of the Tanzania Craton, the 1.92- to 1.83-Ga Usagaran Belt consists of predominantly supracrustal rocks metamorphosed to granulite facies and granitoid that were partially derived from reworking and recycling of the Tanzania Craton (Cahen et al., 1984; de Waele et al., 2008; Schlüter & Hampton, 1997). Relatively higher

attenuation is observed in the southwestern part of the area and it gradually decreases towards the east. The Δt^* measurements recorded at the 7 stations in this area have a mean value of 0.06 ± 0.02 s.

3.3. AREA C

Tectonically, area C mainly includes the Neoproterozoic Mozambique Belt which is a part of the East African Orogen extending from the Arabian Nubian Shield in the north to as far south as Antarctica (Cutten & Johnson, 2006). Formed as a result of multiple collisional events between 1200 and 450 Ma (Cahen et al., 1984; Fritz et al., 2013), the Mozambique Belt is comprised of gneisses and granulities. The overall mean of the Δt^* measurements recorded at 16 stations in this area is close to zero (0.00 ± 0.04 s). The key feature of this area is the SW-NE trending low attenuation anomaly that extends from the South Irumide Belt (Area E) in the west to the Mozambique Belt in the east across the Malawi Basin. The southern portion of this area exhibits medium attenuation with no apparent attenuation anomaly.

3.4. AREA D

Area D is mainly comprised of the N-S-oriented MRZ. The northern region of this area constitutes the Nubia-Rovuma-Victoria (NRV) Triple Junction where the boundaries of the microplates namely Victoria Plate in the north and Rovuma Plate in the east meet with the Nubian Plate in the west. In the vicinity of the NRV Triple Junction lie the Holocene volcanoes in the RVP near the northern terminus of the MRZ. The overall mean of the Δt^* measurements recorded at 46 stations in this area is 0.05 ± 0.01 s. High

attenuation anomalies are observed in the RVP near the northern tip and at the southern tip of the MRZ, which is consistent with the low-velocity anomalies reported in recent studies of body-wave and surface-wave tomography (Accardo et al., 2017; Adams et al., 2018; Grijalva et al., 2018; O'Donnell et al., 2013; Yu et al., 2020). The central part of the MRZ exhibit low to medium attenuation which is an extension of the low-attenuation anomaly observed in the Mozambique Belt (northwest part of Area C).

3.5. AREA E

Area E is located between the Luangwa and Malawi basins in the South Irumide Belt. Sandwiched between the Congo and Zimbabwe cratons, the ENE-WSW trending South Irumide Belt consists of late Mesoproterozoic and Neoproterozoic metasedimentary and metaigneous rocks (Johnson et al., 2006). This area displays low attenuation anomalies and the mean of the Δt^* measurements recorded by an E-W trending array of 10 stations is -0.13 ± 0.06 s. The significantly decreased Δt^* values in this area show a sharp contrast with its surrounding areas D and F (Figure 4d).

3.6. AREA F

Area F comprises the Archean Bangweulu Craton in the northern and central parts and the Irumide Belt in the south. The Irumide Belt consists of reworked Archean and Paleoproterozoic crust overlain by ~2 Ga rhyolites and sediments (Begg et al., 2009). This area comprises different physiographic provinces, resulting in a medium-to-high attenuation beneath the Bangweulu Craton and low-to-medium attenuation along the Irumide Belt. The mean of the Δt^* measurements recorded at 19 stations in this area is

-0.03 ± 0.03 s. A sharp decrease in Δt* values at the northern and eastern boundary of area F demonstrates the contrast in attenuation magnitude for different tectonic provinces.

We next analyze the contribution to the observed Δt* by scattering that can also lead to the decay of the teleseismic *P*-wave amplitude because of the heterogeneity of the Earth's crust and mantle (Shapiro & Kneib, 1993). To examine the strength of scattering we estimated the ratio between the mean absolute amplitude of the transverse and the vertical components for all the events used to calculate the Δt*. In an isotropic medium that is free of any heterogeneities, there would be no *P*-wave energy on the transverse component. Therefore, most of the energy in the *P*-wave window on the transverse component can be attributed to the scattered energy due to 3-D heterogeneity. A signal window spanning 5 s before and 10 s after, and a noise window in the range of 5-15 s before, the theoretical *P*-wave arrival time for both the vertical and transverse components are selected. A bandpass filter with corner frequencies of 0.1 Hz and 0.5 Hz is used, which is identical to the one used in Δt* calculation. The ratio of the noise-normalized absolute mean amplitude between the transverse and vertical components is calculated for each of the event-station pairs using

$$Rtz = \frac{Ts / Tn}{Zs / Zn} \tag{7}$$

where Z_s and T_s are the mean total absolute vertical and transverse amplitudes, respectively, and, Z_n and T_n are mean absolute vertical and transverse noise amplitudes, respectively. The station-averaged *Rtz* measurements (Figure 6) range from 0.130 to 0.347 in the study area. The mean *Rtz* value of 0.210 ± 0.003 for all the stations suggests that on average, the contribution of scattering is small in comparison to the anelastic attenuation to the observed total Δt* values. Most of the study area is dominated by low-

to-medium *Rtz* values, with relatively high *Rtz* values observed near the northern tip of the LRZ and the southernmost part of the MRZ. High *Rtz* values obtained at the southern tip of MRZ, an area characterized by high Δt* values suggest that high power and incoherent signals are recorded on the transverse component, or an apparent loss of *P*-wave energy from the vertical component due to scattering, or a combination of both. The *Rtz* values provide an insight into the elastic scattering contributions to the reduction of seismic amplitudes and revealing intrinsic attenuation as the primary cause of the amplitude reduction.

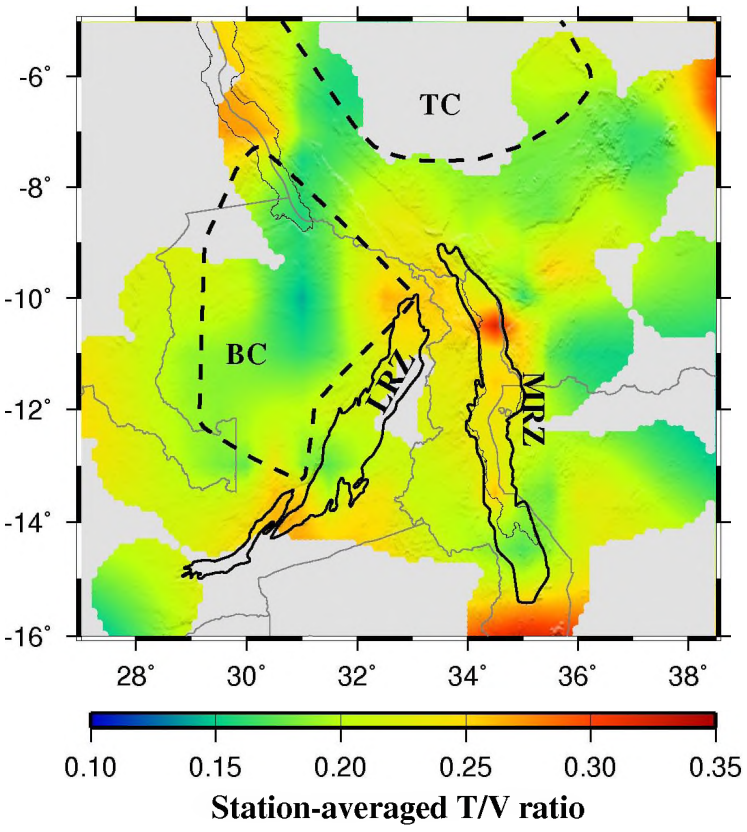

Figure 6. Station-averaged transverse/vertical amplitude ratios

4. DISCUSSION

4.1. ATTENUATION TOMOGRAPHY

4.1.1. Tomographic Inversion. We estimate the 3-D attenuation structure of the upper mantle beneath the study area by inverting the seismic attenuation parameters obtained from the spectral ratio method. The ray-tracing technique proposed by Zhao et al. (1992) is employed to calculate the raypaths using the IASP91 Earth model as the starting one-dimensional velocity model.

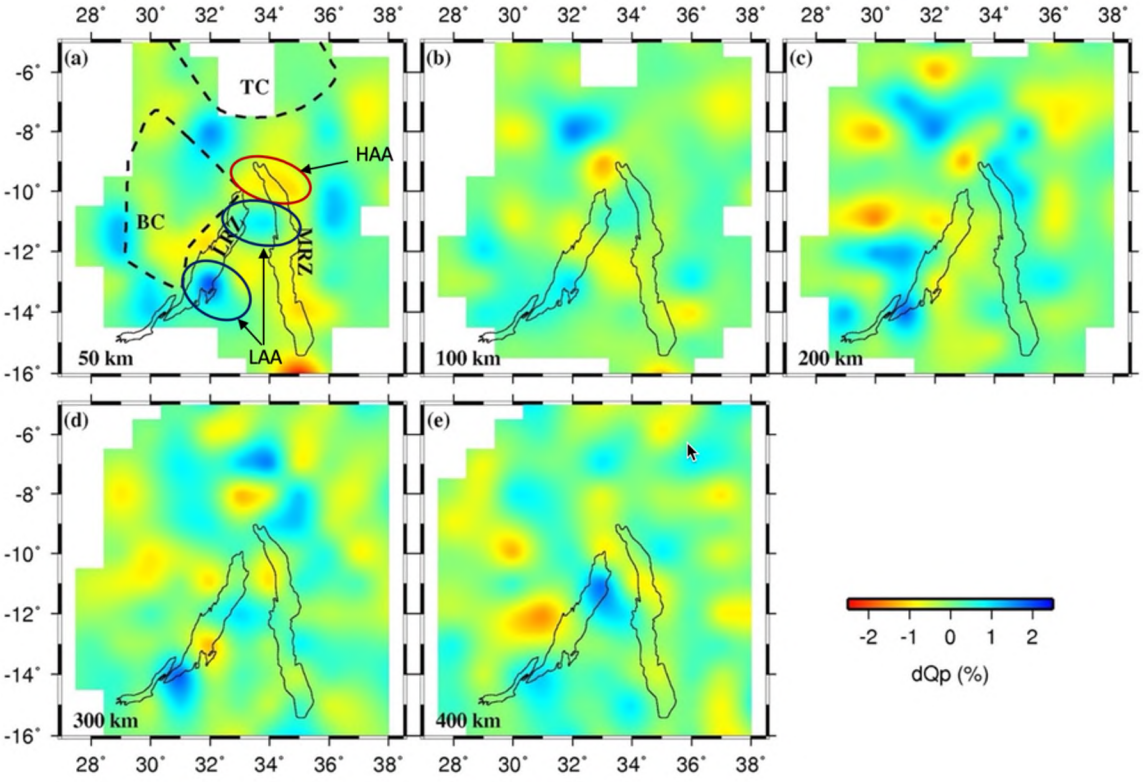

Figure 7. Attenuation tomography results at different depths (50 – 400 km). Red and blue colors denote high and low attenuations, respectively, whose scale is shown below (c). The Malawi (MRZ) and Luangwa (LRZ) Rift Zones are outlined by solid black lines. High (HAA) and low (LAA) attenuation anomalies are marked by red and blue ellipses respectively.

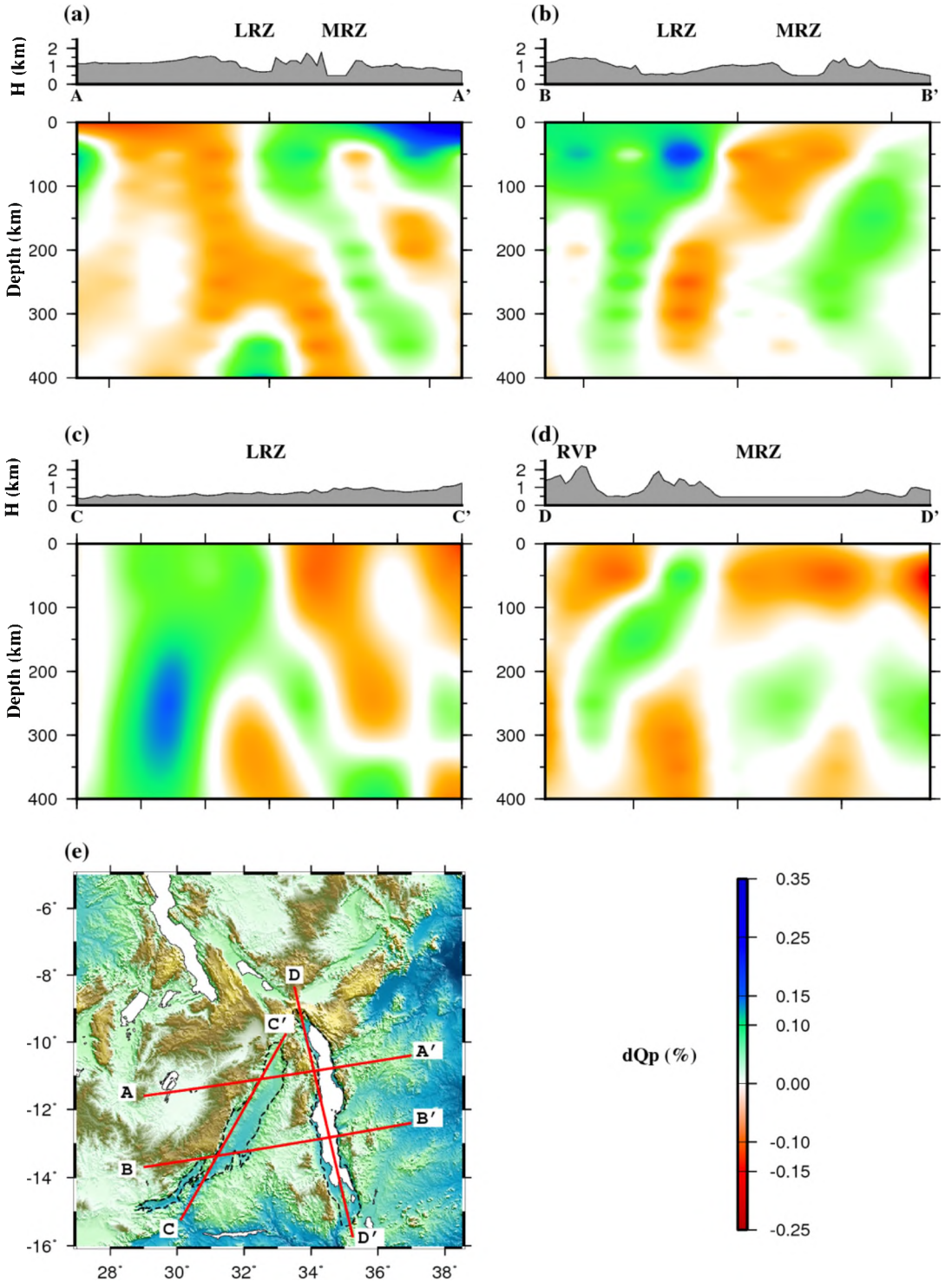

Figure 8. (a)-(d) Vertical cross-sections of Q_P anomalies along the four profiles shown on the inset map (e). LRZ- Luangwa Rift Zone; MRZ-Malawi Rift Zone; RVP-Rungwe Volcanic Province.

The medium under the study area is divided into different layers containing three-dimensional grid nodes with a lateral grid interval of 1°. The vertical spacing between the layers is 50 km at depths of 0-100 km, and 100 km at depths of 100-400 km. The nonlinear tomographic inversion (Zhao et al., 1992) of 1876 Δt* measurements is done by iteratively conducting linear inversions to obtain the 3-D VQ variations

$$\mathbf{t}^* = \int_r \frac{\mathbf{1}}{\boldsymbol{V(r)Q(r)}} \boldsymbol{ds}, \tag{8}$$

where $V(r)$ is the velocity of the waves. The value of the parameter VQ at any point in the study volume is obtained by linear interpolation of VQ values at eight grid nodes surrounding that point. The 3-D ΔQ_P model is obtained by dividing the VQ value with the P-wave velocity (Lu et al., 2019) at each grid node. The resulting ΔQ_P values at grid nodes with a ray hit-count > 3 are mapped (Figure 7) at depths of 50-400 km. Vertical cross-sections of Q_P anomalies along four profiles; two across (Figures 8a & 8b), and two along (Figures 8c & 8d) the rifts are plotted. The Q_P tomographic model reveals high-attenuation anomalies (HAAs) at the northern and southern tips of the MRZ (Figures 7 & 8d), and an elongated NE-SW strip of low-attenuation anomaly (LAA) traversing central MRZ (Figures 7, 8a, 8b, & 8c). A prominent HAA exists beneath the RVP at the northern terminus of the rift in the shallow upper mantle (i.e., down to 300 km depth), which is consistent with the low-velocity anomalies reported in the recent studies of body-wave and surface-wave tomography (Accardo et al., 2017; Grijalva et al., 2018; Yu et al., 2020). The LAAs observed in areas A and D (Figure 5b) extend to the depth of 200 km and 300 km, respectively.

4.1.2. Resolution Test. A checkerboard resolution test (CRT) is conducted to access the reliability of our ΔQ_P tomographic model. The CRT is a reasonable and

convenient method to evaluate the resolving power of tomographic inversion because the CRT does not require the knowledge of the internal operation used in the inversion.

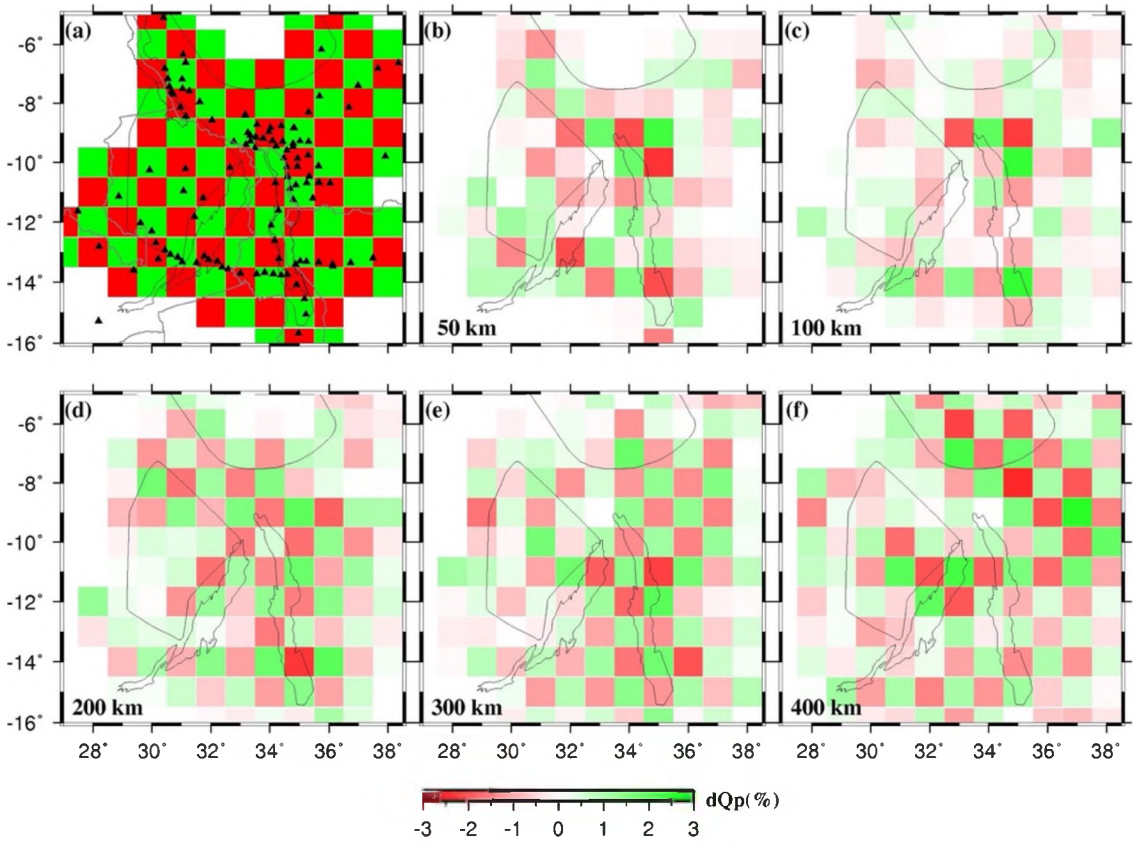

Figure 9. Results of a checkerboard resolution test at different depths with a lateral grid interval of 1° and input Q_P anomalies of ±3%. The green and red squares indicate positive and negative Q_P anomalies, respectively. (a) The input checkerboard model. Black triangles denote seismic stations. (b)-(f) The recovered ΔQ_P at depths of 50, 100, 200, 300, and 400 km, respectively.

The idea is to compute synthetic ΔQ_P for all the events at every station used in the inversion and superimposing a small perturbation signal in a checkerboard pattern. These synthetic ΔQ_P values are then inverted using the same tomographic method. The resolving power of the tomographic inversion is determined by its ability to recover the

perturbed checkerboard model. Following the approach used by Wang et al. (2017) and Yu et al. (2017), perturbed Q_P values of ±3% are assigned alternatively in opposite polarities to the 3-D grid nodes. Thereafter, we added random noise with a standard deviation of 0.1 to the synthetic data and conducted a tomographic inversion to recover the checkerboard pattern. The test result (Figure 9) shows that the checkerboard pattern is reasonably well recovered, and our 3-D Q_P model is robust enough in the upper mantle down 400 km depth beneath the study area. Since the teleseismic rays travel subvertically to the surface, the input anomalies at the shallower depths are not recovered very well beneath the station array. As the depth increases, crisscrossing of the teleseismic rays is gradually improved, leading to a better resolution. In the regions with sparse station coverage, however, the tomographic resolution is low, which is expected.

4.2. COMPARISONS WITH PREVIOUS ATTENUATION AND VELOCITY MODELS

Numerous global 3-D models of upper mantle attenuation have been published using the surface-wave amplitude data (Dalton et al., 2008; Gung & Romanowicz, 2004; Romanowicz, 1995; Selby, 2002), and body-wave data (Bhattacharyya et al., 1996; Hwang et al., 2011; Karaoğlu & Romanowicz, 2018; Reid et al., 2001; Warren & Shearer, 2002). These larger-scale attenuation studies reported a common pattern of higher-than-average attenuation in the vicinity of the EARS and lower-than-average attenuation in the stable continental interiors, such as the cratons of Africa. In a recent study, Karaoğlu and Romanowicz (2018) used a hybrid-full-waveform inversion approach based on the spectral element method to produce a global upper-mantle Q_S model and compared it with the previous global upper-mantle attenuation models (Dalton

et al., 2008; Gung & Romanowicz, 2004) at different depths. At shallower depths (up to 250 km), they reported a good correlation between all three models, with higher attenuation associated with the EARS up to ~100 km and prominent low attenuation beneath the cratons in the depth range of 150-200 km. Below 250 km depth, the correlation becomes unreliable as the attenuation perturbation becomes weaker due to poor depth resolution.

Jemberie and Nyblade (2009) investigated crustal attenuation using 1 Hz *Lg* coda waves and the energy flux model of Frankel and Wennerberg (1987) to estimate the intrinsic and scattering attenuation across the East African plateau. A fairly uniform, higher-than-average crustal intrinsic attenuation (Q ~300–600) is reported in the Tanzania Craton and its surrounding mobile belts, which is attributed to the fluid-filled fractures in the upper crust formed by the Cenozoic rifting. Another study (Ferdinand, 1998) determined the average crustal attenuation using 0.7-5.0 Hz *Lg* waves in the western branch of the EARS reported low Q values associated with active tectonics and geological structure of the rift system. Venkataraman et al. (2004) estimated the regional variation of sub-lithospheric mantle attenuation beneath the Tanzania Craton and the eastern branch of the EARS by measuring *P*-wave spectral amplitude ratios from deep-focus earthquakes. Beneath the rifted lithosphere at 100-400 km depths, a temperature difference of 140-280 K higher than the ambient mantle temperature is reported by combining the V_P perturbations with low Q_P values obtained in this study.

The crustal and upper mantle structure of the MRZ and surrounding regions studied using the surface-wave velocity tomography reported a modest reduction in velocity beneath the Malawi Rift (Accardo et al., 2017; Adams et al., 2018; Borrego et

al., 2018; O'Donnell et al., 2013; Wang et al., 2019). Phase-velocity maps produced using ambient-noise and teleseismic Rayleigh-wave phase velocities revealed slow velocities primarily confined to the Lake Malawi at short periods ($T \leq 12$ s), indicating a thick sedimentary cover (Accardo et al., 2017; Wang et al., 2019), and a prominent low-velocity anomaly beneath the RVP at longer periods ($T > 25$ s) (Accardo et al., 2017). However, the low-velocity anomalies typically found beneath the MRZ do not exist beneath the central portion of the rift (Accardo et al., 2017; O'Donnell et al., 2013), which is consistent with the medium-attenuation estimated in our study (Area D).

4.3. LITHOSPHERIC STRUCTURE AND IMPLICATIONS FOR EARLY-STAGE RIFTING

The Tanzania Craton, located in the northern part of our study area has a significantly thicker lithosphere with a maximum thickness ranging between 150 and 200 km than the surrounding EARS, as estimated from body wave tomography (Begg et al., 2009; Mulibo & Nyblade, 2013), surface wave tomography (Adams et al., 2012; Fishwick, 2010; O'Donnell et al., 2013; Weeraratne et al., 2003) and receiver function analyses (Hansen et al., 2009; Wölbern et al., 2012). Priestley et al. (2008) reported a gradual thinning of the lithosphere from ~250 km at the southern extent of the Victoria Microplate towards the south across the Rukwa, and the MRZ segments of the EARS. Continental-scale surface wave tomographic studies (Fishwick, 2010; Priestley et al., 2008), and receiver function studies (Reed et al., 2016) using the SAFARI data reveal greater-than-average lithospheric thickness beneath the south-central MRZ as compared to the other rift segments in the eastern and western branches of the EARS. A "tongue-shaped" E-W trending zone of 180-200 km thick lithosphere traversing the Congo and

Kalahari cratons was reported near the southern tip of the MRZ (Fishwick, 2010), which may represent the eastward extension of the cratonic lithosphere. A study by Sarafian et al. (2018) using magnetotelluric and aeromagnetic data found that the lithosphere extends to a depth of 250 km beneath the Bangweulu Block, 150-180 km beneath the north, and 250 km beneath the south Irumide Belt. The zone of prominent LAA found in our study correlates with the fast velocities found beneath the Irumide Belt, extending from the Bangweulu Block across the MRZ, most likely caused by the southward subsurface extension of the Bangweulu Block (Adams et al., 2018) and supports the presence of the proposed Niassa Craton and cratonic materials beneath the Irumide Belt (Sarafian et al., 2018). The LAA extending to a depth of ~300 km suggests an assemblage of Archean cratonic roots, overlain by the younger units. This extension of cratonic assemblage accompanied by the previously existing strong lithosphere is believed to restrict the southward extension of the western branch of the EARS (Adams et al., 2018).

4.4. CAUSES OF HIGH ATTENUATION BENEATH THE RVP

The RVP lies within a complex accommodation zone between the Rukwa and Malawi rifts and the Usangu-Ruaha depression, and acts as the nexus of three rigid blocks including the Nubian plate in the west, Victoria microplate in the north, and Rovuma microplate in the east (Calais et al., 2006). This triple junction is seismically active and includes three stratovolcanoes that have experienced Plinian and basaltic eruptions in the past 10 Ka (Ebinger et al., 1989). The high attenuation of seismic waves in the lithospheric mantle and uppermost asthenosphere beneath the Cenozoic RVP can be associated with the elevated temperatures due to the localized magmatism. The surface

wave tomography maps obtained from an excellent ray coverage constrain the low-velocity anomaly beneath the RVP showing that similar-magnitude low-velocity regions do not extend into the south along the Malawi Rift (Accardo et al., 2017). They reported that these low velocities occur within the lithospheric mantle and potentially uppermost asthenosphere, suggesting that mantle processes control the association of volcanism and localization of magmatism beneath the RVP. Yu et al. (2020) used teleseismic *P*-waves to obtain a 3-D distribution of V_P and reported a prominent circular low-velocity anomaly in the top 200 km beneath the RVP without finding any obvious connections to the lower mantle. They interpreted this low-velocity anomaly as a result of decompression melting in response to lithospheric extension further reporting that this anomaly exhibits negative and positive radial anisotropies in the asthenosphere and lithosphere, respectively. The optimal depths for the center of the layer of azimuthal anisotropy obtained from the spatial coherency of shear-wave splitting parameters (Gao & Liu, 2012; Reed et al., 2017) range between 220 and 265 km, which is approximately the depth of the lithosphere-asthenosphere boundary in this region. Our attenuation tomography results (Figure 7) show that the HAA is noticeably shifted to the SW as the depth increases and diminishes at the depth of ~ 300 km. The results indicate that the HAA is mostly constrained in the upper mantle, and thus is not in agreement with the suggestion that the NE-SW pattern of fast orientations are related to NE-ward mantle flow originating from the African Superswell (Bagley & Nyblade, 2013; Tepp et al., 2018; Walker et al., 2004). Instead, the high attenuation observed beneath the RVP is associated mainly with elevated temperatures and localized weakening of the lithosphere caused by decompression melting associated with lithospheric extension.

5. CONCLUSIONS

In this study, we present the first regional-scale 3-D *P*-wave attenuation model beneath the Malawi and Luangwa rift zones using broadband teleseismic data recorded at a total of 113 stations. The resulting 2,626 Δt^* measurements obtained using the spectral ratio technique reveal high-attenuation anomalies at the northern and southern tips of the MRZ, and an elongated NE-SW strip of low-attenuation anomaly traversing central MRZ. The ratio between the transverse and vertical amplitudes of the *P*-wave indicates that the contribution of scattering to the observed Δt^* is low in comparison to the intrinsic attenuation. The Δt^* measurements are inverted to image the 3-D attenuation structure down to 400 km depth. The tomographic results reveal a high attenuation zone beneath the RVP in the upper mantle (i.e., down to 300 km depth), which can be associated with the decompression melting. The prominent low-attenuation anomaly traversing the central part of the MRZ suggests the presence of a relatively thick cratonic lithosphere, possibly reflecting the southward subsurface extension of the Bangweulu block.

ACKNOWLEDGMENTS

All the data used in this study are publicly available from the Incorporated Research Institutions for Seismology Data Management Center (https://ds.iris.edu/ds/nodes/dmc/data/types/waveform-data/). Station and event information, the measured Δt^* and its standard deviation (SD), and a plot for each of the 2,626 measurements can be found at https://web.mst.edu/~as6g7/2c_MRZ_tst/. We

appreciate Cory Reed, Patrick R. N. Chindandali, Belarmino Massingue, Hassan Mdala, Daniel Mutamina, Shane Ingate, Gift Navilembo, Joseph Kayenta, and Francis Tchilongola for their field assistance of seismic data acquisition in Malawi, Mozambique, and Zambia.

APPENDIX

Table S1. Station averaged Δt^* measurements.

S. No.	Station Name	Latitude	Longitude	Δt^*	Std. dev. Δt^*	No. of Events
1	BAKOxx_YQ	-8.8437	34.8016	0.0754	0.0723	16
2	BANGxx_YQ	-10.1128	35.6506	-0.5085	0.0966	9
3	BUMIxx_YQ	-10.1277	34.9365	0.1376	0.0476	15
4	CHAAxx_ZV	-7.5911	31.2704	0.1195	0.0819	13
5	CHALxx_YH	-6.6403	38.367	0.0176	0.0966	13
6	CHAMxx_ZP	-10.9505	31.0691	-0.0351	0.0534	10
7	CHMLxx_YQ	-8.8261	34.0283	-0.3345	0.0822	24
8	DODTxx_AF	-6.186	35.748	-0.0173	0.0276	79
9	GAWAxx_YQ	-8.7648	34.3864	0.2356	0.0553	29
10	IFAKxx_YH	-8.1397	36.6828	0.129	0.0874	9
11	ILINxx_YQ	-9.0818	33.3327	-0.2554	0.0571	37
12	ILOMxx_YQ	-9.2829	33.3421	0.1519	0.0484	41
13	IRINxx_ZP	-7.762	35.6864	-0.0196	0.0419	24
14	ISOKxx_YQ	-9.509	33.4944	0.2344	0.0779	21

Table S1. Station averaged Δt^* measurements. (cont.)

S. No.	Station Name	Latitude	Longitude	Δt^*	Std. dev. Δt^*	No. of Events
15	ISOKxx_ZP	-10.1708	32.6457	-0.0991	0.074	12
16	ITUMxx_YQ	-9.4005	33.188	0.1314	0.0932	17
17	JILOxx_YQ	-8.7261	33.5663	0.2079	0.0436	37
18	KALAxx_ZV	-8.1337	30.9701	0.028	0.0637	15
19	KARAxx_ZV	-6.8216	30.4394	0.2572	0.1274	12
20	KASAxx_ZV	-8.4383	31.1473	-0.2192	0.0712	17
21	KASMxx_ZP	-10.2174	31.1401	0.0513	0.0707	16
22	KIDExx_YQ	-9.2745	35.0214	0.1096	0.0599	19
23	KIMOxx_YQ	-10.6922	36.0463	-0.0781	0.0667	19
24	KIPAxx_ZV	-7.4322	30.591	-0.0057	0.1561	9
25	KIPExx_YQ	-9.2936	34.4364	0.0294	0.0437	38
26	KISAxx_ZV	-7.1901	31.0231	0.1409	0.0734	16
27	KISHxx_ZP	-12.0219	29.6123	-0.0876	0.0745	15
28	KOLAxx_ZV	-7.1687	30.5375	0.1898	0.1267	8
29	KTWExx_AF	-12.814	28.209	0.1918	0.0894	6
30	KURUxx_YQ	-11.1996	35.4577	0.134	0.07	23
31	LAEAxx_ZV	-8.5768	32.0422	-0.1564	0.0692	25
32	LBBxxx_AF	-11.631	27.485	-0.1484	0.0972	13
33	LIGAxx_YQ	-10.6835	35.2545	0.1544	0.0619	27
34	LOSIxx_YQ	-8.3872	33.1682	-0.066	0.0852	13

Table S1. Station averaged Δt^* measurements. (cont.)

S. No.	Station Name	Latitude	Longitude	Δt^*	Std. dev. Δt^*	No. of Events
35	LOSSxx_ZP	-8.4166	33.1575	0.0225	0.0482	25
36	LSZxxx_IU	-15.2779	28.1882	-0.108	0.0567	49
37	LWNGxx_ZP	-10.2498	29.921	0.1196	0.0789	16
38	MAFIxx_ZP	-8.3057	35.3132	0.1701	0.0526	34
39	MAKAxx_ZP	-8.8465	34.8302	0.1354	0.0785	18
40	MAKExx_YQ	-9.2647	34.0968	0.0326	0.0596	37
41	MANDxx_YQ	-10.4782	34.6005	-0.2474	0.0602	17
42	MANSxx_ZP	-11.14	28.8749	-0.1332	0.0836	18
43	MATAxx_YQ	-8.9593	33.9689	0.171	0.0733	27
44	MBAMxx_YQ	-11.2484	34.7919	-0.0286	0.0828	15
45	MBEYxx_AF	-9.0000	33.2500	-0.0088	0.0435	57
46	MBEYxx_YQ	-8.9996	33.2504	-0.0343	0.042	26
47	MFRIxx_YQ	-9.2944	35.3129	0.048	0.0719	13
48	MGORxx_ZP	-6.8279	37.6696	0.0222	0.0454	29
49	MIKUxx_ZP	-7.4035	36.9902	0.1261	0.0662	21
50	MKILxx_YQ	-10.8807	34.6813	-0.0915	0.0538	17
51	MKUSxx_ZP	-13.6035	29.3791	-0.2392	0.1079	10
52	MPIKxx_ZP	-11.821	31.4517	0.0894	0.0858	12
53	MUDIxx_YQ	-9.8621	34.9373	0.0101	0.0647	23
54	MZUNxx_YQ	-9.1502	33.5213	-0.1596	0.0411	36

Table S1. Station averaged Δt^* measurements. (cont.)

S. No.	Station Name	Latitude	Longitude	Δt^*	Std. dev. Δt^*	No. of Events
55	NAMAxx_ZP	-7.5094	31.0414	-0.2412	0.0468	32
56	NAMAxx_ZV	-7.6236	30.6592	0.0647	0.1169	12
57	NGEAxx_YQ	-10.6754	35.6744	-0.1328	0.0532	23
58	NINAxx_ZV	-7.6889	30.7241	0.0375	0.0906	7
59	NINDxx_YQ	-10.1421	34.5792	0.3262	0.1156	12
60	NJOMxx_ZP	-9.3665	34.7911	0.0639	0.0476	29
61	NKALxx_YQ	-9.1881	33.7736	0.0016	0.0386	37
62	PNDAxx_ZP	-6.3519	31.0613	0.0229	0.0586	28
63	Q01MPx_XK	-13.4078	34.87	0.0467	0.047	34
64	Q02GGx_XK	-13.2923	35.0304	0.0861	0.0746	16
65	Q03LCx_XK	-13.3088	35.2425	0.0596	0.0538	39
66	Q04NMx_XK	-13.3309	35.6584	-0.0809	0.0404	45
67	Q05MJx_XK	-13.3953	36.1257	0.1624	0.0932	5
68	Q05MLx_XK	-13.4671	36.1397	0.0361	0.0755	18
69	Q06MQx_XK	-13.3496	36.7453	-0.0322	0.0469	32
70	Q07MRx_XK	-13.1967	37.4986	-0.0401	0.0562	30
71	SERJxx_ZP	-13.2275	30.215	-0.4412	0.0716	12
72	SHWGxx_ZP	-11.1925	31.7397	0.1661	0.0547	10
73	SITAxx_ZV	-6.6192	31.1427	0.0537	0.0808	22
74	SONGxx_ZP	-10.6738	35.6507	-0.0571	0.0492	28

Table S1. Station averaged Δt^* measurements. (cont.)

S. No.	Station Name	Latitude	Longitude	Δt^*	Std. dev. Δt^*	No. of Events
75	SUMBxx_ZP	-7.9531	31.6195	-0.324	0.0554	22
76	TIRIxx_YQ	-10.7626	34.8831	0.0555	0.0652	17
77	TOLAxx_YQ	-9.5921	34.5841	0.1054	0.0461	20
78	TUNDxx_ZP	-9.2958	32.7712	0.022	0.0505	33
79	UKWAxx_YQ	-9.4539	34.2158	0.223	0.0469	31
80	UNDAxx_YQ	-9.8536	34.4738	0.0914	0.106	14
81	UVZAxx_ZP	-5.1049	30.3934	0.1414	0.1213	15
82	UWEMxx_YQ	-9.4696	34.7859	0.1527	0.1129	15
83	W01PDx_XK	-13.7073	33.0061	-0.0019	0.0468	33
84	W02NBx_XK	-13.724	33.5599	-0.0489	0.0583	35
85	W03BLx_XK	-13.6788	33.8245	0.0849	0.0466	32
86	W04VRx_XK	-13.7212	34.1205	0.1275	0.0693	21
87	W05SLx_XK	-13.7627	34.3834	0.182	0.0629	17
88	W06SBx_XK	-13.7421	34.5959	0.1102	0.071	20
89	W07CRx_XK	-10.6838	34.1931	-0.1439	0.0648	29
90	W08KBx_XK	-11.61	34.2964	0.0351	0.0449	26
91	W09TKx_XK	-12.1085	34.0464	-0.0073	0.0634	21
92	W10LWx_XK	-12.6208	34.1652	0.1047	0.0552	29
93	W11KPx_XK	-13.2166	34.3113	-0.1205	0.0559	22
94	W12MBx_XK	-14.0852	34.9112	0.1697	0.0698	25

Table S1. Station averaged Δt^* measurements. (cont.)

S. No.	Station Name	Latitude	Longitude	Δt^*	Std. dev. Δt^*	No. of Events
95	W13CCx_XK	-14.548	35.1806	0.0679	0.0616	33
96	W14MCx_XK	-15.0626	35.2259	0.0475	0.0498	29
97	W15SSx_XK	-15.6818	34.9747	0.2238	0.0598	27
98	WALExx_YH	-9.7896	37.917	0.0925	0.0915	11
99	WINOxx_YQ	-9.7576	35.3001	0.2024	0.0441	50
100	WINOxx_ZP	-9.7576	35.3001	0.2024	0.0441	50
101	Z01TGx_XK	-12.296	29.9948	0.0658	0.0581	29
102	Z02PPx_XK	-12.6965	30.1358	-0.0964	0.0635	30
103	Z03CKx_XK	-12.939	30.4424	0.1252	0.0482	34
104	Z04NNx_XK	-13.075	30.6276	-0.0344	0.0488	26
105	Z05CSx_XK	-13.1667	30.8784	-0.0739	0.0639	28
106	Z06GLx_XK	-13.3502	31.5149	-0.5551	0.0562	7
107	Z06LWx_XK	-13.3218	31.0287	-0.0261	0.0945	13
108	Z07FWx_XK	-13.1206	31.7754	-0.4253	0.0558	27
109	Z08MFx_XK	-13.2546	31.9314	-0.2928	0.064	31
110	Z09CGx_XK	-13.3058	32.221	0.0536	0.0527	33
111	Z10KWx_XK	-13.4991	32.3828	-0.1443	0.066	25
112	Z11CPx_XK	-13.5636	32.5889	-0.1138	0.0606	26
113	ZINIxx_YQ	-10.4659	35.3383	0.0552	0.0675	22

REFERENCES

Abdelsalam, M. G., Li, J.-P., & Stern, R. J. (2002). The Saharan Metacraton.

Accardo, N. J., Gaherty, J. B., Shillington, D. J., Ebinger, C. J., Nyblade, A. A., Mbogoni, G. J., Chindandali, P. R. N., Ferdinand, R. W., Mulibo, G. D., Kamihanda, G., Keir, D., Scholz, C., Selway, K., O'Donnell, J. P., Tepp, G., Gallacher, R., Mtelela, K., Salima, J., & Mruma, A. (2017). Surface wave imaging of the weakly extended Malawi Rift from ambient-noise and teleseismic Rayleigh waves from onshore and lake-bottom seismometers. Geophysical Journal International, 209 (3), 1892–1905. https://doi.org/10.1093/gji/ggx133

Accardo, N. J., Shillington, D. J., Gaherty, J. B., Scholz, C. A., Nyblade, A. A., Chindandali, P. R. N., Kamihanda, G., McCartney, T., Wood, D., & Wambura Ferdinand, R. (2018). Constraints on Rift Basin Structure and Border Fault Growth in the Northern Malawi Rift From 3-D Seismic Refraction Imaging. Journal of Geophysical Research: Solid Earth, 123 (11), 10,003-10,025. https://doi.org/10.1029/2018JB016504

Adams, A, Miller, J., & Accardo, N. (2018). Relationships between lithospheric structures and rifting in the East African Rift System: A Rayleigh wave tomography study. Geochemistry, Geophysics, Geosystems, 19 (10), 3793–3810. https://doi.org/10.1029/2018GC007750

Adams, A, Nyblade, A., & Weeraratne, D. (2012). Upper mantle shear wave velocity structure beneath the East African plateau: evidence for a deep, plateauwide low velocity anomaly. Geophysical Journal International, 189 (1), 123–142. https://doi.org/10.1111/j.1365-246X.2012.05373.x

Akinci, A., del Pezzo, E., & Ibáñez, J. M. (1995). Separation of scattering and intrinsic attenuation in southern Spain and western Anatolia (Turkey). Geophysical Journal International, 121 (2), 337–353. https://doi.org/10.1111/j.1365-246X.1995.tb05715.x

Anderson, D. L. (1967). The anelasticity of the mantle. Geophysical Journal International, 14 (1–4), 135–163. https://doi.org/10.1111/j.1365-246X.1967.tb06232.x

Bagley, B., & Nyblade, A. A. (2013). Seismic anisotropy in eastern Africa, mantle flow, and the African superplume. Geophysical Research Letters, 40 (8), 1500–1505. https://doi.org/10.1002/grl.50315

Banks, N. L., Bardwell, K. A., & Musiwa, S. (1995). Karoo Rift Basins of the Luangwa Valley, Zambia. Hydrocarbon Habitat in Rift Basins, 285–295.

Begg, G. C., Griffi, W. L., Natapov, L. M., O'reilly, S. Y., Grand, S. P., O'neill, C. J., Hronsky, J. M. A., Djomani, Y. P., Swain, C. J., Deen, T., & Bowden, P. (2009). The lithospheric architecture of Africa: Seismic tomography, mantle petrology, and tectonic evolution. Geosphere, 5 (1), 23–50. https://doi.org/10.1130/GES00179.1

Bhattacharyya, J., Masters, G., & Shearer, P. (1996). Global lateral variations of shear wave attenuation in the upper mantle. Journal of Geophysical Research: Solid Earth, 101 (B10), 22273–22289. https://doi.org/10.1029/96jb01782

Borrego, D., Nyblade, A. A., Accardo, N. J., Gaherty, J. B., Ebinger, C. J., Shillington, D. J., Chindandali, P. R. N., Mbogoni, G., Ferdinand, R. W., Mulibo, G., O'Donnell, J., Kachingwe, M., & Tepp, G. (2018). Crustal structure surrounding the northern Malawi rift and beneath the Rungwe Volcanic Province, East Africa. Geophysical Journal International, 215 (2), 1410–1426. https://doi.org/10.1093/gji/ggy331

Bridges, D. L., Mickus, K., Gao, S. S., Abdelsalam, M. G., & Alemu, A. (2012). Magnetic stripes of a transitional continental rift in Afar. Geology, 40 (3), 203–206. https://doi.org/10.1130/G32697.1

Buck, W. R. (2016). 1. Consequences of asthenospheric variability on continental rifting. In Rheology and Deformation of the Lithosphere at Continental Margins (1–30). Columbia University Press. https://doi.org/10.7312/karn12738-002

Cahen, L., Snelling, N. J., Delhal, J., Vail, J. R., Bonhomme, M., & Ledent, D. (1984). The geochronology and evolution of Africa. Clarendon Press.

Calais, E., Ebinger, C. J., Hartnady, C., & Nocquet, J. M. (2006). Kinematics of the East African Rift from GPS and earthquake slip vector data. Geological Society Special Publication, 259, 9–22. https://doi.org/10.1144/GSL.SP.2006.259.01.03

Chorowicz, J. (2005). The East African rift system. Journal of African Earth Sciences, 43, 379-410. https://doi.org/10.1016/j.jafrearsci.2005.07.019

Courtillot, V., Davaille, A., Besse, J., & Stock, J. (2003). Three distinct types of hotspots in the Earth's mantle. Earth and Planetary Science Letters, 205 (3–4), 295–308. https://doi.org/10.1016/S0012-821X(02)01048-8

Cunningham, D., Davies, S., & McLean, D. (2009). Exhumation of a Cretaceous rift complex within a Late Cenozoic restraining bend, southern Mongolia: Implications for the crustal evolution of the Gobi Altai region. Journal of the Geological Society, 166 (2), 321–333. https://doi.org/10.1144/0016-76492008-082

Cutten, H. N. C., & Johnson, S. P. (2006). Tectonic evolution of the Mozambique Belt, Eastern Africa. 21st Colloquium of African Geology, Maputo, Mozambique, 3–5 July (2006), pp. 33-34. Abstract Volume

Dalton, C. A., Ekström, G., & Dziewoński, A. M. (2008). The global attenuation structure of the upper mantle. Journal of Geophysical Research: Solid Earth, 113 (9), 1–24. https://doi.org/10.1029/2007JB005429

de Waele, B., Fitzsimons, I. C. W., Wingate, M. T. D., Tembo, F., Mapani, B., & Belousova, E. A. (2009). The geochronological framework of the irumide belt: A prolonged crustal history along the margin of the Bangweulu Craton. American Journal of Science, 309 (2), 132–187. https://doi.org/10.2475/02.2009.03

de Waele, B., Johnson, S. P., & Pisarevsky, S. A. (2008). Palaeoproterozoic to Neoproterozoic growth and evolution of the eastern Congo Craton: Its role in the Rodinia puzzle. Precambrian Research, 160, 127–141. https://doi.org/10.1016/j.precamres.2007.04.020

Deen, T. J., Griffin, W. L., Begg, G., O'Reilly, S. Y., Natapov, L. M., & Hronsky, J. (2006). Thermal and compositional structure of the subcontinental lithospheric mantle: Derivation from shear wave seismic tomography. Geochemistry, Geophysics, Geosystems, 7 (7). https://doi.org/10.1029/2005GC001120

Der, Z. A., & McElfresh, T. W. (1976). Short-period P-wave attenuation along various paths in North America as determined from P-wave spectra of the SALMON nuclear explosion. Bulletin of the Seismological Society of America, 66 (5), 1609–1622.

Der, Z. A., & McElfresh, T. W. (1977). The relationship between anelastic attenuation and regional amplitude anomalies of short-period P waves in North America. Bulletin of the Seismological Society of America, 67 (5), 1303–1317.

Dobrynina, A. A., Sankov, V. A., Chechelnitsky, V. V., & Déverchère, J. (2016). Spatial changes of seismic attenuation and multiscale geological heterogeneity in the Baikal rift and surroundings from analysis of coda waves. Tectonophysics, 675, 50–68. https://doi.org/10.1016/j.tecto.2016.03.010

Dziewonski, A. M. (1979). Elastic and anelastic structure of the Earth. Reviews of Geophysics, 17 (2), 303–312. https://doi.org/10.1029/RG017i002p00303

Ebinger, C. J., Bechtel, T. D., Forsyth, D. W., & Bowin, C. O. (1989). Effective elastic plate thickness beneath the East African and Afar plateaus and dynamic compensation of the uplifts. Journal of Geophysical Research, 94 (B3), 2883–2901. https://doi.org/10.1029/JB094iB03p02883

Ebinger, C. J., Deino, A. L., Drake, R. E., & Tesha, A. L. (1989). Chronology of volcanism and rift basin propagation: Rungwe volcanic province, East Africa. Journal of Geophysical Research, 94 (B11). https://doi.org/10.1029/jb094ib11p15785

Ebinger, C. J., Deino, A. L., Tesha, A. L., Becker, T., & Ring, U. (1993). Tectonic controls on rift basin morphology: evolution of the northern Malawi (Nyasa) Rift. Journal of Geophysical Research, 98(B10). https://doi.org/10.1029/93jb01392

Faul, U. H., Gerald, J. D. F., & Jackson, I. (2004). Shear wave attenuation and dispersion in melt-bearing olivine polycrystals: 2. Microstructural interpretation and seismological implications. Journal of Geophysical Research: Solid Earth, 109, B06202. https://doi.org/10.1029/2003JB002407

Faul, U. H., & Jackson, I. (2005). The seismological signature of temperature and grain size variations in the upper mantle. Earth and Planetary Science Letters, 234 (1), 119–134. https://doi.org/10.1016/j.epsl.2005.02.008

Ferdinand, R. W. (1998). Average attentuation of 0.7-5.0 Hz Lg waves and magnitude scale determination for the region bounding the western branch of the East African Rift. Geophysical Journal International, 134 (3), 818–830. https://doi.org/10.1046/j.1365-246X.1998.00616.x

Fishwick, S. (2010). Surface wave tomography: Imaging of the lithosphere-asthenosphere boundary beneath central and southern Africa? Lithos, 120 (1-2), 63-73. https://doi.org/10.1016/j.lithos.2010.05.011

Frankel, A., & Wennerberg, L. (1987). Energy-flux model of seismic coda: separation of scattering and intrinsic attenuation. Bulletin of the Seismological Society of America, 77 (4).

Fritz, H., Abdelsalam, M., Ali, K. A., Bingen, B., Collins, A. S., Fowler, A. R., Ghebreab, W., Hauzenberger, C. A., Johnson, P. R., Kusky, T. M., Macey, P., Muhongo, S., Stern, R. J., & Viola, G. (2013). Orogen styles in the East African Orogen: A review of the Neoproterozoic to Cambrian tectonic evolution. Journal of African Earth Sciences, 86, 65–106. https://doi.org/10.1016/j.jafrearsci.2013.06.004

Gao, S. S., Liu, K. H., Davis, P. M., Slack, P. D., Zorin, Y. A., Mordvinova, V. V., & Kozhevnikov, V. M. (2003). Evidence for small-scale mantle convection in the upper mantle beneath the Baikal Rift Zone. Journal of Geophysical Research: Solid Earth, 108, 2194. https://doi.org/10.1029/2002JB002039

Gao, S. S., & Liu, K. H. (2012). AnisDep: A FORTRAN program for the estimation of the depth of anisotropy using spatial coherency of shear-wave splitting parameters. Computers & Geosciences, 49, 330–333. https://doi.org/10.1016/j.cageo.2012.01.020

Gao, S. S., Liu, K. H., Reed, C. A., Yu, Y., Massinque, B., Mdala, H., Moidaki, M., Mutamina, D., Atekwana, E. A., Ingate, S., & Reusch, A. M. (2013). Seismic Arrays to Study African Rift Initiation. Eos, Transactions American Geophysical Union, 94 (24), 213–214. https://doi.org/10.1002/2013EO240002

Godey, S., Deschamps, F., Trampert, J., & Snieder, R. (2004). Thermal and compositional anomalies beneath the North American continent. Journal of Geophysical Research: Solid Earth, 109 (B1). https://doi.org/10.1029/2002JB002263

Goes, S, Govers, R., & Vacher, P. (2000). Shallow mantle temperatures under Europe from P and S wave tomography. Journal of Geophysical Research: Solid Earth, 105 (B5), 11153–11169. https://doi.org/10.1029/1999JB900300

Goes, Saskia, & Lee, S. van der. (2002). Thermal structure of the North American uppermost mantle inferred from seismic tomography. Journal of Geophysical Research: Solid Earth, 107 (B3). https://doi.org/10.1029/2000JB000049

Graham, D. W. (2002). Noble gas isotope geochemistry of mid-ocean ridge and ocean island basalts: Characterization of mantle source reservoirs. Reviews in Mineralogy and Geochemistry, 47 (1), 247–317. https://doi.org/10.2138/rmg.2002.47.8

Grijalva, A., Nyblade, A. A., Homman, K., Accardo, N. J., Gaherty, J. B., Ebinger, C. J., Shillington, D. J., Chindandali, P. R. N., Mbogoni, G., Ferdinand, R. W., Mulibo, G., O'Donnell, J. P., Kachingwe, M., & Tepp, G. (2018). Seismic evidence for plume- and craton-influenced upper mantle structure beneath the northern Malawi rift and the Rungwe volcanic province, East Africa. Geochemistry, Geophysics, Geosystems, 19 (10), 3980–3994. https://doi.org/10.1029/2018GC007730

Gung, Y., & Romanowicz, B. (2004). Q tomography of the upper mantle using three-component long-period waveforms. Geophysical Journal International, 157 (2), 813–830. https://doi.org/10.1111/j.1365-246X.2004.02265.x

Halderman, T. P., & Davis, P. M. (1991). Qp beneath the Rio Grande and East African Rift Zones. Journal of Geophysical Research: Solid Earth, 96 (B6), 10113–10128. https://doi.org/10.1029/91JB00146

Hansen, S. E., Nyblade, A. A., & Julià, J. (2009). Estimates of crustal and lithospheric thickness in sub-saharan Africa from S-wave receiver functions. South African Journal of Geology, 112 (3–4), 229–240. https://doi.org/10.2113/gssajg.112.3-4.229

Hansen, Samantha E., Nyblade, A. A., & Benoit, M. H. (2012). Mantle structure beneath Africa and Arabia from adaptively parameterized P-wave tomography: Implications for the origin of Cenozoic Afro-Arabian tectonism. Earth and Planetary Science Letters, 319–320, 23–34. https://doi.org/10.1016/j.epsl.2011.12.023

Hilton, D. R., Halldórsson, S. A., Barry, P. H., Fischer, T. P., de Moor, J. M., Ramirez, C. J., Mangasini, F., & Scarsi, P. (2011). Helium isotopes at Rungwe Volcanic Province, Tanzania, and the origin of East African Plateaux. Geophysical Research Letters, 38, L21304. https://doi.org/10.1029/2011GL049589

Hwang, Y. K., Ritsema, J., & Goes, S. (2011). Global variation of body-wave attenuation in the upper mantle from teleseismic P wave and S wave spectra. Geophysical Research Letters, 38 (8). https://doi.org/10.1029/2011GL046812

Hwang, Y. K., Ritsema, J., & Goes, S. (2009). Spatial variations of P wave attenuation in the mantle beneath North America. Journal of Geophysical Research: Solid Earth, 114 (B6). https://doi.org/10.1029/2008JB006091

Jackson, D. D., & Anderson, D. L. (1970). Physical mechanisms of seismic-wave attenuation. Reviews of Geophysics, 8 (1), 1–63. https://doi.org/10.1029/RG008i001p00001

Jackson, I., Faul, U. H., Gerald, J. D. F., & Tan, B. H. (2004). Shear wave attenuation and dispersion in melt-bearing olivine polycrystals: 1. Specimen fabrication and mechanical testing. Journal of Geophysical Research: Solid Earth, 109, B06201. https://doi.org/10.1029/2003JB002407

Jackson, I., Gerald, J. D. F., Faul, U. H., & Tan, B. H. (2002). Grain-size-sensitive seismic wave attenuation in polycrystalline olivine. Journal of Geophysical Research: Solid Earth, 107 (B12). https://doi.org/10.1029/2001JB001225

Jemberie, A. L., & Nyblade, A. A. (2009). Intrinsic and scattering Q near 1 Hz across the East African plateau. Bulletin of the Seismological Society of America, 99 (6), 3516–3524. https://doi.org/10.1785/0120090062

Johnson, S. P., de Waele, B., & Liyungu, K. A. (2006). U-Pb sensitive high-resolution ion microprobe (SHRIMP) zircon geochronology of granitoid rocks in eastern Zambia: Terrane subdivision of the Mesoproterozoic Southern Irumide Belt. Tectonics, 25 (6). https://doi.org/10.1029/2006TC001977

Kampunzu, A. B., & Lubala, R. T. (1991). Magmatism in extensional structural settings. Magmatism in Extensional Structural Settings. Springer Berlin Heidelberg. https://doi.org/10.1007/978-3-642-73966-8

Karaoğlu, H., & Romanowicz, B. (2018). Inferring global upper-mantle shear attenuation structure by waveform tomography using the spectral element method. Geophysical Journal International, 213 (3), 1536–1558. https://doi.org/10.1093/gji/ggy030

Karato, S. (1993). Importance of anelasticity in the interpretation of seismic tomography. Geophysical Research Letters, 20 (15), 1623–1626. https://doi.org/10.1029/93GL01767

Karato, S.-I. (2004). Mapping Water Content in the Upper Mantle. In Inside the Subduction Factory. J. Eiler (Ed.). https://doi.org/10.1029/138GM08

Knopoff, L. (1964). Q. Reviews of Geophysics, 2 (4), 625–660. https://doi.org/10.1029/RG002i004p00625

Koptev, A., Calais, E., Burov, E., Leroy, S., & Gerya, T. (2015). Dual continental rift systems generated by plume-lithosphere interaction. Nature Geoscience, 8 (5), 388–392. https://doi.org/10.1038/ngeo2401

Koptev, A., Cloetingh, S., Gerya, T., Calais, E., & Leroy, S. (2018). Non-uniform splitting of a single mantle plume by double cratonic roots: Insight into the origin of the central and southern East African Rift System. Terra Nova, 30 (2), 125–134. https://doi.org/10.1111/ter.12317

Kovach, R. L., & Anderson, D. L. (1964). Attenuation of shear waves in the upper and lower mantle. Bulletin of the Seismological Society of America, 54 (6A), 1855–1864.

Last, R. J., Nyblade, A. A., Langston, C. A., & Owens, T. J. (1997). Crustal structure of the East African Plateau from receiver functions and Rayleigh wave phase velocities. Journal of Geophysical Research: Solid Earth, 102 (B11), 24469-24483. https://doi.org/10.1029/97JB02156

Lee, C.-T. A. (2003). Compositional variation of density and seismic velocities in natural peridotites at STP conditions: Implications for seismic imaging of compositional heterogeneities in the upper mantle. Journal of Geophysical Research: Solid Earth, 108 (B9). https://doi.org/10.1029/2003JB002413

Lenoir, J. L., Liégeois, J. P., Theunissen, K., & Klerkx, J. (1994). The Palaeoproterozoic Ubendian shear belt in Tanzania: geochronology and structure. Journal of African Earth Sciences, 19 (3), 169–184. https://doi.org/10.1016/0899-5362(94)90059-0

Liégeois, J. P., Abdelsalam, M. G., Ennih, N., & Ouabadi, A. (2013). Metacraton: Nature, genesis and behavior. Gondwana Research 23 (1), 220–237. https://doi.org/10.1016/j.gr.2012.02.016

Liu, K. H., & Gao, S. S. (2010). Spatial variations of crustal characteristics beneath the Hoggar swell, Algeria, revealed by systematic analyses of receiver functions from a single seismic station. Geochemistry, Geophysics, Geosystems, 11 (8). https://doi.org/10.1029/2010GC003091

Logatchev, N. A., & Florensov, N. A. (1978). The Baikal system of rift valleys. Tectonophysics, 45 (1), 1–13. https://doi.org/10.1016/0040-1951(78)90218-4

Lu, C., Grand, S. P., Lai, H., & Garnero, E. J. (2019). TX2019slab: A new P and S tomography model incorporating subducting slabs. Journal of Geophysical Research: Solid Earth, 124 (11), 11549–11567. https://doi.org/10.1029/2019JB017448

Mak, S., Chan, L. S., Chandler, A. M., & Koo, R. C. H. (2004). Coda Q estimates in the Hong Kong region. Journal of Asian Earth Sciences, 24 (1), 127–136. https://doi.org/10.1016/j.jseaes.2003.10.001

Marco Achille Giacomo, A. (1984). Petrochemistry, tectonic evolution and metasomatic mineralisations of Mozambique belt granulites from S Malawi and Tete (Mozambique). Precambrian Research, 25 (1–3), 161–186. https://doi.org/10.1016/0301-9268(84)90031-7

Marty, B., Pik, R., & Gezaheg, Y. (1996). Helium isotopic variations in Ethiopian plume lavas: Nature of magmatic sources and limit on lower mantle contribution. Earth and Planetary Science Letters, 144 (1–2), 223–237. https://doi.org/10.1016/0012-821x(96)00158-6

Mazur, S., Campbell, S., Green, C., & Bouatmani, R. (2015). Extension across the Laptev Sea continental rifts constrained by gravity modeling. Tectonics, 34 (3), 435–448. https://doi.org/10.1002/2014TC003590

Mulibo, G. D., & Nyblade, A. A. (2013). The P and S wave velocity structure of the mantle beneath eastern Africa and the African superplume anomaly. Geochemistry, Geophysics, Geosystems, 14 (8), 2696–2715. https://doi.org/10.1002/ggge.20150

Nyblade, A. A., Owens, T. J., Gurrola, H., Ritsema, J., & Langston, C. A. (2000). Seismic evidence for a deep upper mantle thermal anomaly beneath East Africa. Geology, 28 (7), 599–602. https://doi.org/10.1130/0091-7613(2000)28<599:SEFADU>2.0.CO;2

Nyblade, Andrew A., & Robinson, S. W. (1994). The African Superswell. Geophysical Research Letters, 21 (9), 765–768. https://doi.org/10.1029/94GL00631

O'Donnell, J. P., Adams, A., Nyblade, A. A., Mulibo, G. D., & Tugume, F. (2013). The uppermost mantle shear wave velocity structure of eastern Africa from Rayleigh wave tomography: constraints on rift evolution. Geophysical Journal International, 194 (2), 961–978. https://doi.org/10.1093/gji/ggt135

O'Donnell, J. P., Selway, K., Nyblade, A. A., Brazier, R. A., Tahir, N. el, & Durrheim, R. J. (2016). Thick lithosphere, deep crustal earthquakes and no melt: a triple challenge to understanding extension in the western branch of the East African Rift. Geophysical Journal International, 204 (2), 985–998. https://doi.org/10.1093/GJI

Peřestý, V., Lexa, O., Holder, R., Jeřábek, P., Racek, M., Štípská, P., Schulmann, K., & Hacker, B. (2017). Metamorphic inheritance of Rheic passive margin evolution and its early-Variscan overprint in the Teplá-Barrandian Unit, Bohemian Massif. Journal of Metamorphic Geology, 35 (3), 327–355. https://doi.org/10.1111/jmg.12234

Priestley, K., McKenzie, D., Debayle, E., & Pilidou, S. (2008). The African upper mantle and its relationship to tectonics and surface geology. Geophysical Journal International, 175 (3), 1108–1126. https://doi.org/10.1111/j.1365-246X.2008.03951.x

Reed, C. A., Liu, K. H., Chindandali, P. R. N., Massingue, B., Mdala, H., Mutamina, D., Yu, Y., & Gao, S. S. (2016). Passive rifting of thick lithosphere in the southern East African Rift: Evidence from mantle transition zone discontinuity topography. Journal of Geophysical Research: Solid Earth, 121 (11), 8068–8079. https://doi.org/10.1002/2016JB013131

Reed, C. A., Liu, K. H., Yu, Y., & Gao, S. S. (2017). Seismic anisotropy and mantle dynamics beneath the Malawi Rift Zone, East Africa. Tectonics, 36 (7), 1338–1351. https://doi.org/10.1002/2017TC004519

Reid, F. J. L., Woodhouse, J. H., & van Heijst, H. J. (2001). Upper mantle attenuation and velocity structure from measurements of differential S phases. Geophysical Journal International, 145 (3), 615–630. https://doi.org/10.1046/j.1365-246X.2001.01395.x

Ritsema, J. (1999). Complex shear wave velocity structure imaged beneath Africa and Iceland. Science, 286 (5446), 1925–1928. https://doi.org/10.1126/science.286.5446.1925

Romanowicz, B. (1995). A global tomographic model of shear attenuation in the upper mantle. Journal of Geophysical Research: Solid Earth, 100 (B7), 12375–12394. https://doi.org/10.1029/95JB00957

Sarafian, E., Evans, R. L., Abdelsalam, M. G., Atekwana, E., Elsenbeck, J., Jones, A. G., & Chikambwe, E. (2018). Imaging Precambrian lithospheric structure in Zambia using electromagnetic methods. Gondwana Research, 54, 38–49. https://doi.org/10.1016/j.gr.2017.09.007

Sato, H., Sacks, I. S., & Murase, T. (1989). The use of laboratory velocity data for estimating temperature and partial melt fraction in the low-velocity zone: Comparison with heat flow and electrical conductivity studies. Journal of Geophysical Research: Solid Earth, 94 (B5), 5689–5704. https://doi.org/10.1029/JB094iB05p05689

Savage, M. S. (1999). Seismic anisotropy and mantle deformation: What have we learned from shear wave splitting? Reviews of Geophysics, 37 (1), 65–106. https://doi.org/10.1029/98RG02075

Scarsi, P., & Craig, H. (1996). Helium isotope ratios in Ethiopian Rift basalts. Earth and Planetary Science Letters, 144 (3–4), 505–516. https://doi.org/10.1016/s0012-821x(96)00185-9

Schlüter, T., & Hampton, C. (1997). Geology of East Africa. Borntraeger.

Schutt, D. L., & Lesher, C. E. (2006). Effects of melt depletion on the density and seismic velocity of garnet and spinel lherzolite. Journal of Geophysical Research: Solid Earth, 111 (B5). https://doi.org/10.1029/2003JB002950

Selby, N. D. (2002). The Q structure of the upper mantle: Constraints from Rayleigh wave amplitudes. Journal of Geophysical Research, 107 (B5). https://doi.org/10.1029/2001jb000257

Shapiro, N. M., & Ritzwoller, M. H. (2004). Inferring surface heat flux distributions guided by a global seismic model: particular application to Antarctica. Earth and Planetary Science Letters, 223 (1), 213–224. https://doi.org/10.1016/j.epsl.2004.04.011

Shapiro, S. A., & Kneib, G. (1993). Seismic attenuation by scattering: theory and numerical results. Geophysical Journal International, 114 (2), 373-391. https://doi.org/10.1111/j.1365-246X.1993.tb03925.x

Shillington, D. J., Gaherty, J. B., Ebinger, C. J., Scholz, C. A., Selway, K., Nyblade, A. A., et al. (2016). Acquisition of a unique onshore/offshore geophysical and geochemical dataset in the northern Malawi (Nyasa) rift. Seismological Research Letters, 87 (6), 1406–1416. https://doi.org/10.1785/0220160112

Silver, P. G., & Chan, W. W. (1991). Shear wave splitting and subcontinental mantle deformation. Journal of Geophysical Research, 96 (B10), 16429–16454. https://doi.org/10.1029/91jb00899

Silver, P. G. (1996). Seismic anisotropy beneath the continents: Probing the depths of geology. Annual Review of Earth and Planetary Sciences, 24 (1), 385–432. https://doi.org/10.1146/annurev.earth.24.1.385

Slack, P. D., Davis, P. M., Baldridge, W. S., Olsen, K. H., Glahn, A., Achauer, U., & Spence, W. (1996). The upper mantle structure of the central Rio Grande rift region from teleseismic P and S wave travel time delays and attenuation. Journal of Geophysical Research: Solid Earth, 101 (B7), 16003–16023. https://doi.org/10.1029/96jb00109

Sobolev, S. V., Zeyen, H., Stoll, G., Werling, F., Altherr, R., & Fuchs, K. (1996). Upper mantle temperatures from teleseismic tomography of French Massif Central including effects of composition, mineral reactions, anharmonicity, anelasticity and partial melt. Earth and Planetary Science Letters, 139 (1), 147–163. https://doi.org/10.1016/0012-821X(95)00238-8

Solomon, S. C. (1972). Seismic-wave attenuation and partial melting in the upper mantle of North America. Journal of Geophysical Research (1896-1977), 77(8), 1483–1502. https://doi.org/10.1029/JB077i008p01483

Solomon, S. C., & Toksöz, M. N. (1970). Lateral variation of attenuation pf P and S waves beneath the United States. Bulletin of the Seismological Society of America, 60 (3), 819–838.

Specht, T. D., & Rosendahl, B. R. (1989). Architecture of the Lake Malawi Rift, East Africa. Journal of African Earth Sciences, 8 (2–4), 355–382. https://doi.org/10.1016/S0899-5362(89)80032-6

Sun, M, Gao, S, S., Liu, K. H., Mickus, K., Fu, X., & Yu, Y. (2021). Receiver function investigation of crustal structure in the Malawi and Luangwa rift zones and adjacent areas. Gondwana Research, 89, 168-176. https://doi.org/10.1016/j.gr.2020.08.015

Teng, T.-L. (1968). Attenuation of body waves and the Q structure of the mantle. Journal of Geophysical Research (1896-1977), 73(6), 2195–2208. https://doi.org/10.1029/JB073i006p02195

Tepp, G., Ebinger, C. J., Zal, H., Gallacher, R., Accardo, N., Shillington, D. J., et al. (2018). Seismic Anisotropy of the Upper Mantle Below the Western Rift, East Africa. Journal of Geophysical Research: Solid Earth, 123 (7), 5644–5660. https://doi.org/10.1029/2017JB015409

Tugume, F., Nyblade, A., & Juli, J. (2012). Moho depths and Poisson's ratios of Precambrian crust in East Africa: Evidence for similarities in Archean and Proterozoic crustal structure. Earth and Planetary Science Letters, 355–356, 73–81. https://doi.org/10.1016/j.epsl.2012.08.041

Venkataraman, A., Nyblade, A. A., & Ritsema, J. (2004). Upper mantle Q and thermal structure beneath Tanzania, East Africa from teleseismic P wave spectra. Geophysical Research Letters, 31 (15). https://doi.org/10.1029/2004GL020351

Walker, K. T., Nyblade, A. A., Klemperer, S. L., Bokelmann, G. H. R., & Owens, T. J. (2004). On the relationship between extension and anisotropy: Constraints from shear wave splitting across the East African Plateau. Journal of Geophysical Research: Solid Earth, 109 (B8). https://doi.org/10.1029/2003JB002866

Wang, T., Feng, J., Liu, K. H., & Gao, S. S. (2019). Crustal structure beneath the Malawi and Luangwa Rift Zones and adjacent areas from ambient noise tomography. Gondwana Research, 67, 187–198. https://doi.org/10.1016/j.gr.2018.10.018

Wang, Z., Zhao, D., Liu, X., & Li, X. (2017). Seismic attenuation tomography of the source zone of the 2016 Kumamoto earthquake (M 7.3). Journal of Geophysical Research: Solid Earth, 122 (4), 2988–3007. https://doi.org/10.1002/2016JB013704

Wang, Z., & Zhao, D. (2019). Updated attenuation tomography of Japan subduction zone. Geophysical Journal International, 219, 1679-1697. https://doi.org/10.1093/gji/ggz339

Warren, L. M., & Shearer, P. M. (2002). Mapping lateral variations in upper mantle attenuation by stacking P and PP spectra. Journal of Geophysical Research: Solid Earth, 107 (B12). https://doi.org/10.1029/2001jb001195

Weeraratne, D. S., Forsyth, D. W., Fischer, K. M., & Nyblade, A. A. (2003). Evidence for an upper mantle plume beneath the Tanzanian craton from Rayleigh wave tomography. Journal of Geophysical Research: Solid Earth, 108 (B9). https://doi.org/10.1029/2002jb002273

Wölbern, I., Rümpker, G., Link, K., & Sodoudi, F. (2012). Melt infiltration of the lower lithosphere beneath the Tanzania craton and the Albertine rift inferred from S receiver functions. Geochemistry, Geophysics, Geosystems, 13 (8). https://doi.org/10.1029/2012GC004167

Yirgu, G., Ebinger, C. J., & Maguire, P. K. H. (2006). The Afar volcanic province within the East African Rift System: Introduction. Geological Society Special Publication, 259, 1–6. https://doi.org/10.1144/GSL.SP.2006.259.01.01

Yu, Y., Gao, S. S., Zhao, D., & Liu, K. H. (2020). Mantle structure and flow beneath an early-stage continental rift: Constraints from P-wave anisotropic tomography. Tectonics, 39 (2). https://doi.org/10.1029/2019tc005590

Yu, Y., Liu, K. H., Huang, Z., Zhao, D., Reed, C. A., Moidaki, M., Lei, J., & Gao, S. S. (2017). Mantle structure beneath the incipient Okavango rift zone in southern Africa. Geosphere, 13 (1), 102–111. https://doi.org/10.1130/GES01331.1

Zhao, D. (2001). Seismic structure and origin of hotspots and mantle plumes. Earth and Planetary Science Letters, 192 (3), 251–265. https://doi.org/10.1016/S0012-821X(01)00465-4

Zhao, D., Hasegawa, A., & Horiuchi, S. (1992). Tomographic imaging of P and S wave velocity structure beneath northeastern Japan. Journal of Geophysical Research, 97, 19909-19928. https://doi.org/10.1029/92JB00603

SECTION

2. CONCLUSIONS

We estimated the crustal and upper mantle attenuation structure beneath the southeastern United States (SEUS) and the Malawi and Luangwa rift zones of the East African Rift System using the teleseismic *P*-wave amplitude spectra. 14,702 teleseismic *P*-wave amplitude spectra recorded by 477 broadband seismic stations were utilized to map the spatial distribution of Δt^* in the SEUS that provides a better constraint on the crustal and upper mantle *P*-wave attenuation structure than previous larger-scale attenuation studies. The resulting Δt^* measurements reveal an area of relatively high attenuation in the Appalachian Mountains which decreases gradually towards the west as the lithospheric thickness increases. An east-west strip of relatively low attenuation anomalies is observed in the Gulf of Mexico (GoM) Coastal Plain and the southwestern terminus of the Piedmont province. Spatial coherency analysis of the Δt^* observations suggests that the center of the low-attenuation layer is located within the uppermost mantle at about 70 km depth. This low-attenuation anomaly lies along the Suwannee suture zone between Laurentia and Gondwana and approximately coincides with the east-west trending Brunswick magnetic anomaly. The origin of this low-attenuation anomaly can be attributed to low-attenuation bodies in the form of remnant fossil lithospheric. The ratio between the transverse and vertical amplitude of the *P*-wave is calculated to estimate the contribution of scattering to the observed Δt^*. Areas of relatively high transverse/vertical ratios are observed in the Appalachian Plateau and the Floridan

Peninsula, whereas low ratios observed in the GoM Coastal Plain indicate that this area is relatively less capable of producing scattering.

Next, we used *P*-wave amplitude spectra from 203 teleseismic events recorded at 113 SAFARI (Seismic Arrays for African Rift Initiation) and other seismic stations in the vicinity of the Malawi Rift Zone (MRZ) to investigate the mantle dynamics associated with early-stage rifting. The resulting 2,626 Δt^* measurements obtained using the spectral ratio technique reveal high-attenuation anomalies at the northern and southern tips of the MRZ, and an elongated NE-SW strip of low-attenuation anomaly traversing central MRZ. The Δt^* measurements were inverted to image the 3-D attenuation structure down to 400 km depth. The tomographic results reveal a high attenuation zone beneath the RVP in the upper mantle (i.e., down to 300 km depth), which can be associated with the decompression melting. The prominent low-attenuation anomaly traversing the central part of the MRZ suggests the presence of a relatively thick cratonic lithosphere, possibly reflecting the southward subsurface extension of the Bangweulu block.

BIBLIOGRAPHY

Banks, N. L., Bardwell, K. A., & Musiwa, S. (1995). Karoo Rift Basins of the Luangwa Valley, Zambia. *Hydrocarbon Habitat in Rift Basins*, 285–295.

Der, Z. A., & McElfresh, T. W. (1977). The relationship between anelastic attenuation and regional amplitude anomalies of short-period P waves in North America. *Bulletin of the Seismological Society of America*, *67*(5), 1303–1317.

Der, Z. A., McElfresh, T. W., & O'Donnell, A. (1982). An investigation of the regional variations and frequency dependence of anelastic attenuation in the mantle under the United States in the 0.5–4 Hz band. *Geophysical Journal International*, *69*(1), 67–99. https://doi.org/10.1111/j.1365-246X.1982.tb04936.x

Ebinger, C. J., Deino, A. L., Drake, R. E., & Tesha, A. L. (1989). Chronology of volcanism and rift basin propagation: Rungwe volcanic province, East Africa. *Journal of Geophysical Research*, 94 (B11). https://doi.org/10.1029/jb094ib11p15785

Ebinger, C. J., Deino, A. L., Tesha, A. L., Becker, T., & Ring, U. (1993). Tectonic controls on rift basin morphology: evolution of the northern Malawi (Nyasa) Rift. *Journal of Geophysical Research*, 98(B10). https://doi.org/10.1029/93jb01392

Fritz, H., Abdelsalam, M., Ali, K. A., Bingen, B., Collins, A. S., Fowler, A. R., Ghebreab, W., Hauzenberger, C. A., Johnson, P. R., Kusky, T. M., Macey, P., Muhongo, S., Stern, R. J., & Viola, G. (2013). Orogen styles in the East African Orogen: A review of the Neoproterozoic to Cambrian tectonic evolution. Journal of African Earth Sciences, 86, 65–106. https://doi.org/10.1016/j.jafrearsci.2013.06.004

Gao, S. S., & Liu, K. H. (2012). AnisDep: A FORTRAN program for the estimation of the depth of anisotropy using spatial coherency of shear-wave splitting

Golos, E., Fang, H., & van der Hilst, R. D. (2020). Variations in seismic wave speed and Vp/Vs ratio in the North American lithosphere. Journal of Geophysical Research: Solid Earth, 125, e2020JB020574. https://doi.org/ 10.1029/2020JB020574

Hilton, D. R., Halldórsson, S. A., Barry, P. H., Fischer, T. P., de Moor, J. M., Ramirez, C. J., Mangasini, F., & Scarsi, P. (2011). Helium isotopes at Rungwe Volcanic Province, Tanzania, and the origin of East African Plateaux. *Geophysical Research Letters*, 38, L21304. https://doi.org/10.1029/2011GL049589

Hwang, Y. K., Ritsema, J., & Goes, S. (2009). Spatial variations of P wave attenuation in the mantle beneath North America. *Journal of Geophysical Research: Solid Earth*, *114*(B6). https://doi.org/10.1029/2008JB006091

Iverson, W. P., & Smithson, S. B. (1983). Reprocessing and reinterpretation of COCORP southern Appalachian profiles. *Earth and Planetary Science Letters*, *62*(1), 75–90. https://doi.org/10.1016/0012-821X(83)90072-9

Kampunzu, A. B., & Lubala, R. T. (1991). Magmatism in extensional structural settings. *Magmatism in Extensional Structural Settings. Springer Berlin Heidelberg.* https://doi.org/10.1007/978-3-642-73966-8

Lawrence, J. F., Shearer, P. M., & Masters, G. (2006). Mapping attenuation beneath North America using waveform cross-correlation and cluster analysis. *Geophysical Research Letters*, *33*(7), L07315. https://doi.org/10.1029/2006GL025813

Mueller, P. A., Heatherington, A. L., Foster, D. A., Thomas, W. A., & Wooden, J. L. (2014). The Suwannee suture: Significance for Gondwana-Laurentia terrane transfer and formation of Pangaea. Gondwana Research, 26(1), 365–373. https://doi.org/10.1016/j.gr.2013.06.018

O'Donnell, J. P., Selway, K., Nyblade, A. A., Brazier, R. A., Tahir, N. el, & Durrheim, R. J. (2016). Thick lithosphere, deep crustal earthquakes and no melt: a triple challenge to understanding extension in the western branch of the East African Rift. *Geophysical Journal International*, 204 (2), 985–998. https://doi.org/10.1093/GJI

Rankin, D. W., Dillon, W. P., Black, D. F. B., Boyer, S. E., Daniels, D. L., Goldsmith, R., Grow, J. A., Horton, J. W., Hutchinson, D. R., Klitgord, K. D., McDowell, R. C., Milton, D. J., Owens, J. P., Phillips, J. D., Bayer, K. C., Butler, J. R., Elliott, D. W., & Milici, R. C. (1991). *E-4 Central Kentucky to the Carolina Trough.* Geological Society of America. https://doi.org/10.1130/DNAG-COT-E-4

Ritsema, J. (1999). Complex shear wave velocity structure imaged beneath Africa and Iceland. *Science*, 286 (5446), 1925–1928. https://doi.org/10.1126/science.286.5446.1925

Solomon, S. C., & Toksöz, M. N. (1970). Lateral variation of attenuation of P and S waves beneath the United States. *Bulletin of the Seismological Society of America*, *60*(3), 819–838.

Yirgu, G., Ebinger, C. J., & Maguire, P. K. H. (2006). The Afar volcanic province within the East African Rift System: Introduction. *Geological Society Special Publication*, 259, 1–6. https://doi.org/10.1144/GSL.SP.2006.259.01.01

Yu, Y., Gao, S. S., Zhao, D., & Liu, K. H. (2020). Mantle structure and flow beneath an early-stage continental rift: Constraints from P-wave anisotropic tomography. *Tectonics*, 39 (2). https://doi.org/10.1029/2019tc005590

VITA

Ashutosh Shrivastava received his master's degree (Integrated B.Sc. + M.Sc.) in Exploration Geophysics in 2012 from the Indian Institute of Technology Kharagpur, India. He joined Dr. Kelly H. Liu and Dr. Stephen S. Gao's research group in the Geology and Geophysics Ph.D. Program at Missouri University of Science and Technology in August 2016. In July 2021, he received his Ph.D. in Geology and Geophysics from the Missouri University of Science and Technology.